MASARYKOVA UNIVERZITA
PŘÍRODOVĚDECKÁ FAKULTA
ÚSTAV TEORETICKÉ FYZIKY A ASTROFYZIKY

Bakalářská práce

BRNO 2026 JAKUB VYSKOČIL

MASARYKOVA
UNIVERZITA
PŘÍRODOVĚDECKÁ FAKULTA
ÚSTAV TEORETICKÉ FYZIKY A ASTROFYZIKY

Vliv radiální rychlosti na jasnost objektu v úzkopásmovém filtru

Bakalářská práce

Jakub Vyskočil

Vedoucí práce: doc. RNDr. Michal Zajaček, Dr. rer. nat. **Brno 2026**

Bibliografický záznam

Autor:	Jakub Vyskočil Přírodovědecká fakulta, Masarykova univerzita Ústav teoretické fyziky a astrofyziky
Název práce:	Vliv radiální rychlosti na jasnost objektu v úzkopásmovém filtru
Studijní program:	Fyzika
Studijní obor:	Astrofyzika
Vedoucí práce:	doc. RNDr. Michal Zajaček, Dr. rer. nat.
Akademický rok:	2025/2026
Počet stran:	xi + 88
Klíčová slova:	radiální rychlost; Dopplerův jev; úzkopásmová fotometrie; tok záření; dvojhvězdy; kompaktní objekty; černé díry

Bibliographic Entry

Author:	Jakub Vyskočil Faculty of Science, Masaryk University Department of theoretical physics and astrophysics
Title of Thesis:	Effect of radial velocity on object flux density in a narrowband filter
Degree Programme:	Physics
Field of Study:	Astrophysics
Supervisor:	doc. RNDr. Michal Zajaček, Dr. rer. nat.
Academic Year:	2025/2026
Number of Pages:	xi + 88
Keywords:	radial velocity; Doppler effect; narrowband photometry; flux density; binary stars; compact objects; black holes

Abstrakt

V této bakalářské práci studujeme vliv radiální rychlosti objektu na pozorovaný tok záření v úzkopásmovém filtru. Prvně budujeme teoretický základ pro korekci pro radiální rychlosti a následně zobecňujeme tyto korekce i pro další vlivy, jako je třeba gravitační rudý posuv nebo relativistické rychlosti. Následně modelujeme jakou změnu v pozorvané hvězdné velikosti tyto efekty mají na osamocené hvězdy s vysokou radiální rychlostí, dvojhvězdy (ať už klasické nebo kompaktní), objekty obíhající okolo galaktických center nebo na kosmologických škálách. Zároveň se snažíme odpovědět na otázky, zda-li by se daly pomocí periodických fotometrických změn hvězd detekovat neakreující černé díry, a u jakých typů soustav jsou tyhle efekty nezanedbatelné. To celé je prováděno v aproximaci absolutně černých těles, případně jednoduchých modelů akrečních disků.

Abstract

In this thesis, we study the effect of radial velocity on the observed flux density of an object in a narrowband filter. First, we establish theoretical framework for correcting for radial velocity effects, then we extend these corrections to include additional phenomena such as gravitational redshift or relativistic velocities. We then model the resulting changes in observed stellar magnitudes for isolated stars with high radial velocity, binary stars (both classical and those with compact companion), objects in galactic nuclei, and sources on cosmological scales. We also address whether non-accreting black holes can be detected through periodic variations of stars, and identify the types of binary systems in which the these effects cannot be neglected. All calculations are performed under the assumption of blackbody radiation or using simplified models of accretion disks.

MASARYKOVA UNIVERZITA
PŘÍRODOVĚDECKÁ FAKULTA
KOTLÁŘSKÁ 2, 611 37 BRNO
IČ: 00216224
DIČ: CZ00216224

ZADÁNÍ BAKALÁŘSKÉ PRÁCE

Akademický rok: 2025/2026

Ústav:	Ústav teoretické fyziky a astrofyziky
Student:	Jakub Vyskočil
Program:	Fyzika
Specializace:	Astrofyzika

Ředitel *ústavu* PřF MU Vám ve smyslu Studijního a zkušebního řádu MU určuje bakalářskou práci s názvem:

Název práce:	Vliv radiální rychlosti na jasnost objektu v úzkopásmovém filtru
Název práce anglicky:	Effect of radial velocity on object flux density in a narrowband filter
Jazyk práce:	angličtina

Oficiální zadání:

In the Universe, both nearby and more distant, objects are moving with respect to the observer on the Earth with a certain radial velocity. One of the most interesting systems are bound binary systems whose motion is periodic. Due to the periodically changing radial velocity of the emitting objects (stars or compact objects), the flux density is affected by the relativistic Doppler beaming/boosting to a smaller or a larger extent, depending on the ratio of the relative velocity and the speed of light. The student will evaluate these changes in terms of the observed flux density (magnitude) in a narrowband filter. They will focus on known binary stars consisting of stars and compact objects (Cygnus X-1, Scorpius X-1). In addition, they may consider more exotic binary systems, such as S stars orbiting the supermassive black hole in the Galactic center, or binary supermassive black holes in galactic nuclei, where each black hole is surrounded by an accretion disc. The student should discuss applicability of the analyzed periodic flux density changes for discovering new stellar black holes in binary systems using intensive wide-field photometric surveys, such as Vera C. Rubin Legacy Survey of Space and Time and ULTRASAT.

Literatura:

KURMUS, Ali; Michal ZAJAČEK; Gregory KESTIN a Louis DESLAURIERS. Achieving non-orbital particle trapping in binary black holes through dynamic stability. *Classical and Quantum Gravity*. IOP Publishing Ltd, 2025, roč. 42, č. 11, s. 115017-115037. ISSN 0264-9381. Dostupné z: https://doi.org/10.1088/1361-6382/addc2f.

Binary stars as critical tools and tests in contemporary astrophysics : proceedings of the 240th Symposium of the International Astronomical Union, held in Prague, Czech Republic, August 22-25, 2006. Edited by William I. Hartkopf - E. F. Guinan - Petr Harmanec. 1st pub. Cambridge: Cambridge University Press, 2007, xxiii, 479. ISBN 9780521863483.

SHAPIRO, Stuart L. a Saul A. TEUKOLSKY. *Black holes, white dwarfs and neutron stars : the physics of compact objects*. New York: John Wiley & Sons, 1983, 645 s. ISBN 0471873179.

Celestial mechanics and astrodynamics. Edited by Victor G. Szebehely. New York: Academic Press, 1964, xix, 744 p. ISBN 9781600862694.

KARAS, Vladimír; Michal ZAJAČEK; Devaky KUNNERIATH a Michal DOVČIAK. Electromagnetic signatures of strong-field gravity from accreting black-holes. *Advances in Space Research*. Elsevier Ltd, 2022, roč. 69, č. 1, s. 448-466. ISSN 0273-1177. Dostupné z: https://doi.org/10.1016/j.asr.2021.09.012.

DANBY, J. M. Anthony. *Fundamentals of celestial mechanics*. 2nd ed., rev. & enl. Richmond: Willmann-Bell, 1988, xii, 467. ISBN 0943396204.

Methods in astrodynamics and celestial mechanics. Edited by Raynor L. Duncombe - Victor G. Szebehely. New York: Academic Press, 1966, xvi, 436 p. ISBN 9781600862724.

KARAS, Vladimír; Jiří SVOBODA a Michal ZAJAČEK. *Selected Chapters on Active Galactic Nuclei as Relativistic Systems*. Opava: Institute of Physics, Silesian University in Opava, 2021, 154 s. Lecture notes. ISBN 978-80-7510-475-5.

The realm of interacting binary stars. Edited by Jorge Sahade - G. E. McCluskey - Yoji Kondo. Dordrecht: Kluwer Academic Publishers, 1993, 451 s. ISBN 0792316754.

Vedoucí práce:	doc. RNDr. Michal Zajaček, Dr. rer. nat.
Konzultant:	Mgr. Ing. arch. Petr Kurfürst, Ph.D.
Datum zadání práce:	30. 9. 2025
V Brně dne:	12. 12. 2025

Zadání bylo schváleno prostřednictvím IS MU.

Jakub Vyskočil, 2. 10. 2025
doc. RNDr. Michal Zajaček, Dr. rer. nat., 30. 11. 2025
RNDr. Luboš Poláček, 11. 12. 2025

Poděkování

Na tomto místě bych chtěl poděkovat vedoucímu mé bakalářské práce docentu RNDr. Michalu Zajačkovi, Dr. rer. nat. za jeho cenné rady, čas, ochotu i zkušenosti, které mi předal. Za totéž jsem vděčný i konzultantovi Mgr. Ing. arch. Petru Kurfürstovi, PhD. Dále bych vyjádřil své velké dík své rodině, blízkým přátelům i lidem, kteří se mnou na této cestě, ať už celé či jen její části, účinkovali. A na samotný závěr, děkuji i těm, kteří stáli proti mně, neboť díky ním jsem získal motivaci uvést je v omyl.

Prohlášení

Prohlašuji, že jsem svoji bakalářskou práci vypracoval samostatně pod vedením vedoucího práce s využitím informačních zdrojů, které jsou v práci citovány.

Brno 10. května 2026 .....

Jakub Vyskočil

Contents

Introduction

Imagine looking at the stars and trying to shoot one of these beautiful nebulae. To avoid light pollution from surrounding light sources, use a special photometric filter for emission lines, such as Hα. Now, seeing your nebula glowing in the images, you ask a question. What if the nebula wanted to hide. It cannot escape because it is really large. However, if the nebula uses the knowledge of the Doppler effect and starts escaping in the radial direction from use, the emission line could in extreme cases shift from the photometric filter, which would make the nebula disappear.

This story does not have to affect only nebulae, but it can touch anything that shines with a spectral distribution. Our aim is to focus mainly on systems with periodic radial velocity variations, such as binary stars or objects orbiting the Galactic centre. Moreover, we would like to determine the conditions for a binary system with an invisible black hole to be recognized as a candidate for future spectroscopic observations. Lastly, we will study the effect in cosmology and discuss its the relevance in modern astronomy.

Chapter 1

Why do we use photometric filters

All of us have heard of photometric filters and photometric systems (Johnson–Morgan, Strömgren, etc.), which are used for studying segments of source of lights. But why do we not observe the whole light and take only part of the spectra? There are several complications that we have to face and take into account. However, there are good reasons for studying the universe in photometric filters.

1.1 Obstacles

Observations are connected with getting information about the object. Information is essential to understand the physical phenomena about the source, its surroundings, or physics itself. First, let us look at the obstacles connected with not receiving all the light from the sources.

1.1.1 Atmosphere and interstellar dust

The atmosphere is a layer of gas that surrounds the Earth. It provides us with air to breathe, protects us from high energy radiation such as UV, X-ray, and gamma, and thanks to greenhouse gases, the temperature is habitable.

One of the problems with atmosphere has already been mentioned. Fortunately, it protects us from high-energy radiation, but from the surface we can hardly detect any photons from this part of the electromagnetic (EM) spectrum, and we have to send the satellites to space. This not only concerns the high-energy radiation, but also partially infrared (IR) and microwave radiation at specific wavelength bands; see Fig. 1.1.

Hand in hand with absorption, there is scattering, and together they both contribute to extinction. Extinction is called when the intensity of light is somehow reduced. In our atmosphere, it is mostly caused by scattering but at specific wavelengths, there is also absorption by gases in the atmosphere. The rate of change in intensity I with respect to length l is the following:

$$\frac{\mathrm{d}I}{\mathrm{d}l} = -I_0 k_\lambda \,, \tag{1.1}$$

where I_0 is the intensity of the incoming light, k_λ is an extinction coefficient depending on the wavelength λ. Scattering is simply a physical process in which light or particles deviate

from a straight trajectory. We can name Rayleigh scattering on molecules, Mie scattering on aerosol, or Thomson scattering on electrons. For example, Rayleigh scattering causes the blue color of the sky during the day and red in the evening. Furthermore, we need to take into account how much air is above us. The more air, the more scattering effect, which

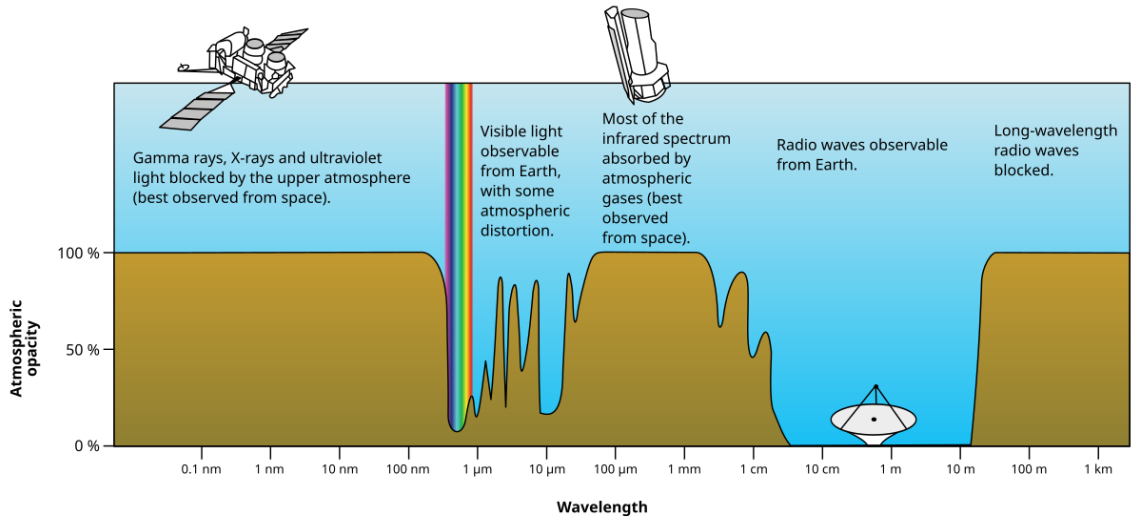

Figure 1.1: This plot shows the dependence of the atmospheric opacity on the wavelength (100% represents the complete opacity, optical depth of 1). Credit: NASA; (Wikimedia Commons).

is actually the reason why the sky appears red in the evening. The amount of air above us is described by the air mass X. In the simplest case, we can describe it as follows:

$$X = \frac{1}{\cos z} = \sec z, \tag{1.2}$$

where z is the zenith angle. Note that there are better approximations, but that is beyond the scope of this work.

All of the problems above can be applied to the interstellar environment, including interstellar dust and molecules, which are the sources of extinction. This makes stars appear more red and dimmer.[1]

Therefore, we need good calibrating stars to resolve how the atmosphere behaves and how big the extinction is. In addition, we need meteorological stations to know atmospheric pressure, temperature, and humidity. These parameters are essential to establish the correct air mass and atmospherical condition for the observations. Moreover, the behavior of the atmosphere and the amount of interstellar extinction affect each wavelength differently. So, we have to measure the calibration stars in various photometric filters for correct measurements.

[1] The discoverer of scattering by interstellar dust was Robert Trumpler, while measuring the brightness of distant open clusters.

1.1.2 Observational instruments

In astronomy, photomultipliers, Charge-Couple Devices (CCDs) or Complementary Metal-Oxide-Semiconductors (CMOS) are commonly used. But why do we use them? Well, observation through our eyes is very subjective and nowadays not accurate. All instruments react in some way to light and, of course, differently. These instruments have some efficiency for each waveband, which leads to the inability to receive all the light going on the sensor. We had to decide how bright the stars appear in the specific waveband. It would be nice to separate the specific light for the best correction. This makes us to invent photometric systems with photometric filters. There are many measurements of various stars that are used for calibration.

1.2 Benefits of photometric filters

Are there any benefits of observing through photometric filters? We must observe many stars through a few filters, not just make one quick observation and even not get all light from it. However, is it always the best option to get all the information in one big step? Probably not because sometimes we just want to focus on some specific event that is visible only in a certain band. Using photometric filters could tell us more than we imagine. Let us make it clear using following example:

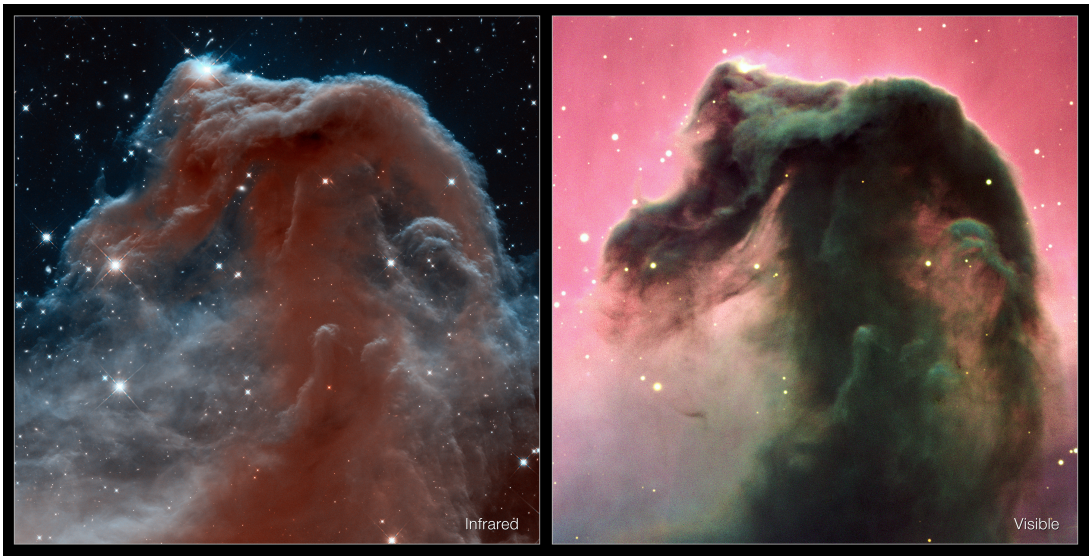

Figure 1.2: Horsehead Nebula captured in IR in the left panel by Hubble's high-resolution Wide Field Camera 3 and in visible band in the right panel taken by Very Large Telescope in Chile - Credit: NASA, ESA and Hubble.

In the picture on the left side, we can see the Horsehead nebula taken in IR, and on the right site there is the same object in visible light. The object shines mostly in the visible spectrum. So, if we observed it in the whole spectrum, we would not see the stars hidden in dark nebulae, which are noticeable in IR. Moreover, in the IR part of the spectra, we can study the birth of new stars, that is, in fact, what we see in the picture on the left.

Using a color-magnitude diagram, we can study the age of star clusters or stellar associations. This helps us to prove theories of stellar evolution and thus gives us a deeper understanding. In addition, it can reveal how star clusters are formed.

Sometimes it is more practical to use a narrow photometric filter instead of a wide-field. Although getting fewer data might sound like nonsense, it can help us to focus on details. Imagine that we observe supernovae remanent and we would like to study its structure. Most supernova remnants are made of ionized gases such as hydrogen, helium, oxygen, etc. Instead of earning amounts of data which are not necessary, it is better to focus on the emission lines produced by remanent. An example can be shown the Veil Nebula, a supernova remanent in Cygnus located near Aljanah (ε Cyg), Fig. 1.3.

Last but not least, the sky is glowing. Now we do not speak about the natural glow of the sky, but about the light pollution. Light pollution is a big problem in many places. This problem is well known, and we are trying to solve it. However, there are still many

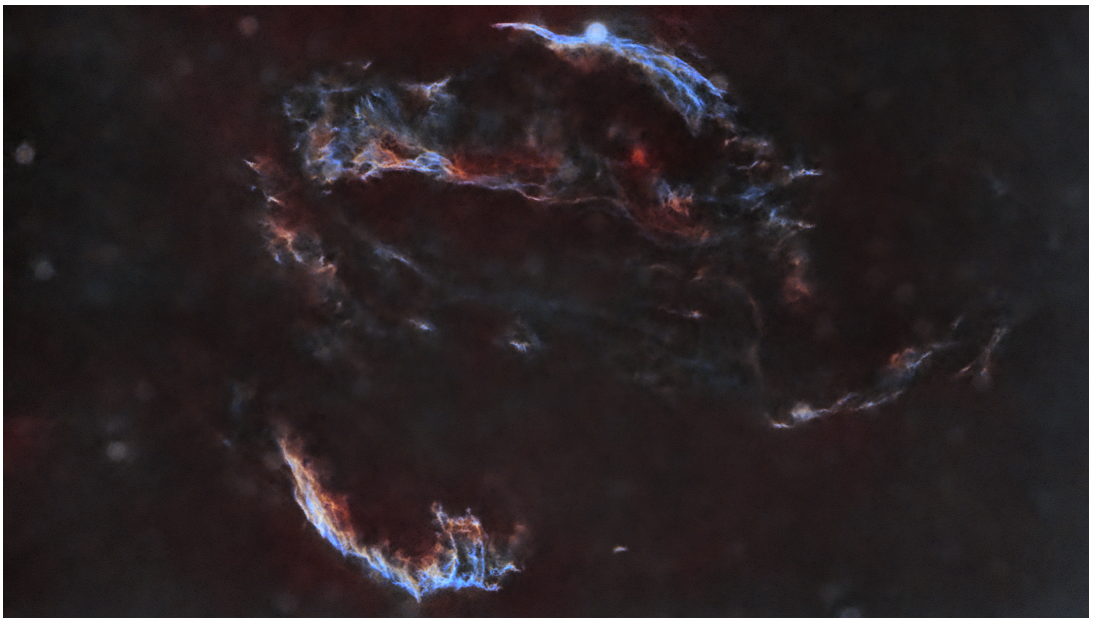

Figure 1.3: The Veil Nebula located in Cygnus captured through the narrowband filter (Optolong L-enhance: Hα (656 nm) and $H\beta$ (486 nm) emission lines and double ionized oxygen [OIII] (501 nm)]) - Credit Jakub Vyskočil.

places like factories, buildings, etc., that make our sky shine, which adds noise to our observations, and then more observational time is needed. Fortunately, we have filters that can avoid sodium discharge tubes or study the structure thanks to emission lines. Of course, there is the possibility to combine the data through broadband filters with data from narrowband filters. Not only does it reveal the structure, but it can also display the locations of various components. In Fig. 1.3, blue structures are made of double ionized oxygen [OIII], and red structures consist of ionized hydrogen HII, which shines mostly at Hα. Astrophotographers and Hubble use another emission line from ionized sulfur [SII], which also shines a lot and reveals essential detail, which can be beautifully highlighted using the SHO Hubble pallet. The great target for SHO astrophotography can be the Eagle Nebula located in Serpens 1.4, as it shines brightly in Hα, [OIII] and [SII] as well. Using sulfur

as red, hydrogen as green, and oxygen as blue makes a spectacular color variation image, which is not what we would see. However, it tells us something about the structure of nebulae.

Figure 1.4: The Eagle Nebula located in Serpens captured through narrowband filter (Optolong L-enhance: Hα (656 nm) and $H\beta$ (486 nm) emission lines and double ionized oxygen [OIII] (501 nm) + Optolong [SII] - central wavelength 672 nm and half value width 6.5 nm) - Credit Jakub Vyskočil.

Chapter 2

Physical background

In this chapter, we will focus on the physical background, which is necessary to understand observed processes. In our thought experiment, one arrives at a solution that as a result of radial velocity the wavelengths get shifted. However, we can interpret the problem that the central wavelength and the band of the filer in the observer's frame of reference do not change but the wavelength (energy) of incoming photons from the source are affected by its motion with respect to the observer. Therefore, before we start, we will begin with the review of physics connected to our problem such as black-body radiation, Doppler effect, Keplerian motion, and a little bit of Cosmology.[1]

2.1 Black-body radiation

The concept of a black body is a very simple model of a heated body, which emits as much as it absorbs. One would say that the properties of the radiation would depend on the type of material. Surprisingly, it depends only on the temperature, as we will show. But what is black body radiation and how can we imagine it? Let us do a simple thought experiment. Imagine that we have a box with black walls inside and there is a photon gas in it. The walls of the box would be heated to a constant temperature T. To observe the radiation, it would be necessary to make a small hole to see the photon gas. The radiation would have basic properties such that the intensity of the radiation only depends on temperature and, moreover, the black body radiation is isotropic, it does not depend on direction from which we observe the radiation.

2.1.1 Planck's distribution law

For many years, scientists struggled with theoretical model for the black body radiation, since description led to the so called ultraviolet catastrophe: the intensity for short wavelength went to infinity. Then Max Planck came with, firstly, a mathematical solution: quantization of energy

$$E = hf, \tag{2.1}$$

[1] This chapter really contains very simple physical problems, so feel free to skip to Chapter 3.

where E is the energy, f is the frequency, and $h = 6.626 \times 10^{-34}$ J·s is the so-called Planck constant. In nutshell, the concept says that energy is exchanged by a small amount called photons. The quantization of energy was then proved by the photoelectric effect, for whose description Albert Einstein got his Nobel prize in 1921. This will help us in thermodynamics and statistical physics.

Thermodynamics stands on three axioms and a few relations which can be measured or obtained from axioms. Of course, we can add properties of materials such as heat capacity, magnetic susceptibility, etc. However, statistical description begins with the energy and number of particles in the system. Of course, there are limitations for systems and using this we can divide them into three categories:

- Microcanonical ensemble: the system cannot exchange energy and particles (isolated system)
- Canonical ensemble: the system cannot exchange particles but can exchange energy (closed system)
- Grand-canonical ensemble: the system can exchange energy and particles (open system)

We will be using the most general one, the Grand-canonical ensemble. One of the standard definitions of entropy uses the Boltzmann constant

$$S = k_{\mathrm{B}} \ln \Gamma, \tag{2.2}$$

where Γ is the number of possible states and $k_{\mathrm{B}} = 1.381 \times 10^{-23}$ J·K^{-1} is the Boltzmann constant. From this we can arrive at the probability of finding the system in the n-th quantum state with N particles as

$$w_{nN} = \frac{1}{\Xi} \mathrm{e}^{-\beta(\varepsilon_{nN} - \mu N)}, \tag{2.3}$$

where $\beta = \frac{1}{k_{\mathrm{B}} T}$ and we introduce the grand-canonical partition sum in the following form

$$\Xi = \sum_n \sum_N \mathrm{e}^{-\beta(\varepsilon_{nN} - \mu N)}, \tag{2.4}$$

which will be used to derive the Planck's distribution law. The grand-canonical partition sum is connected to the Grand-canonical (Landau's) potential Ω, which can be obtained from free energy F

$$\Omega = F - \mu N, \tag{2.5}$$

where μ is a chemical potential, which basically says how much energy the system gains by adding a particle and N is the number of particles. Free energy can be obtained from

$$F = E - TS, \tag{2.6}$$

where T is a temperature and S is an entropy. Since $\mathrm{d}\Omega$

$$\mathrm{d}\Omega = -p \, \mathrm{d}V - S \, \mathrm{d}T - N \, \mathrm{d}\mu \tag{2.7}$$

represents an exact form, one can arrive at the following relations:

$$p = -\left(\frac{\partial \Omega}{\partial V}\right)_{\mu,T}, \tag{2.8}$$

$$S = -\left(\frac{\partial \Omega}{\partial T}\right)_{\mu,V}, \tag{2.9}$$

$$N = -\left(\frac{\partial \Omega}{\partial \mu}\right)_{V,T}. \tag{2.10}$$

Moreover, it can be easily shown that

$$\Omega_i = -k_{\mathrm{B}} T \ln \Xi_i. \tag{2.11}$$

We can conclude that if we know the Grand-canonical potential, we have all the thermodynamic information about the system, such as equation of state, entropy, number of particles, or using various relations, heat capacities etc.
Now we move on to the derivation. Recalling the Grand-canonical potential as

$$\Omega = \int_0^\infty \Omega_\varepsilon \, \mathrm{d}\Gamma_\varepsilon, \tag{2.12}$$

where Ω_ε is given by the identity (2.11) and $\mathrm{d}\Gamma_\varepsilon$ is a weight factor which can be determined in an element of phase-space $\mathrm{d}\phi$ with the degeneracy factor g,

$$\mathrm{d}\Gamma_i = g\frac{\mathrm{d}\phi}{h^3} = g\frac{\mathrm{d}x\,\mathrm{d}y\,\mathrm{d}z\,\mathrm{d}p_x\,\mathrm{d}p_y\,\mathrm{d}p_z}{h^3}. \tag{2.13}$$

For photons, the degeneracy factor depends on the polarization, since there are two possible polarizations, we can set $g = 2$. Integrating over volume and transforming from momenta to energy gives us a formula

$$\mathrm{d}\Gamma_\varepsilon = \frac{8\pi V \varepsilon^2}{h^3 c^3}\,\mathrm{d}\varepsilon. \tag{2.14}$$

We obtained the density of energetic states $\gamma(\varepsilon)$

$$\mathrm{d}\Gamma_\varepsilon = \gamma(\varepsilon)\,\mathrm{d}\varepsilon, \quad \gamma(\varepsilon) = \frac{8\pi V \varepsilon^2}{h^3 c^3}. \tag{2.15}$$

The total energy of photons with energy ε is given by

$$U_\varepsilon = \varepsilon N_\varepsilon. \tag{2.16}$$

The chemical potential of photons is $\mu = 0$. The number of photons with energy ε is given by

$$N_\varepsilon = -\lim_{\mu \to 0} \frac{\partial \Omega_\varepsilon}{\partial \mu}. \tag{2.17}$$

For intensity, we can use the formula

$$I(T) = \frac{uc}{4}. \tag{2.18}$$

For

$$u = \frac{U}{V} = \frac{8\pi}{h^3 c^3} \int_0^\infty \frac{\varepsilon^3}{\exp\left(\frac{\varepsilon}{k_B T}\right) - 1} \, \mathrm{d}\varepsilon. \tag{2.19}$$

Using $\varepsilon = hf$, we finally obtain the relation between radiation intensity, frequency, and temperature

$$\frac{\mathrm{d}I(f,T)}{\mathrm{d}f} = \frac{2\pi h f^3}{c^2} \frac{1}{\exp\left(\frac{hf}{k_B T}\right) - 1}, \tag{2.20}$$

where $c = 2.998 \times 10^8 \ \mathrm{m \cdot s^{-1}}$ is the speed of light in vacuum. We can see that the relation depends only on the frequency and thermodynamic temperature. Finally, we can write the relation with wavelengths λ

$$\frac{\mathrm{d}I(\lambda,T)}{\mathrm{d}\lambda} = \frac{2\pi h c^2}{\lambda^5} \frac{1}{\exp\left(\frac{hc}{\lambda k_B T}\right) - 1}. \tag{2.21}$$

Let us plot the relation for the wavelengths, see Fig. 2.1. From the graph, it can be said that

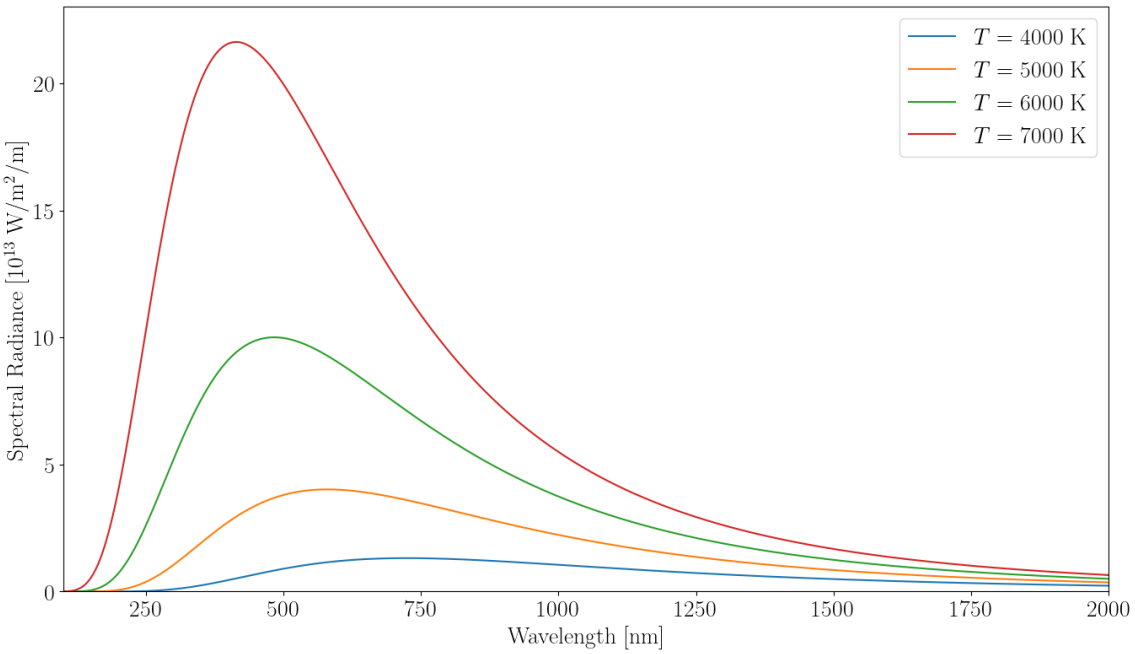

Figure 2.1: Planck's distribution law for different temperatures in legend.

for higher temperatures, the intensity increases for all wavelengths. Moreover, for higher temperatures the maximum intensity shifts to shorter wavelengths. We will discuss this shifting of the maxima in the Section about Wien's displacement law.

2.1.2 Wien's displacement law

Wien's displacement law describes the relation between the wavelength at which the maximum intensity occurs λ_{max} and the temperature. Finding the maximum of the relation

(2.21), mathematically speaking, we are searching for the point at which the first derivative with respect to the wavelength is equal to zero.

$$\frac{\mathrm{d}}{\mathrm{d}\lambda}\left[\frac{2\pi hc^2}{\lambda^5}\frac{1}{\exp\left(\frac{hc}{\lambda k_\mathrm{B}T}\right)-1}\right]=0, \tag{2.22}$$

$$\frac{-5\lambda^{-6}\left[\exp\left(\frac{hc}{\lambda k_\mathrm{B}T}\right)-1\right]+\lambda^{-7}\exp\left(\frac{hc}{\lambda k_\mathrm{B}T}\right)\frac{hc}{k_\mathrm{B}T}}{\left[\exp\left(\frac{hc}{\lambda k_\mathrm{B}T}\right)-1\right]^2}=0, \tag{2.23}$$

$$\Rightarrow 5\left[\exp\left(\frac{hc}{\lambda k_\mathrm{B}T}\right)-1\right]=\exp\left(\frac{hc}{\lambda k_\mathrm{B}T}\right)\frac{hc}{\lambda k_\mathrm{B}T}. \tag{2.24}$$

This is a transcendental equation; in other words, it cannot be solved analytically. Therefore, we need to solve it numerically. One obtains the final form of Wien's displacement law

$$\lambda_\mathrm{max}=\frac{b}{T}, \tag{2.25}$$

where $b=2.898\times10^{-3}\ \mathrm{m}\cdot\mathrm{K}$ is Wien's constant. We can infer from this relation and from the Planck's distribution that for higher temperatures the peaks can be found at shorter wavelengths. This is a very important physical law that will help us in describing different phenomena.

2.1.3 Stefan–Boltzmann law

Looking at the graph 2.1, it would surely be clever to ask how much intensity the black body emits. We will now use the relation (2.20) which is simpler to integrate. We need to integrate over all frequencies f

$$I=\frac{2\pi h}{c^2}\int_0^\infty\frac{f^3}{\exp\left(\frac{hf}{k_\mathrm{B}T}\right)-1}\,\mathrm{d}f=\frac{2\pi k_\mathrm{B}^4}{c^2h^3}T^4\int_0^\infty\frac{x^3}{\mathrm{e}^x-1}\,\mathrm{d}x. \tag{2.26}$$

Simple substitution shows us that the intensity depends on the temperature of the black body, specifically $I\sim T^4$. However, the integral $\mathscr{I}=\int_0^\infty\frac{x^3}{\mathrm{e}^x-1}\,\mathrm{d}x$ is not that easy to solve[2] and leads to

$$\int_0^\infty\frac{x^3}{\mathrm{e}^x-1}\,\mathrm{d}x=\frac{\pi^4}{15}. \tag{2.27}$$

Finally, we are able to give an exact solution for the intensity of radiation of the black body, which is described by the Stefan–Boltzmann law

$$I=\sigma T^4,\qquad\sigma=\frac{2\pi^5k_\mathrm{B}^4}{15h^3c^2}=5.670\times10^{-8}\ \mathrm{W}\cdot\mathrm{m}^{-2}\cdot\mathrm{K}^{-4}, \tag{2.28}$$

where σ is the Stefan–Boltzmann constant. As we mentioned earlier, we do not access to the whole intensity, and generally, we would like to know how much intensity we

[2]The whole solution can be found in the appendix (C) of this work.

will observe in a specific photometric filter. This filter can be described with a range of wavelengths $[\lambda_0, \lambda_0 + \Delta\lambda]$.[3] Now the intensity in the photometric filter is given by the following integral

$$I(\lambda, \Delta\lambda, T) = 2\pi hc^2 \int_{\lambda_0}^{\lambda_0+\Delta\lambda} \frac{\lambda^{-5}}{\exp\left(\frac{hc}{\lambda k_B T}\right) - 1} \, \mathrm{d}\lambda, \tag{2.29}$$

which, once again, cannot be solved analytically. Therefore, we will be using numerical methods to obtain the intensities. All in all, it is not really necessary to get a general solution; however, it would help us with the job, but it is mostly the pre-work to which we will refer.

2.2 Doppler Effect

We have all experienced different sounds from the ambulance that was driving along us. The sound might appear higher when the ambulance is coming towards us than away from us. That is what is called the Doppler effect, which describes how the observed frequency changes in relation to the radial velocity of the source. However, the Doppler effect also applies to light; a nice illustration can be seen in Fig. 2.2. It would be natural to start with derivation of the classic Doppler effect and then derive the relativistic Doppler effect. However, I find it more natural to derive the relativistic Doppler effect and then use the classical limit to show the result for non-relativistic velocities.

2.2.1 Relativistic Doppler effect

Consider two inertial frames S and S'. Let the S frame be at rest and let S' be moving along the common x-axis $x = x'$. Imagine that there is a source of radiation with frequency ω_0 in S' frame. Observing from the S frame, we would like to know the observed frequency ω. Using the four-vector $\left(\frac{\omega_0}{c}, -\mathbf{k}\right)$, where $\mathbf{k}$ is the wave-vector. In S' we have

$$\begin{pmatrix} \frac{\omega_0}{c} \\ -k_x \\ -k_y \\ -k_z \end{pmatrix} = \begin{pmatrix} \frac{\omega_0}{c} \\ -k\cos\alpha \\ -k\sin\alpha \\ 0 \end{pmatrix} = \begin{pmatrix} \frac{\omega_0}{c} \\ -\frac{\omega_0}{c}\cos\alpha \\ -\frac{\omega_0}{c}\sin\alpha \\ 0 \end{pmatrix}. \tag{2.30}$$

Using the Lorentz transformation

$$\Lambda = \begin{pmatrix} \gamma & -\gamma\beta & 0 & 0 \\ -\gamma\beta & \gamma & 0 & 0 \\ 0 & 0 & 1 & 0 \\ 0 & 0 & 0 & 1 \end{pmatrix}, \tag{2.31}$$

where $\gamma = \frac{1}{\sqrt{1-\beta^2}}$ and $\beta = \frac{v}{c}$. Taking only the first term, we obtain

$$\omega = \gamma\left(1 + \frac{v}{c}\cos\alpha\right)\omega_0. \tag{2.32}$$

[3] Of course, we can describe the range by frequencies and use the relation with the same variable, but it is more natural to use wavelengths.

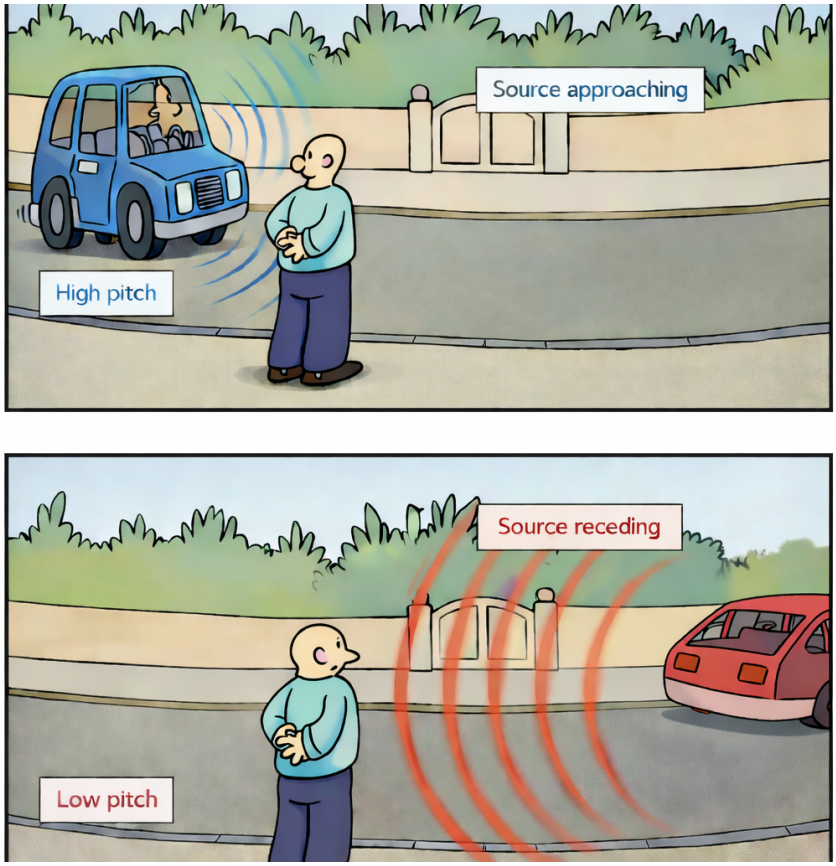

Figure 2.2: Illustration of the Doppler effect - original Fig. from reddit upgraded resolution using ChatGPT5.

Since we focus on radial velocities, let us set the $\alpha = 180°$. For the radial velocity from us, we will use plus, and for motion toward us we will use the negative sign. Using this convention, our relation will be in the form

$$\omega = \sqrt{\frac{1 - v_r/c}{1 + v_r/c}}\omega_0. \tag{2.33}$$

For wavelengths, we can recalculate the relation

$$\omega = 2\pi f = 2\pi\frac{c}{\lambda}. \tag{2.34}$$

Plugging in (2.33) and rearranging terms, we will obtain

$$\frac{\lambda_o}{\lambda_e} = \sqrt{\frac{1 + v_r/c}{1 - v_r/c}}. \tag{2.35}$$

2.2.2 Classical limit

Now, for the classical limit, we will use $v_r \ll c \Rightarrow v_r/c \ll 1$. Therefore, we can use Taylor expansion $(1 \pm x)^n \approx 1 \pm nx$, we obtain

$$\frac{\lambda_o}{\lambda_e} \approx \left(1 + \frac{v_r}{2c}\right)^2 \approx 1 + \frac{v_r}{c}. \tag{2.36}$$

Rearranging the terms, we get the well-known relation

$$\frac{\Delta\lambda}{\lambda_e} = \frac{\lambda_o - \lambda_e}{\lambda_e} = \frac{v_r}{c} \tag{2.37}$$

for the classical Doppler shift. It is obvious that using our convention, we really observe longer wavelengths for positive velocities and shorter wavelengths for negative radial velocities.

2.3 Parameters of the trajectory

Now, since we know that the radial velocity can affect the observed wavelength, it is a good time to start describing the orbital trajectories. Why orbital trajectories? Orbiting is in most cases connected to periodic motion, and for us it is useful to study periodic changes.

2.3.1 Gravitational One-Body Problem

Firstly, we would like to describe the motion of our planet around the Sun before we examine a more complex motion. As the mass of the Earth ($M_{Earth} = 5.972 \times 10^{24}$ kg) is much smaller than the mass of Sun ($M_\odot = 1.989 \times 10^{30}$ kg), we can assume that the Earth orbits the Sun. Kepler taught us that all planets orbit the Sun on elliptical trajectories, with the Sun located at one of the foci of these ellipses. Describing an ellipse is a fundamental mathematical concept, and the derivation of the equation of ellipse is relatively simple, however, it is beyond the scope of this work. We can write the general equation of the ellipse as

$$\frac{x^2}{a^2} + \frac{y^2}{b^2} = 1, \tag{2.38}$$

where a is the length of the semi-major axis and b is the length of the semi-minor axis. From the geometry of the ellipse we can derive an equation for the length of the semi-minor axis using the numerical eccentricity e and the length of the semi-major axis. Firstly, let us define eccentricity as the distance between the centre of the ellipse and the focus of the ellipse ε. The relation between the numerical eccentricity is given by

$$e = \frac{\varepsilon}{a}. \tag{2.39}$$

Using the Pythagorean theorem, we can derive the following formula from the right-angle triangle

$$b = a\sqrt{1 - e^2}. \tag{2.40}$$

The Cartesian coordinate system is not the best option we could use. Using polar coordinates is a more natural idea. However, we should not set the origin to the centre of the ellipse but rather set the origin to the focus. This step will help us determine the distance of the Earth from the Sun as a function of the true anomaly $r = r(\phi)$, which is an angle with the origin in the focus and is measured from the closest point of the ellipse to the focus. The closest point of the ellipse to the focus is usually called periapsis. Using a basic geometry, we write the relations between the polar and the Cartesian coordinates as follows

$$x = ae + r\cos\phi, \tag{2.41}$$

$$y = r\sin\phi. \tag{2.42}$$

Connecting Eqs. (2.38), (2.41) and (2.41) and substituting for b from Eq. (2.40), we can write

$$\frac{a^2e^2 + 2aer\cos\phi + r^2\cos^2\phi}{a^2} + \frac{r^2\sin^2\phi}{a^2(1-e^2)} = 1. \tag{2.43}$$

By solving this quadratic formula we obtain, taking into account that r is always positive, the final formula

$$r(\phi) = \frac{a\left(1-e^2\right)}{1+e\cos\phi}. \tag{2.44}$$

Now, we would like to derive the first Keplerian law from the equations of motion. We will consider spherical coordinates, and for these, we have the following expression for acceleration

$$\begin{aligned}\mathbf{a} = &\left[\frac{\mathrm{d}^2r}{\mathrm{d}t^2} - r\left(\frac{\mathrm{d}\theta}{\mathrm{d}t}\right)^2 - r\sin^2\theta\left(\frac{\mathrm{d}\phi}{\mathrm{d}t}\right)^2\right]\hat{\mathbf{r}} \\ &+ \left[r\frac{\mathrm{d}^2\theta}{\mathrm{d}t^2} + 2\frac{\mathrm{d}r}{\mathrm{d}t}\frac{\mathrm{d}\theta}{\mathrm{d}t} - r\sin\theta\cos\theta\left(\frac{\mathrm{d}\phi}{\mathrm{d}t}\right)^2\right]\hat{\theta} \\ &+ \left[r\sin\theta\frac{\mathrm{d}^2\phi}{\mathrm{d}t^2} + 2\sin\theta\frac{\mathrm{d}r}{\mathrm{d}t}\frac{\mathrm{d}\phi}{\mathrm{d}t} + 2r\cos\theta\frac{\mathrm{d}\theta}{\mathrm{d}t}\frac{\mathrm{d}\phi}{\mathrm{d}t}\right]\hat{\phi},\end{aligned} \tag{2.45}$$

where $\hat{\mathbf{r}}, \hat{\theta}$ and $\hat{\phi}$ are the basis vectors.[4] Using Newton's second law, we can write $\mathbf{a} = \frac{\mathbf{F}}{m}$, and therefore

$$\frac{\mathrm{d}^2r}{\mathrm{d}t^2} - r\left(\frac{\mathrm{d}\theta}{\mathrm{d}t}\right) - r\sin^2\theta\left(\frac{\mathrm{d}\phi}{\mathrm{d}t}\right)^2 = -\frac{GM}{r^2} \tag{2.46}$$

$$r\frac{\mathrm{d}^2\theta}{\mathrm{d}t^2} + 2\frac{\mathrm{d}r}{\mathrm{d}t}\frac{\mathrm{d}\theta}{\mathrm{d}t} - r\sin\theta\cos\theta\left(\frac{\mathrm{d}\phi}{\mathrm{d}t}\right)^2 = 0 \tag{2.47}$$

$$r\sin\theta\frac{\mathrm{d}^2\phi}{\mathrm{d}t^2} + 2\sin\theta\frac{\mathrm{d}r}{\mathrm{d}t}\frac{\mathrm{d}\phi}{\mathrm{d}t} + 2r\cos\theta\frac{\mathrm{d}\theta}{\mathrm{d}t}\frac{\mathrm{d}\phi}{\mathrm{d}t}^2 = 0 \tag{2.48}$$

We can solve Eq. (2.47) by setting $\theta = \frac{\pi}{2}$ radians, so that the motion is confined to the equatorial plane. This allows us to simplify Eq. (2.48) to

$$\frac{1}{r}\frac{\mathrm{d}}{\mathrm{d}t}\left(r^2\frac{\mathrm{d}\phi}{\mathrm{d}t}\right) = 0. \tag{2.49}$$

[4] Derivation of the acceleration in the spherical coordinates can be found in Abstract D.

The formula inside the derivation is the specific angular momentum

$$\ell = |\ell| = |\mathbf{r} \times \mathbf{v}| = r^2 \frac{\mathrm{d}\phi}{\mathrm{d}t}. \tag{2.50}$$

From Eq. (2.49) we may say that the angular momentum is conserved. Finally, we can solve for the radial motion, as Eq. (2.46) becomes

$$\frac{\mathrm{d}^2 r}{\mathrm{d}t^2} - \frac{\ell^2}{r^3} = -\frac{GM}{r^2}. \tag{2.51}$$

It would be better to know the radial distance as a function of an angle ϕ. Let us make a substitution for $r = \frac{1}{u}$ and find the derivative with respect to ϕ. This leads to

$$\frac{\mathrm{d}r}{\mathrm{d}t} = \frac{\mathrm{d}(1/u)}{\mathrm{d}\phi}\frac{\mathrm{d}\phi}{\mathrm{d}t} = -\ell\frac{\mathrm{d}u}{\mathrm{d}\phi} \tag{2.52}$$

and similarly

$$\frac{\mathrm{d}^2 r}{\mathrm{d}t^2} = \frac{\mathrm{d}}{\mathrm{d}\phi}\left(-\ell\frac{\mathrm{d}u}{\mathrm{d}\phi}\right)\ell u^2 = -\ell^2 u^2 \frac{\mathrm{d}^2 u}{\mathrm{d}\phi^2}. \tag{2.53}$$

Now we can rewrite Eq. (2.51) as following

$$\frac{\mathrm{d}^2 u}{\mathrm{d}\phi^2} + u = \frac{GM}{\ell^2} \tag{2.54}$$

and find the solution

$$\frac{1}{r(\phi)} = u(\phi) = B\cos\phi + \frac{GM}{\ell^2} = \left|B = \frac{GMe}{\ell^2}\right| = \frac{GM}{\ell^2}\left(1 + e\cos\phi\right). \tag{2.55}$$

This curve describes an ellipse with the eccentricity e.

To examine Kepler's second law, we will consider the area $\mathrm{d}A$ swept by the motion of the planet in some small time interval $\mathrm{d}t$. It can be shown from geometry that the relation for this area is

$$\mathrm{d}A = \frac{1}{2}|\mathbf{r} \times \mathbf{v}\mathrm{d}t| = \frac{1}{2}|\ell|\,\mathrm{d}t \tag{2.56}$$

and we can see, thanks to the conservation of the norm of vector $|\ell|$, the rate of change of area with respect to time is constant. This is an important result because it tells us that if a planet is closer to the star, it has to move faster than it is further from the star.

Moving on to the third Kepler's law, we would like to use the area of the ellipse. There are two ways to compute the area of the ellipse. The first option is to derive using the geometry and the integral, when we would obtain the formula

$$A = \pi ab = \pi a^2\sqrt{1 - e^2} \tag{2.57}$$

The second option is to use the relation for the second Kepler's law

$$\frac{\mathrm{d}A}{\mathrm{d}t} = \frac{\ell}{2} \tag{2.58}$$

Now we introduce the orbital period of the planet P. We know that the planet in one orbital period has to orbit the whole ellipse and the area is A, therefore we get

$$A = \frac{\mathrm{d}A}{\mathrm{d}t} \cdot P = \frac{\ell P}{2} \tag{2.59}$$

It would be helpful to know the exact formula for the specific angular momentum ℓ. Fortunately, by comparing equations (2.44) and (2.55), we get the relation for ℓ

$$\ell = \sqrt{GMa\,(1-e^2)} \tag{2.60}$$

By combining Eq. (2.57) and (2.59), and substituing ℓ, we obtain

$$\frac{a^3}{P^2} = \frac{GM}{4\pi^2} \tag{2.61}$$

which is our final formula.

2.3.2 Gravitational Two-Body Problem

In this paragraph, we will attempt to describe the parameters of the trajectories in a two-body system. Consider the gravitational interaction between mass m_1 at position $\mathbf{r}_1$ and mass m_2 at position $\mathbf{r}_2$. Define the separation vector,

$$\mathbf{r} = \mathbf{r}_2 - \mathbf{r}_1 \tag{2.62}$$

and the position of the center of mass,

$$\mathbf{R} = \frac{m_1\mathbf{r}_1 + m_2\mathbf{r}_2}{m_1 + m_2} \tag{2.63}$$

Also, define the reduced mass,

$$\mu_\mathrm{m} = \frac{m_1 m_2}{m_1 + m_2} \tag{2.64}$$

and the total mass,

$$M = m_1 + m_2 \tag{2.65}$$

Using Newton's second and third law, we can derive that the acceleration of the center of mass is zero

$$\frac{\mathrm{d}^2\mathbf{R}}{\mathrm{d}t^2} = \mathbf{0} \tag{2.66}$$

Therefore, we can define an inertial reference frame with the center of the mass at the origin, so $\mathbf{R} = \mathbf{0}$. Then, for our position vectors, we obtain relations

$$\mathbf{r}_1 = -\frac{\mu_\mathrm{m}}{m_1}\mathbf{r} \quad \text{and} \quad \mathbf{r}_2 = \frac{\mu_\mathrm{m}}{m_2}\mathbf{r} \tag{2.67}$$

Furthermore, by shifting the origin to the center of mass, there are two additional results we can derive. One of them is that the sum of the lengths of the position vector equals to the length of the separation vector. In other words,

$$|\mathbf{r}| = |\mathbf{r}_1| + |\mathbf{r}_2| \tag{2.68}$$

Next, the ratio of the lengths gives us relation

$$\frac{|\mathbf{r}_1|}{|\mathbf{r}_2|} = \frac{m_2}{m_1} \tag{2.69}$$

Mathematically, the two-body problem is equivalent to a one-body problem with the total mass $M = m_1 + m_2$. The equations (2.44) and (2.67) imply that the lengths of the semi-major axis are

$$a_1 = \frac{\mu_\mathrm{m}}{m_1} a \quad \text{and} \quad a_2 = \frac{\mu_\mathrm{m}}{m_2} a \tag{2.70}$$

where a is the length of the semi-major axis in the one-body problem with center mass M.

We now turn to the velocities by differentiating Eq. (2.67) with respect to time

$$\mathbf{v}_1 = -\frac{\mu_\mathrm{m}}{m_1}\mathbf{v} \quad \text{and} \quad \mathbf{v}_2 = \frac{\mu_\mathrm{m}}{m_2}\mathbf{v} \tag{2.71}$$

Let us focus on $\mathbf{v}$ because it allows us derive velocities of the bodies $\mathbf{v}_1$ and $\mathbf{v}_2$. First, we derive the components in polar coordinates. From geometry, we have angular component

$$v_\phi = r\frac{\mathrm{d}\phi}{\mathrm{d}t} = \frac{\ell(1 + e\cos\phi)}{a(1-e^2)} \tag{2.72}$$

For the radial component, we use the definition of velocity

$$v_r = \frac{\mathrm{d}r}{\mathrm{d}t} = \frac{\ell e \sin\phi}{a(1-e^2)} \tag{2.73}$$

Using the transformation between polar and Cartesian coordinates derived in (D), we obtain

$$v_x = -\frac{\ell\left[e\sin\phi_0 + \sin(\phi+\phi_0)\right]}{a(1-e^2)} \quad \text{and} \quad v_y = \frac{\ell\left[e\cos\phi_0 + \cos(\phi+\phi_0)\right]}{a(1-e^2)} \tag{2.74}$$

where ϕ_0 is the general angle at which the semi-major axis lies. Now, we have almost everything needed to describe the radial motion of the stars.

The only remaining step is to calculate the phase $\varphi = \frac{t}{P}$. We recall Eq. (2.50)

$$\ell = r^2\frac{\mathrm{d}\phi}{\mathrm{d}t} \Rightarrow t = \frac{1}{\ell}\int r(\phi)^2\,\mathrm{d}\phi \tag{2.75}$$

Solving the integral and dividing by period, we obtain

$$\varphi = \frac{t}{P} = \frac{1}{2\pi}\left[2\arctan\left(\sqrt{\frac{1-e}{1+e}}\tan\frac{\phi}{2}\right) - \frac{e\sqrt{1-e^2}\sin\phi}{1+e\cos\phi}\right] \tag{2.76}$$

Note that for the circular orbit ($e = 0$), we get the well-known relation between time and the true anomaly $\frac{t}{P} = \frac{\phi}{2\pi}$. There are some model situations in Fig. 2.3 for different eccentricities.

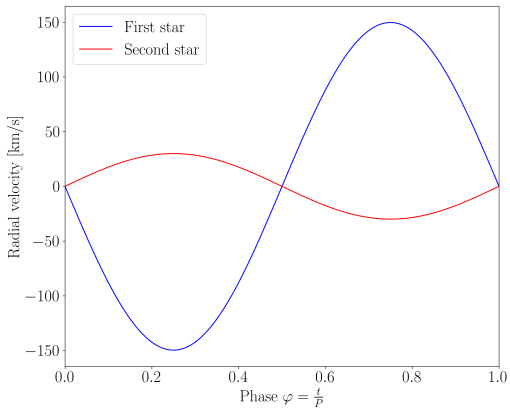

(a) $e = 0.0$

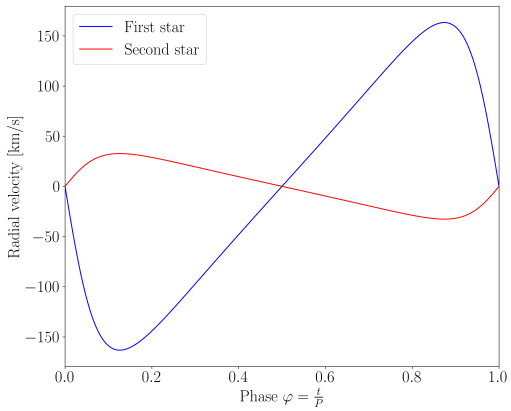

(b) $e = 0.4$

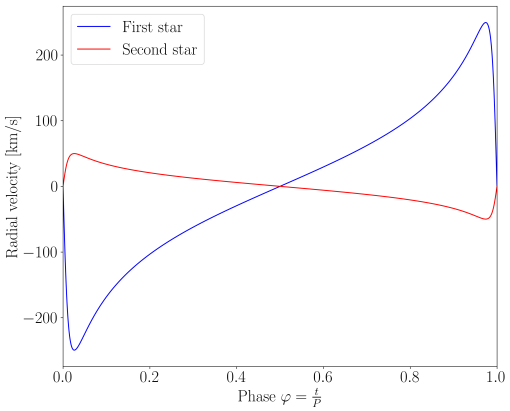

(c) $e = 0.8$

Figure 2.3: Model of radial velocities of the binary stars system with an eccentricity.

2.3.3 Roche limit

We would like to introduce the Roche limit. In celestial mechanics, the first body can cause the destruction of the second body because of its tidal forces. As a star gets closer to the compact object it is orbiting, the star's velocities must increase. Our goal is simple: to calculate the limit at which the last possible orbital trajectory occurs and to determine how fast the star will orbit. At that orbit, the orbital velocity must be at its fastest, and the effect of the rate of change of the intensity in a photometric filter due to the radial velocity must be the highest. Let us calculate the difference between the acceleration on the object's surface and the center of the object. We obtain

$$\Delta a = -\frac{GM}{(r-R)^2} - \left(-\frac{GM}{r^2}\right) \cong -2\frac{GM}{r^3}R. \tag{2.77}$$

We need to include the rotation of the object, which is usually in co-rotation, because of the strong gravitational field. Using the centripetal force, we get the following

$$\Delta a_{\mathrm{c}} = -2\frac{GM}{r^3}R_{\mathrm{o}} - \omega^2 R_{\mathrm{o}}, \tag{2.78}$$

where ω can be calculated from the third Kepler law and we obtain

$$\Delta a_{\mathrm{c}} = -3\frac{GM}{r^3}R_{\mathrm{o}}. \tag{2.79}$$

With this, we can now calculate how close an object can get to the heavier component with mass M. As the object holds by its own gravity, it is still stable, therefore

$$g = \Delta a_{\mathrm{c}} \Rightarrow \frac{GM_{\mathrm{o}}}{R_{\mathrm{o}}^2} = 3\frac{GM}{r^3}R_{\mathrm{o}} \Rightarrow r = R_{\mathrm{o}}\left(3\frac{M}{M_{\mathrm{o}}}\right)^{1/3} = R\left(3\frac{\rho}{\rho_{\mathrm{o}}}\right)^{1/3}. \tag{2.80}$$

This limit tells us how close we can approach the compact object to not get ripped apart. Also, it could be used to find the effect on stars orbiting supermassive black hole, see Sec. 4.5. Lastly, let us determine the minimal orbital period

$$P_{\min} = \sqrt{\frac{4\pi^2 r^3}{G(M_{\mathrm{o}}+M)}} = \sqrt{\frac{12\pi^2 R_{\mathrm{o}}^3}{G(M_{\mathrm{o}}+M)}\frac{M}{M_{\mathrm{o}}}}. \tag{2.81}$$

One would say that this is a very rare phenomenon. However, this is a scenario of the future of one of the Mars moons, Phobos. As Phobos gets closer and closer to Mars, it will eventually tear apart in tens of millions of years and turn into a ring around Mars. Another example are comets, which get very close to Jupiter or the Sun. Of course, we note that the concept of the Roche limit is different from the Roche lobe.

2.4 Cosmological redshift

The cosmological redshift is a consequence of the expanding space-time. If we wish to observe distant galaxies, we should switch to the infrared spectrum due to the redshift. The amount of change in wavelength can be determined from radial velocity v_{r} of the galaxy, which can be derived using Hubble–Lemaître law

$$v_{\mathrm{r}} = H_0 \cdot d, \tag{2.82}$$

where H_0 is Hubble–Lemaître constant[5] and d is the proper distance to the galaxy. Today, we can use the so-called *standard candles* to determine the distances. For example, there is a relation between the period of pulsation of Cepheids P, periodic variable stars, and their absolute visual magnitude M_V.

$$M_V = a\log P + b, \tag{2.83}$$

[5]The Hubble-Lemaitre constant expresses the Hubble parameter at the current epoch, $H_0 \equiv H(t_0)$.

where a and b are empirical coefficients. This relation can also be applied to other pulsating stars, such as δ Scuti or RR Lyrae. Another method involves using Type Ia supernovae (SN Ia), since their absolute visual magnitudes are well-known. By measuring the apparent visual magnitude m_V of Cepheids or SN Ia, we can calculate the distance from the distance modulus:

$$m_V - M_V = 5 \log \left(\frac{d}{1 \text{ pc}} \right) - 5. \tag{2.84}$$

With this, we have all the information needed to calculate the radial velocity of the distant galaxy. However, the Hubble–Lemaître constant is not constant across the history of the Universe since it just expresses the Hubble parameter at the current epoch, see the definition above.

Chapter 3

Vyskočil's effect

Vyskočil's effect is a working name for change of observed magnitude due to change of spectral distribution due to radial velocity, gravitational field and other possible effects. In this Chapter, our main goal is to determine corrections in Planck's distribution law for moving objects or strong gravitational fields. So we aim to describe such a phenomena mathematically and give a physical interpretation.

3.1 Physical interpretation

The physical interpretation was already mentioned in the introduction. We mentioned that we used Doppler shift for measuring the radial velocity of the stars using the shift of spectral lines. However, the whole spectrum shifts as well. Planck's distribution law in Eq. (2.21) is only correct for the static source of thermal emission. The equation has to be, therefore, corrected using the following form

$$\boxed{\frac{\mathrm{d}I(\lambda,T,v_\mathrm{r})}{\mathrm{d}\lambda}=\frac{2\pi hc^2}{\lambda^5}(1+v_\mathrm{r}/c)^4\frac{1}{\exp\left[\frac{hc}{\lambda kT}\,(1+v_\mathrm{r}/c)\right]-1},} \tag{3.1}$$

which now depends on three variables: effective temperature T, radial velocity v_r and wavelength λ. Let us see how the spectral distribution will behave, when we set the radial velocity for the black body with temperature $T_\odot = 5778$ K, to[1] $v_\mathrm{r} = 10\,000\ \mathrm{km\cdot s^{-1}}$ in the positive and negative directions. Let us plot this relation even for the black body with the same temperature at rest.

[1] This high velocity occurs only in extreme cases such as stars orbiting super massive black hole.

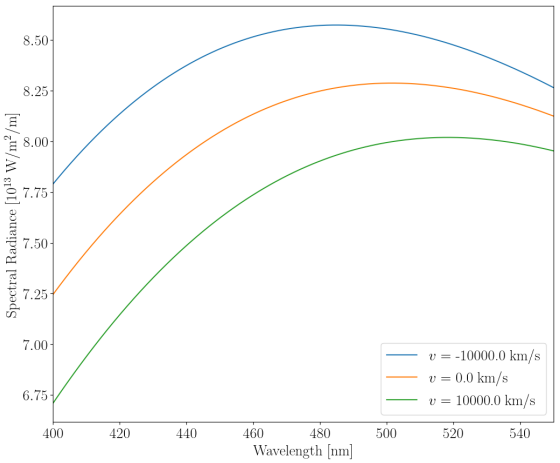

(a) Detailed - first part

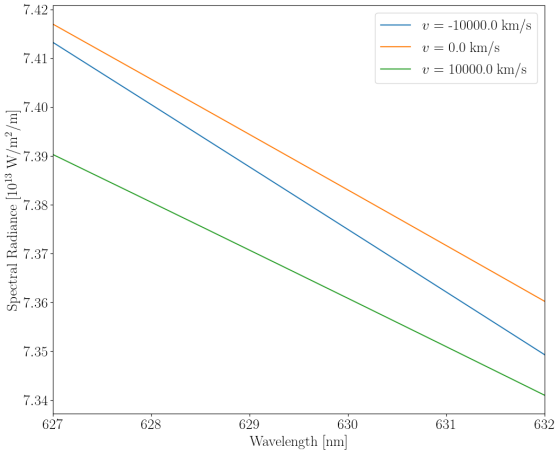

(b) Detailed - second part

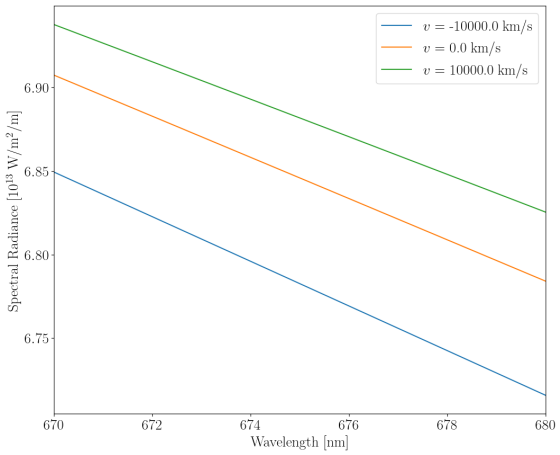

(c) Detailed - third part

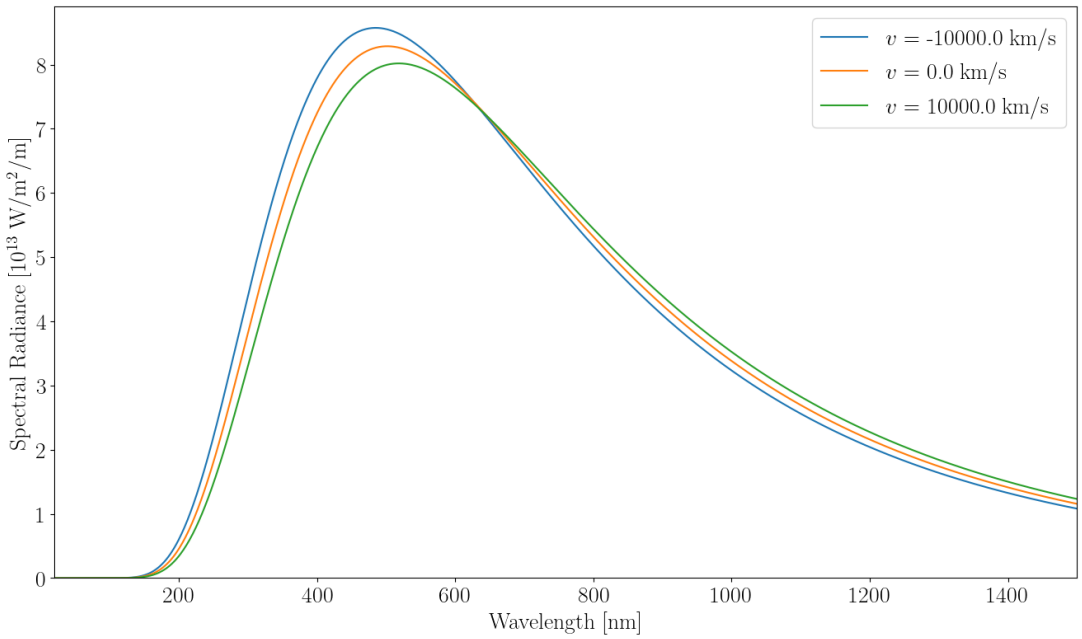

(d) The whole spectral distribution.

Figure 3.1: Planck's corrected spectral distribution.

In the graphs (3.1), we can discover several interesting facts. First, the predicted fact is connected with the shift of the whole spectral distribution. Of course, this leads to the shift of the peak. However, we have not spoken of any change in intensity at peaks. One could admit that the radial velocity might change the whole intensity of the black body. Logically, it does not really make sense because there is no other source of light. Moreover, it seems like it is growing on one side of the peak and decreasing on the other side. This can be supported by the third part of the detailed part of the spectral distribution in the graph (3.1c). We will assume that the whole intensity of the black body radiation will remain the same. Let us prove this statement. Of course, the calculation using the wavelengths is not the best way and we will once again use frequencies. The corrected relation for frequencies has the following form

$$\frac{\mathrm{d}I(f,T,v_\mathrm{r})}{\mathrm{d}f} = \frac{2\pi h f^3}{c^2}\left(1+v_\mathrm{r}/c\right)^4 \frac{1}{\exp\left[\frac{hf}{k_\mathrm{B}T}\left(1+v_\mathrm{r}/c\right)\right]-1}. \tag{3.2}$$

By integrating this relation across all frequencies, we get the total intensity

$$I = \frac{2\pi h}{c^2}\left(1+v_\mathrm{r}/c\right)^4 \int_0^\infty \frac{f^3}{\exp\left[\frac{hf}{k_\mathrm{B}T}\left(1+v_\mathrm{r}/c\right)\right]-1}\,\mathrm{d}f = \frac{2\pi k_\mathrm{B}^4}{c^2h^3}T^4\int_0^\infty \frac{x^3}{\mathrm{e}^x-1}\,\mathrm{d}x. \tag{3.3}$$

Using again the derived value for the integral, we obtain the following result

$$I = \sigma T^4. \tag{3.4}$$

The hypothesis that the total intensity remains the same is proved. Let us calculate the intensity that should be observed through a thin photometric filter. We get

$$I(\lambda,\Delta\lambda,T,v_\mathrm{r}) = 2\pi hc^2\left(1+v_\mathrm{r}/c\right)^4 \int_{\lambda_0}^{\lambda_0+\Delta\lambda} \frac{\lambda^{-5}}{\exp\left[\frac{hc}{\lambda k_\mathrm{B}T}\left(1+v_\mathrm{r}/c\right)\right]-1}\,\mathrm{d}\lambda. \tag{3.5}$$

It was already mentioned that the radial velocity can be connected with shifting of wavelengths in reference frame of the observer. Using substitution of the exponent, we obtain the following.

$$I(\lambda,\Delta\lambda,T,v_\mathrm{r}) = \frac{2\pi k_\mathrm{B}^4T^4}{h^3c^2}\int_{\frac{hc}{(\lambda_0+\Delta\lambda)k_\mathrm{B}T}(1+v_\mathrm{r}/c)}^{\frac{hc}{\lambda_0k_\mathrm{B}T}(1+v_\mathrm{r}/c)} \frac{x^3}{\mathrm{e}^x-1}\,\mathrm{d}x. \tag{3.6}$$

From the new bounds, the shift of the photometric filter is given by:

$$\frac{hc}{\lambda_0k_\mathrm{B}T}(1+v_\mathrm{r}/c), \quad \frac{hc}{(\lambda_0+\Delta\lambda)k_\mathrm{B}T}(1+v_\mathrm{r}/c). \tag{3.7}$$

The fraction $\frac{hc}{k_\mathrm{B}T}$ is just a scale factor that occurs in static motion as well. However, $(1+v_\mathrm{r}/c)$ is characteristic of the shift of the photometric filter. In other words, the radial velocity can be interpreted as a shift of working wavelengths of the photometric filter.

3.2 Relativistic Doppler shift, gravitational Doppler shift and cosmological redshift

As we mentioned earlier, in Sect. 3.1, corrected equation can be written as follows:

$$\boxed{\frac{\mathrm{d}I(\lambda,T,z)}{\mathrm{d}\lambda}=\frac{2\pi hc^2}{\lambda^5}z^4\frac{1}{\exp\left(\frac{hc}{\lambda kT}z\right)-1},} \tag{3.8}$$

where z[2] is the factor related to the observed and emitted wavelength (frequency if you wish). In general,

$$\boxed{\frac{\lambda_\mathrm{o}}{\lambda_\mathrm{e}}=\frac{f_\mathrm{e}}{f_\mathrm{o}}=z.} \tag{3.9}$$

For example, the z factor can be in a relativistic Doppler shift

$$z=\sqrt{\frac{1+v_\mathrm{r}/c}{1-v_\mathrm{r}/c}}. \tag{3.10}$$

Similarly, we can use the gravitational redshift

$$z=\left(1-\frac{2GM}{c^2r}\right)^{-\frac{1}{2}}. \tag{3.11}$$

For cosmological redshift, there is almost the same relation as for Doppler shift. Let us return again to the corrected equation (3.8) and calculate the integral. Using substitution

$$I=\frac{2\pi k^4T^4}{c^2h^3}\int_{\varepsilon_{1,z}}^{\varepsilon_{2,z}}\frac{x^3}{\mathrm{e}^x-1}\,\mathrm{d}x=\frac{15\sigma T^4}{\pi^4}\int_{\varepsilon_{1,z}}^{\varepsilon_{2,z}}\frac{x^3}{\mathrm{e}^x-1}\,\mathrm{d}x, \tag{3.12}$$

where $\varepsilon_{1,z}=\frac{hc}{(\lambda_0+\Delta\lambda)k_\mathrm{B}T}z$ and $\varepsilon_{2,z}=\frac{hc}{\lambda_0k_\mathrm{B}T}z$ are the energy ratios. Further calculations lead to

$$I=\frac{15\sigma T^4}{\pi^4}\sum_{n=1}^{\infty}\left[\mathrm{e}^{-n\varepsilon_{1,z}}\left(\frac{\varepsilon_{1,z}^3}{n}+\frac{3\varepsilon_{1,z}^2}{n^2}+\frac{6\varepsilon_{1,z}}{n^3}+\frac{6}{n^4}\right)-\right.$$
$$\left.-\,\mathrm{e}^{-n\varepsilon_{2,z}}\left(\frac{\varepsilon_{2,z}^3}{n}+\frac{3\varepsilon_{2,z}^2}{n^2}+\frac{6\varepsilon_{2,z}}{n^3}+\frac{6}{n^4}\right)\right]. \tag{3.13}$$

Setting $\varepsilon_{1,z}=0$ and $\varepsilon_{2,z}\to\infty$, we get

$$I=\sigma T^4. \tag{3.14}$$

However, with general $\varepsilon_{1,z}$ and $\varepsilon_{2,z}$, it can be solved analytically only for each first term, since

$$\boxed{\sum_{n=1}^{\infty}\frac{\mathrm{e}^{-n\alpha}}{n}=-\ln\left(1-\mathrm{e}^{-\alpha}\right).}\text{[3]} \tag{3.15}$$

[2] Note that z is not used as relation between wavelength shift $\Delta\lambda$ and emitted wavelength λ_e.

[3] Derivation can be found in E.

The other infinite sums must be solved numerically. These sums are called polylogarithms, which are defined for $|\mathscr{Z}| < 1$, where $\mathscr{Z}$ is in this case a complex number, and are defined as follows

$$\boxed{\mathrm{Li}_k(\mathscr{Z}) = \sum_{n=1}^{\infty} \frac{\mathscr{Z}^n}{n^k}.} \tag{3.16}$$

3.3 Derivation of the highest effect

We have shown the physical interpretation. Now, it is time to calculate at which wavelength the effect is the greatest. In other words, we would like to derive something similar to the Wien's law but with our effect. Then, we are ready to determine the wavelength for the highest effect and to have effective observations. However, we will start the derivation with frequencies. In other words, we are looking for the maximum of the first derivative of Planck's distribution. Therefore, our goal is to find a solution to the following equation

$$\frac{\mathrm{d}^2}{\mathrm{d}f^2}\left(\frac{2\pi h f^3}{c^2} z^4 \frac{1}{\exp\left(\frac{hf}{k_\mathrm{B}T}z\right) - 1}\right) = 0, \tag{3.17}$$

where $z = 1 + v_\mathrm{r}/c$. Simple calculations lead to

$$6\xi\left[\mathrm{e}^\xi - 1\right]^2 + \xi^3\mathrm{e}^\xi\left[\mathrm{e}^\xi + 1\right] - 6\xi^2\mathrm{e}^\xi\left[\mathrm{e}^\xi - 1\right] = 0, \tag{3.18}$$

where $\xi = \frac{hf}{k_\mathrm{B}T}z$. It is obvious that the solution is for $\xi = 0$, however, it is not a maximum. Using numerical methods in `python`, we obtain the solution for $\xi_\mathrm{max} \approx 0.9662677$, see Fig. 3.2a. Turning back to our initial problem, we get

$$\xi_\mathrm{max} = \frac{hf}{k_\mathrm{B}T}z, \tag{3.19}$$

and hence

$$\boxed{\frac{f}{T}z = \mathscr{J}_\mathrm{max},} \tag{3.20}$$

where $\mathscr{J}_\mathrm{max} = 20.13375 \cdot 10^9\ \mathrm{s}^{-1}\cdot\mathrm{K}^{-1}$ is the (Vyskočil's) constant. However, it is not the only solution, because from the distribution we can deduce that there is a solution on the increasing side, which we already have. Moreover, there is still a solution at the decreasing side, which is visible in graph 3.2b. The other value is $\xi_\mathrm{min} \approx 4.6322471$, from which receive a relation

$$\boxed{\frac{f}{T}z = \mathscr{J}_\mathrm{min} = 96.33284 \times 10^9\ \mathrm{s}^{-1}\cdot\mathrm{K}^{-1}.} \tag{3.21}$$

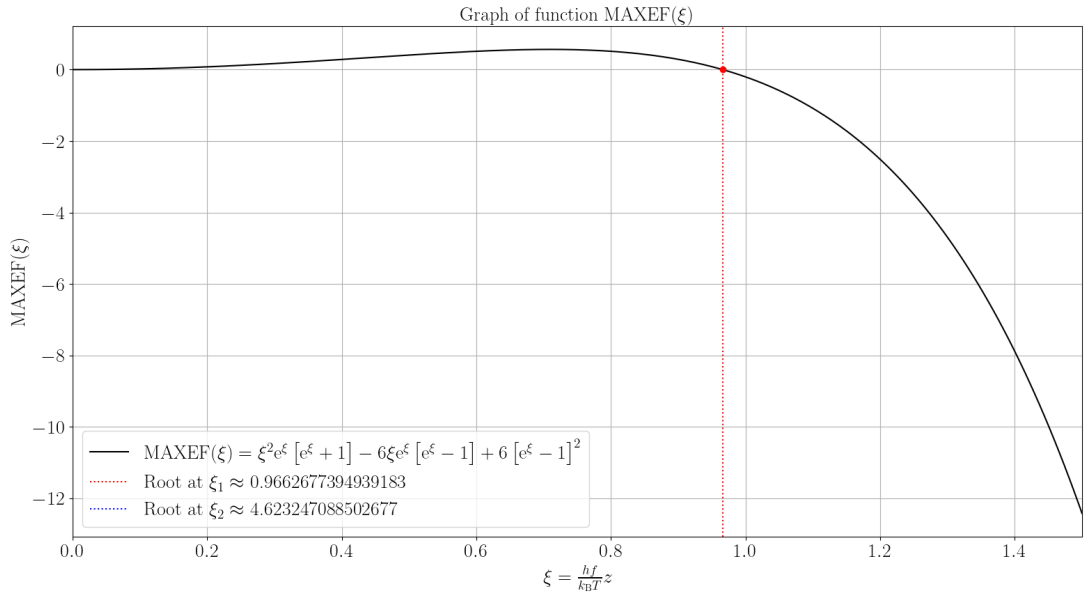

(a) The maximum effect - absolute maximum.

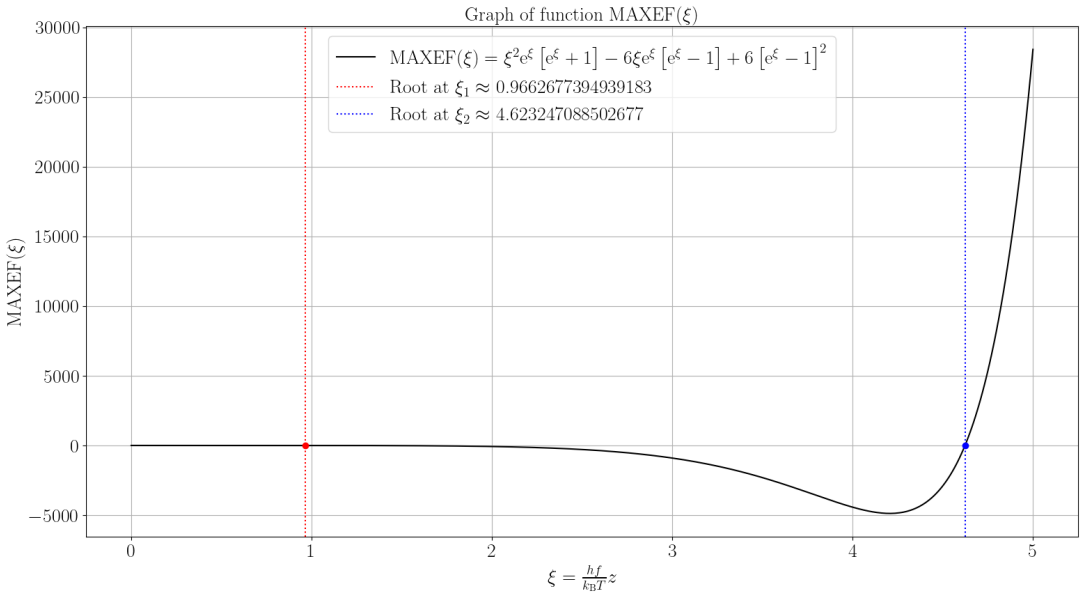

(b) The maximum effect - both solutions.

Figure 3.2: Numerical solution of $f(\xi) = 0$, used to determine the frequency at which the studied effect reaches its maximum. The function $f(\xi) = \xi^2 e^{\xi}\left[e^{\xi}+1\right] - 6\xi e^{\xi}\left[e^{\xi}-1\right] + 6\left[e^{\xi}-1\right]^2$ is shown as a function of $\xi = \frac{hf}{k_B T} z$.

The same method can be used for the determination of the highest effect in wavelengths. One could say that we should use the results from previous calculations. Unfortunately, that would be wrong because there is a different relation. Let us break it down, and lately,

we will show that the results are not the same.

$$\frac{\mathrm{d}^2}{\mathrm{d}\lambda^2}\left(\frac{2\pi hc^2}{\lambda^5}z^4\frac{1}{\exp\left(\frac{hc}{\lambda k_\mathrm{B}T}\right)-1}\right)=0. \tag{3.22}$$

This leads to

$$\eta^2\mathrm{e}^\eta\left(\mathrm{e}^\eta+1\right)-12\eta\mathrm{e}^\eta\left(\mathrm{e}^\eta-1\right)+30\left(\mathrm{e}^\eta-1\right)^2=0. \tag{3.23}$$

Again, using numerical methods in `python`, we obtain the solution for $\eta_\mathrm{max}\approx 8.4445392$, from which we get

$$\boxed{\frac{\lambda T}{z}=\mathscr{V}_\mathrm{max}=1.70380\times 10^{-3}\ \mathrm{m\cdot K}.} \tag{3.24}$$

And the solution at the decreasing side is $\eta_\mathrm{min}=3.5241385$ for which we have

$$\boxed{\frac{\lambda T}{z}=\mathscr{V}_\mathrm{min}=4.082634\times 10^{-3}\ \mathrm{m\cdot K}.} \tag{3.25}$$

The graphs can be seen in Fig. 3.3. In the light of correction, we should change the Wien's displacement law a little to a new form

$$\boxed{\frac{\lambda_\mathrm{max}T}{z}=b.} \tag{3.26}$$

For example, if there is no radial velocity, the Wien's displacement law will be the same as we know it. Now we could possibly plot our solutions in the Planck's distribution to see where are the points with the maximum decrease and increase, and the very maximum; in other words, the Wien's displacement law, see Fig. 3.4.

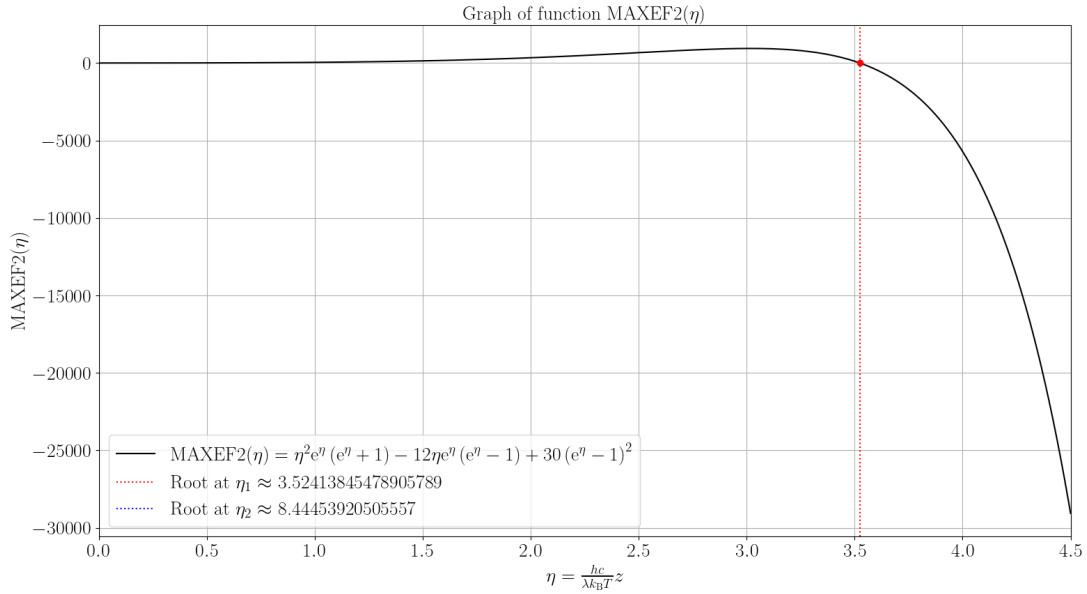

(a) The maximum effect - absolute minimum.

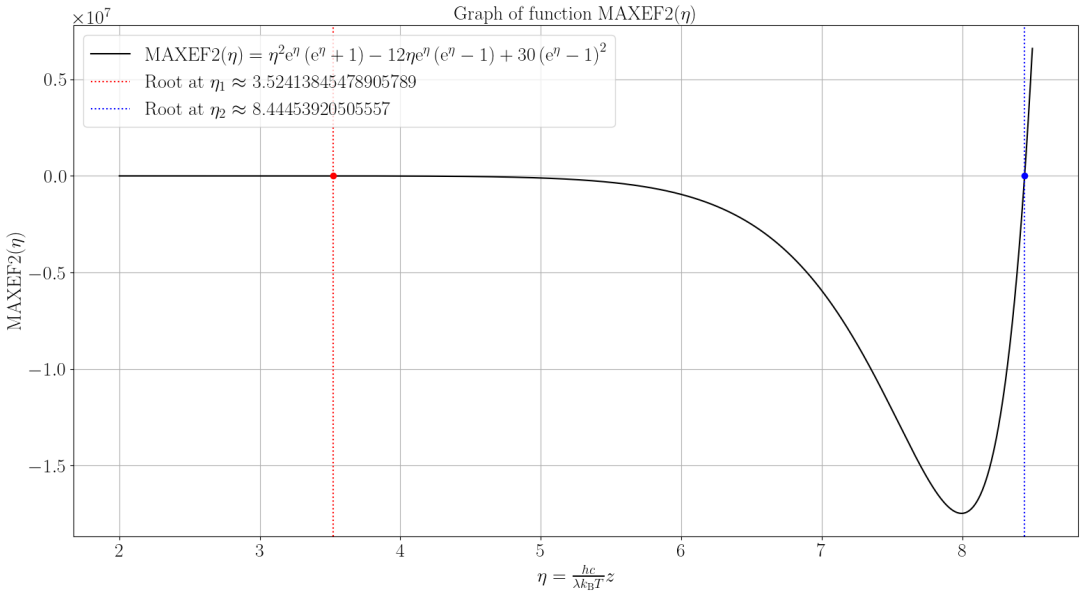

(b) The maximum effect - both solutions.

Figure 3.3: Numerical solution of $f(\eta) = 0$, used to determine the wavelength at which the studied effect reaches its maximum. The function $f(\eta) = \eta^2 e^{\eta}(e^{\eta}+1) - 12\eta e^{\eta}(e^{\eta}-1) + 30(e^{\eta}-1)^2$ is shown as a function of $\eta = \frac{hc}{\lambda k_B T} z$.

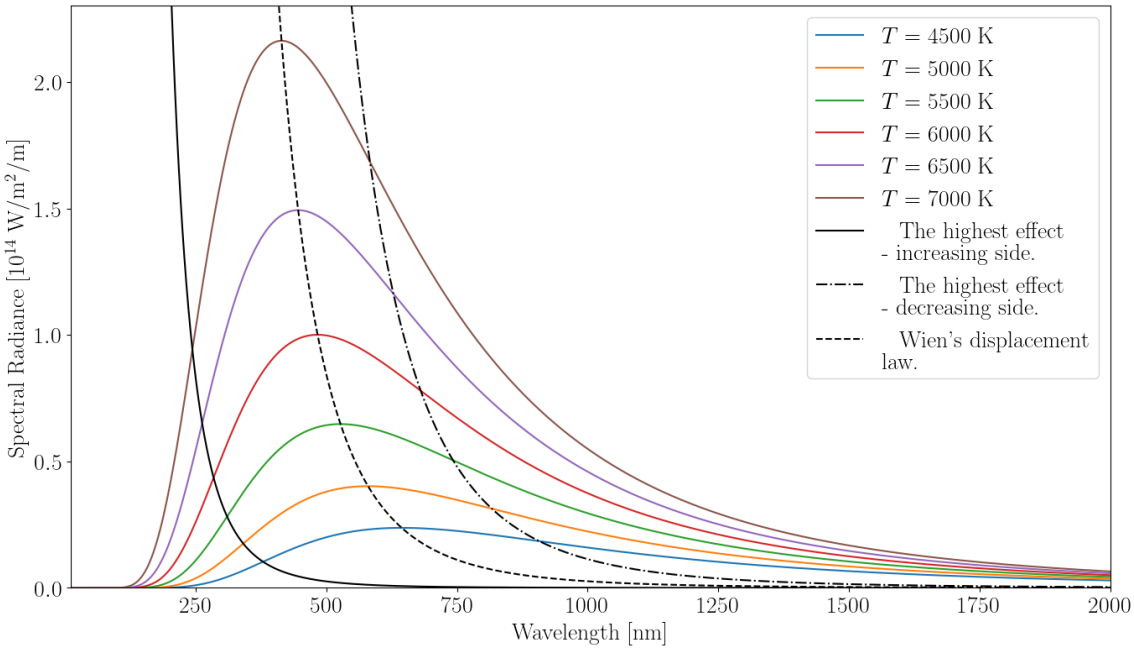

Figure 3.4: Planck spectral distributions for different temperatures. The dashed curve represents Wien's displacement law, while the solid and dash-dotted curves indicate the wavelength regions where the studied effect reaches its maximum on the increasing and decreasing sides of the spectrum, respectively.

Chapter 4

Applications

Let us apply the effect described in the previous chapter to some realistic cases. First, we will begin with isolated stars and then we will also model real systems, where extreme velocities may occur under certain conditions (small distances or large masses involved). At the end we will discuss the problems that could be connected to cosmological distances, the expansion of the universe, peculiar velocities of galaxies in galactic clusters, and other phenomena.

4.1 Effect on main sequence stars

In this section, we will try to demonstrate how this effect can change the observed magnitude of the star. Using the Pogson equation

$$\Delta m = -2.5 \log \left[\frac{I(\lambda, \Delta\lambda, T, v_{\mathrm{r}})}{I(\lambda, \Delta\lambda, T)} \right], \tag{4.1}$$

where Δm is a change in apparent magnitude, $I(\lambda, \Delta\lambda, T, v_{\mathrm{r}})$ is the intensity of the moving object, and $I(\lambda, \Delta\lambda, T)$ is the intensity of the object at rest. The typical radial velocity in e. g. W Ursa Majoris type binaries can reach $300\,\mathrm{km \cdot s^{-1}}$. We will calculate the difference for the visual part of the spectra $\lambda_0 = 550$ (representing V band) nm with the width of the photometric filter $\Delta\lambda = 10$ nm. The results can be found in Figure 4.1.

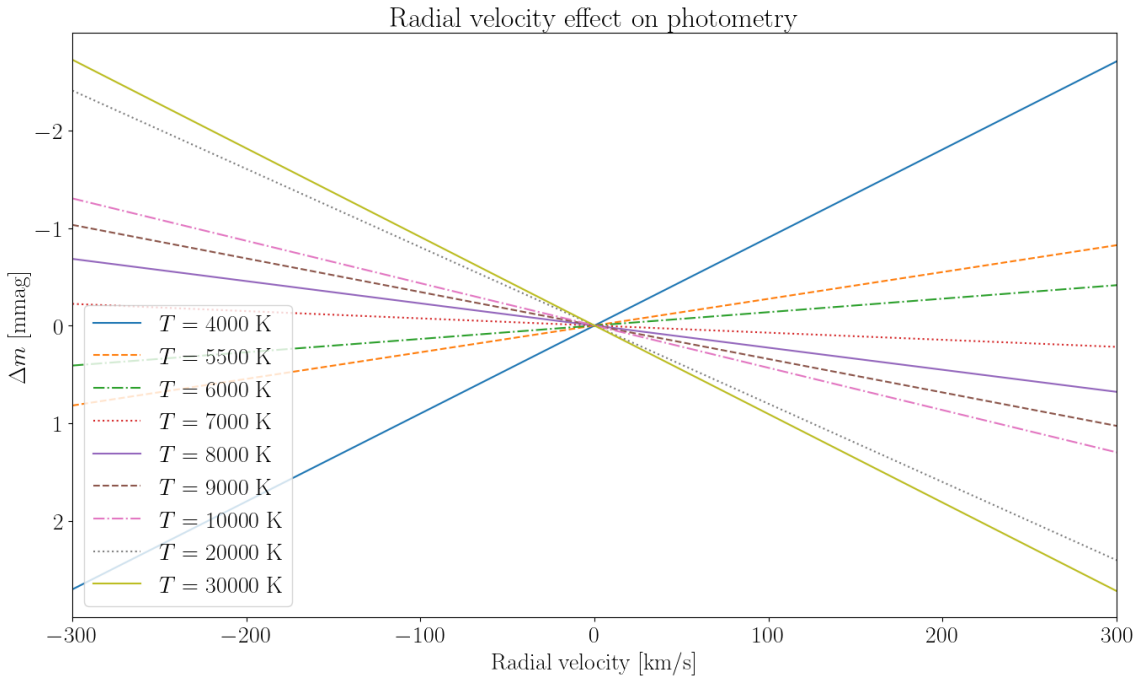

Figure 4.1: The relation between change of apparent magnitude in a photometric filter $\lambda_0 = 550$ nm, $\Delta\lambda = 10$ nm where different line corresponds to different temperature.

It can be observed that, for various temperatures, we obtain a different slope of the graph. That is in agreement with our calculation since for each temperature we are located in a different part of the Planck's distribution. The rate of change is not major, but for some compact systems, where one of the components could be a white dwarf, neutron star or black hole, we could find a rapidly orbiting component. Therefore, the velocities could be significant and that would lead to a higher effect. For example, a non-compact object could orbit near its Roche limit. Using a proper photometric filter could give us even a better result.

4.1.1 US 708

US 708 is the fastest unbound star in our Galaxy with heliocentric radial velocity $v_{\text{helio}} = (917 \pm 7)\ \text{km} \cdot \text{s}^{-1}$, taken from Geier et al. (2015). The parameters of the stars are shown in Table 4.1. From these parameters, one could obtain the mass of the star and the

Parameter	Value
Visual magnitude m_g	(18.668 ± 0.006) mag
Radial velocity v_{helio}	$(917 \pm 7)\ \text{km} \cdot \text{s}^{-1}$
Effective temperature T_{eff}	$(47\,200 \pm 400)$ K
Surface gravity $\log g$	(5.69 ± 0.09)
Distance d	(8.5 ± 1.0) kpc

Table 4.1: Parameters of US 708 obtained from Geier et al. (2015), see their Tab. 1.

proportions of the star. Since we have very precise measurements in 10^{-3} mag, we might start to think about making some corrections to the measured visual magnitude. From Fig. 4.1, we can see that the change in observed magnitude is for 300 $\mathrm{km}\cdot\mathrm{s}^{-1}$ for a lower temperature almost 3 mmag. Let us estimate that for our star it would be 3 mmag, because it tends to grow for higher temperatures. Therefore, for this star, the difference given its radial velocity could be 0.01 mag, which is not a small change. One can object that the precision of obtained distance is not good enough to think about this effect, yet; however, we should consider it. Moreover, the correction exceeds twice the uncertainty of visual magnitude. From this new perspective, let us calculate the radius of the star and the mass of the star. Assume that we will calculate an effective radius, since the star does not have to be spherically symmetric. The area of the star can be estimated as

$$A = 4\pi R_\star^2, \tag{4.2}$$

where $R_\star$ is considered to be our effective radius. From the Stefan–Boltzmann law, we can calculate $R_\star$ as follows,

$$R_\star = d\sqrt{\frac{F_0}{\sigma T_{\mathrm{eff}}^4}} \times 10^{-0.2 m_{\mathrm{g}}}. \tag{4.3}$$

Using the parameters in Tab. (4.1), we obtain $R_\star = (0.021 \pm 0.003)\ \mathrm{R}_\odot$. For the effective mass, we can use

$$M_\star = R_\star^2 \frac{g}{G}. \tag{4.4}$$

The calculation leads to a value of $M_\star = (79 \pm 25) \times 10^{-3}\ \mathrm{M}_\odot$. When compared to the data obtained from Geier et al. (2015), see Tab. 4.2, it must be stressed that the change

Parameter	Value
Star radius $R_\star$	not included $\mathrm{R}_\odot$
Star mass $M_\star$	adopted 0.3 $\mathrm{M}_\odot$

Table 4.2: Results for US 708 from Geier et al. (2015).

by 0.01 mag in m_{g} does not make a big difference, however, we should consider it especially for high-velocity stars, for which the effect is maximized.

4.2 Binary systems

There are many, in fact half or more stars that are found to be bound in binary systems. We will focus our tests mainly on objects with periodic radial motion. First, we will try to demonstrate the effect in classic cases with no compact companion. Then, we will try to apply the calculations to systems with a compact companion, where due to the bigger difference in masses radial velocities are expected to be larger. Since we have two sources of radiation, it is difficult to decide which effective temperature gives a higher effect. Let us introduce a statistic which will help us decide for which temperature to choose the right photometric filter. Since the luminosity of the object is proportional to its area, we can write $L \sim R^2$. Therefore, the area, or the radius, of the object will help us to determine the temperature T_{det} using

$$T_{\mathrm{det}} = \frac{T_1 R_1^2 + T_2 R_2^2}{R_1^2 + R_2^2}. \tag{4.5}$$

The effect on the system, or change of the magnitude for the whole system, was calculated using the formula:

$$\Delta m = -2.5 \log \left[\frac{S_1 I(\lambda, \Delta\lambda, T_1, v_{\mathrm{r},1})_1 + S_2 I(\lambda, \Delta\lambda, T_2, v_{\mathrm{r},2})_2}{S_1 I(\lambda, \Delta\lambda, T_1)_1 + S_2 I(\lambda, \Delta\lambda, T_2)_2} \right], \tag{4.6}$$

where S_1 and S_2 are the areas of the sources, $I(\lambda, \Delta\lambda, T_1, v_{\mathrm{r},1})_1$ is the intensity observed from the first star with a radial velocity and $I(\lambda, \Delta\lambda, T_2, v_{\mathrm{r},2})_2$ is the intensity observed from the second star dependent on its radial velocity. In binary star cases, the areas will not cancel out, and we have to take them into account. In our model, we set the inclination $i = 90^\circ$ and the eccentricity $e = 0$. Fortunately, we derived the formula for the non-ideal cases in Sect. 2.3.2, where the relations for the radial velocity for the trajectory with eccentricity and inclination can be found.

Note that not all stars have a spherically symmetric profile since there are tidal forces from the second companion. Since there are many effects, such as limb darkening, the von Zeipel theorem (von Zeipel (1924)) $T_{\mathrm{eff}} \sim g^{1/4}$, etc., we will neglect them to keep the problem as simple as possible, yet complex enough to obtain a reasonable estimation.

Firstly, we would like to study theoretical systems to derive some relations. To find the minimal orbital period, we apply the Roche limit to estimate the realistic limit. Then, we will try to model realistic systems such as AB And or MY Cam, which are representative of the W UMa binaries type. The W UMa binaries are contact systems in which the components have a common envelope. Therefore, their orbital velocities often exceed 200 $\mathrm{km \cdot s^{-1}}$, which might lead to a greater effect.

4.2.1 Modified Antares-like system

In this subsection, we will aim to study an Antares-like system. The Antares system consists of two stars with very different temperatures. Antares A is a red supergiant spectral type M1.5Iab-Ib with an effective temperature of 3 600 K, and Antares B is a main-sequence star B2.5V with an effective temperature of 18 500 K (both temperatures obtained from Schröder and Cuntz (2007)). Since the orbital period of companions is estimated at 1 650 days (Kiss, Szabó, and Bedding (2006)), the radial velocity is not significant enough

to make a big difference in the observed light.

Figure 4.2: Infrared image of the Antares region obtained by the WISE satellite. Credit: NASA/JPL-Caltech/UCLA (WISE mission): Wikimedia Commons.

However, systems with such a varied temperature could be a good start to study such phenomena. We will begin with a hypothetical binary system consisting of one hot star and one cold star. Then, our goal will be to study how large the effect can approximately be, by changing the weight of the second component. Unfortunately, this leads to a change in temperature, which leads to the suppression of the effect. The first model was set for the spectral types M0 and B5. These spectral types were chosen because their effective temperatures were closest to those of the Antares system.

Parameter		M0V star	K0V star	A0V star	B5V star
Mass	$[M_\odot]$	0.45	0.90	2.25	4.40
Radius	$[R_\odot]$	0.50	1.00	2.10	3.00
Temperature	[K]	3 900	5 200	9 400	15 500

Table 4.3: The parameters of the hypothetical Antares-like system where the adopted parameters are taken from Mikulášek and Krtička (2013) - table on page 49 and 50.

Next, we tried to match a star for which radiation was still high enough to dominate and

that was a star with the spectral type K0. Lastly, we repeated the same process for the B5 star, which was the dominant one, and got a perfect match with an A0 star. All the stars were main sequence stars since we wanted to make them as close as possible. This could be achieved, since main sequence stars are in general denser than late type stars. This also corresponds to the fact that their radius is smaller. The parameters of each star are shown in Tab. 4.3.

As you can see, we have various types of binaries. Before any calculation, it is necessary to estimate the orbital period. The very useful limiting case would be when both stars touch. However, we are aware that the stars will deform slightly as they get closer to each other. Therefore, we have decided to use the orbital period when the stars should still be detached, in our calculation ($a - R_1 - R_2 \approx 0.6$ R$_\odot$). This condition cannot be used in general, yet it gives us a good estimation of the effect. For the K0+M0 system, we determined that the highest effect should occur for $\lambda_0 = 326$ nm with an orbital period of 10 hours. For B5+M0 and B5+A0 systems, the hotter companion is the dominant one, so we have chosen the filter $\lambda_0 = 108$ nm. The first period is about 12 hours and the period for the system consisting of B5 and A0 main sequence stars was estimated to be 18 hours.

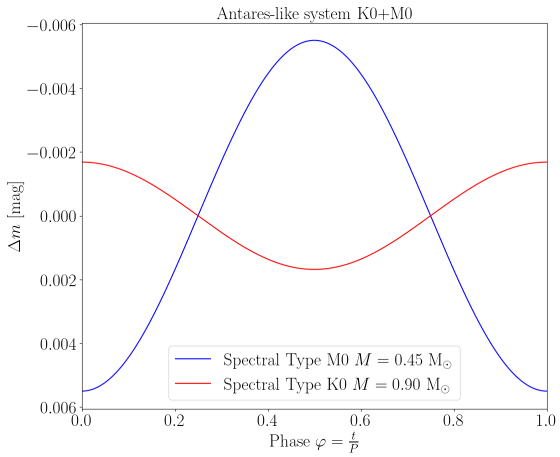

(a) Antares-like system K0+M0 - $\lambda_0 = 326$ nm, $\Delta\lambda = 5$ nm, orbital period 10 h.

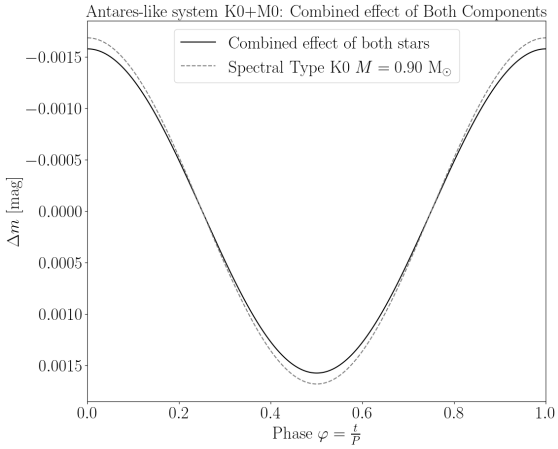

(b) Antares-like system K0+M0: combined effect - $\lambda_0 = 326$ nm, $\Delta\lambda = 5$ nm, orbital period 10 h.

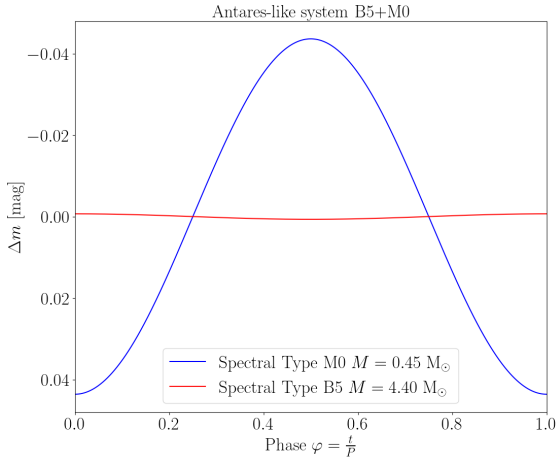

(c) Antares-like system B5+M0 - $\lambda_0 = 108$ nm, $\Delta\lambda = 5$ nm, orbital period 12 h.

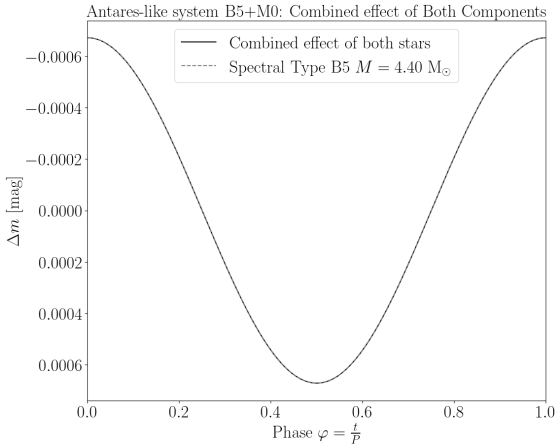

(d) Antares-like system B5+M0: combined effect - $\lambda_0 = 108$ nm, $\Delta\lambda = 5$ nm, orbital period 12 h.

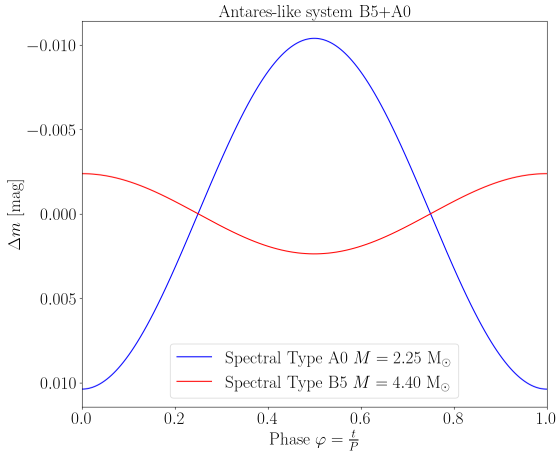

(e) Antares-like system B5+A0 - $\lambda_0 = 108$ nm, $\Delta\lambda = 5$ nm, orbital period 18 h.

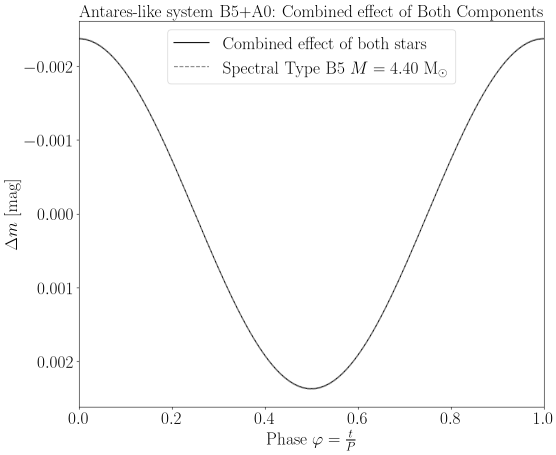

(f) Antares-like system B5+A0: combined effect - $\lambda_0 = 108$ nm, $\Delta\lambda = 5$ nm, orbital period 18 h.

Figure 4.3: Antares-like system.

4.2.2 AB Andromedae - Example of cold EW variable binary

For a cold candidate binary star the AB And system was chosen because of its short orbital period, 0.3319 days. In this case we can expect the effect to be high. Unfortunately, the companions have very similar effective temperatures so the effect will be reduced by their relative motion.

Parameter		AB And A	AB And B
Mass	[$M_\odot$]	1.03	0.58
Radius	[$R_\odot$]	1.15	0.82
Temperature	[K]	5 798	5 450
Spectral type		G5V	G5V

Table 4.4: The parameters of AB And system obtained from Borkovits et al. (2005).

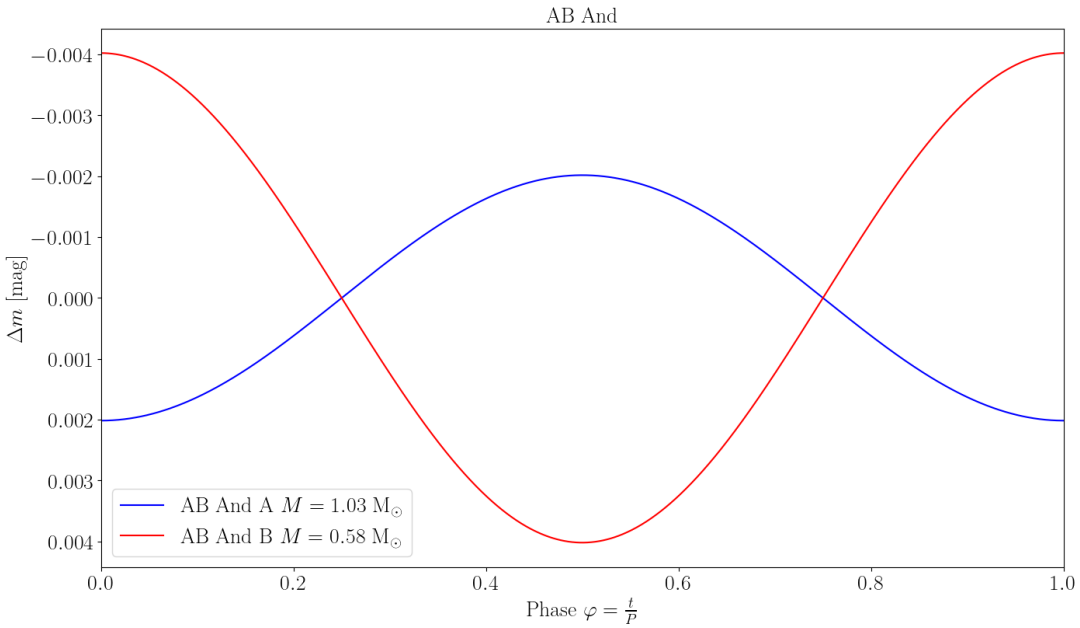

Figure 4.4: AB And: both components separated for $\lambda_0 = 297$ nm and $\Delta\lambda = 5$ nm.

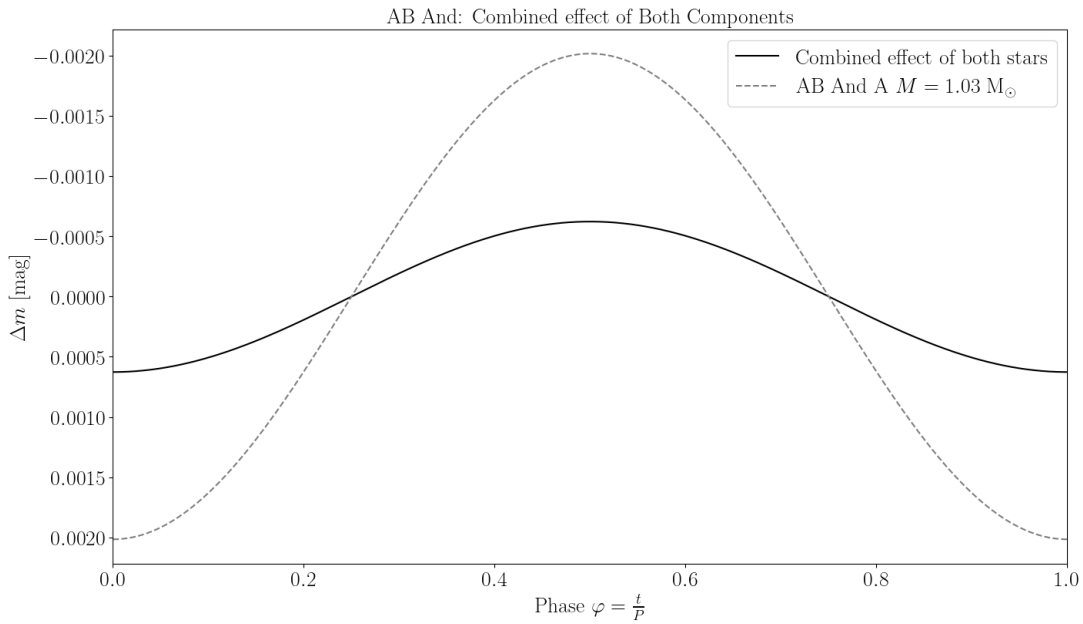

Figure 4.5: AB And: combined effect of both components for $\lambda_0 = 297$ nm and $\Delta\lambda = 5$ nm with comparison with the AB And A alone.

4.2.3 MY Camelopardalis - Example of hot EW variable binary

As a candidate for a binary with hot companions, the MY Cam system was chosen. The orbital period of the system with $i = 62.59°$ is 1.175 days, which makes it a fast orbiting binary. The parameters of the components can be found in Tab. 4.5.

Parameter		MY Cam A	MY Cam B
Mass	$[M_\odot]$	37.7	31.6
Radius	$[R_\odot]$	7.60	7.01
Temperature	[K]	42 000	39 000
Spectral type		O6V	O6V

Table 4.5: The parameters of MY Cam system obtained from Lorenzo et al. (2014)

Fig. 4.6 shows large changes in the observed magnitude compared to its static scenario. It almost seems the effect could reach almost 0.01 mag. However, from Fig. 4.7 we can conclude that in this system the second companion reduces the effect by its own light and we can expect changes slightly above 2 mmag.

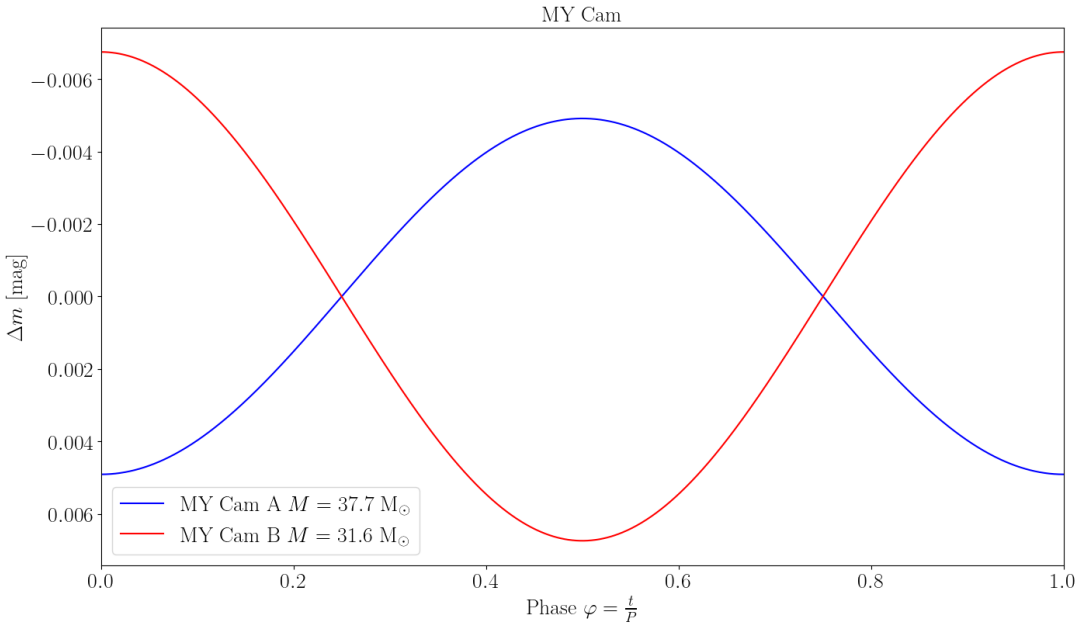

Figure 4.6: MY Cam: both components separated for $\lambda_0 = 40$ nm and $\Delta\lambda = 5$ nm.

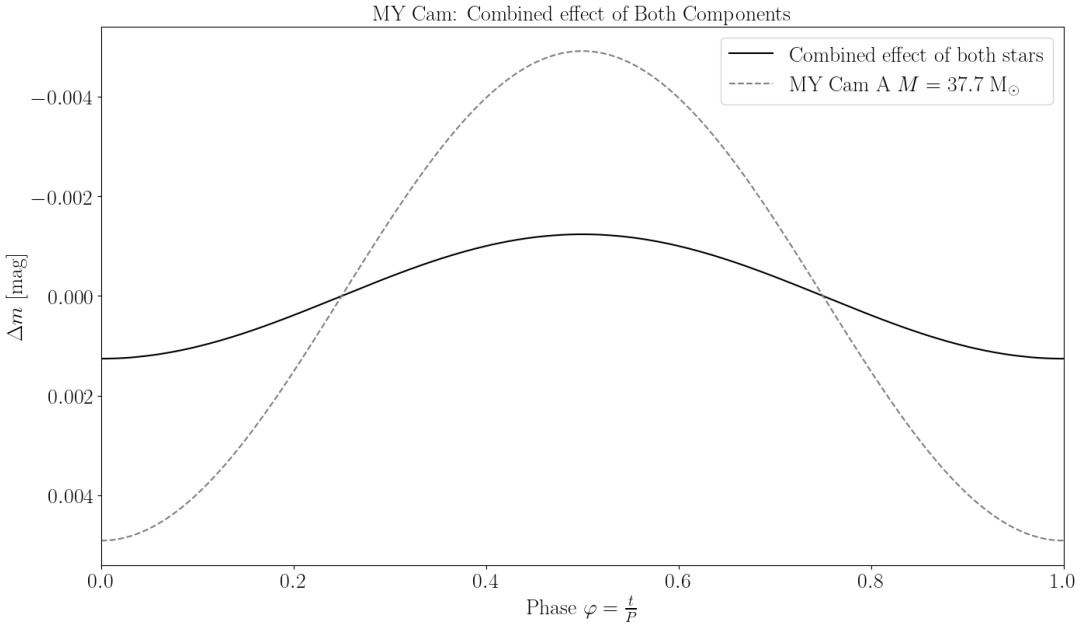

Figure 4.7: MY Cam: combined effect of both components for $\lambda_0 = 40$ nm and $\Delta\lambda = 5$ nm with comparison with the MY Cam A alone.

4.3 Binary systems with a compact companion

4.3.1 Scorpius X-1

In this subsection, we will apply our method to study the Vyskocil's effect for the Sco X-1 system, a low-mass X-ray binary. This system consists of a neutron star and a star on the main sequence. This system was actually the first extrasolar X-ray source discovered. The parameters of companions can be found in Tab. 4.6.

Parameter	Donor star	Neutron star
Mass	0.4 $M_\odot$	1.4 $M_\odot$
Radius	1.25 $R_\odot$	15 km
Temperature	3 000 K	4×10^7 K

Table 4.6: The parameters of Sco X-1 system obtained from Cherepashchuk, Khruzina, and Bogomazov (2021).

The orbital period was determined to be $P = 0.787$ days and the inclination $i = 30°$ (Cherepashchuk, Khruzina, and Bogomazov (2021)). Hence, thanks to the inclination, we can say that the radial velocity is just half of the orbital velocity. Using the obtained parameters, we can use a simple model to estimate the effect.

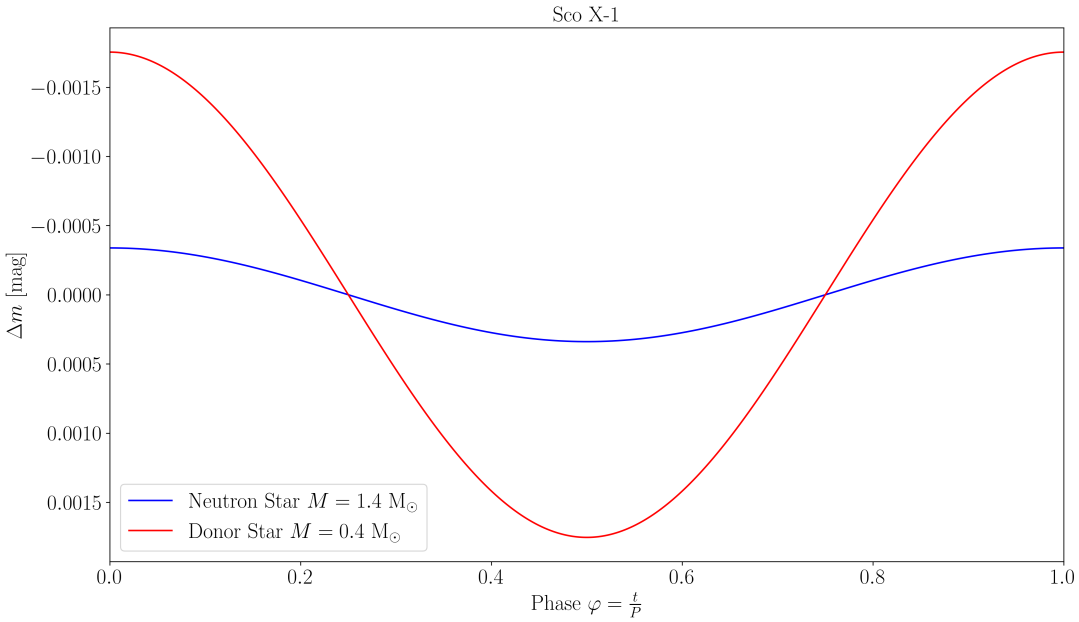

Figure 4.8: Both components

Since the visible companion is 10^4 times larger and the neutron star is heavier, the effect is mostly determined by the donor star in the visible part of the spectrum ($\lambda_0 = 566$ nm, $\Delta\lambda = 5$ nm). Let us study how big the effect is on the X-ray domain. We will use the wavelength range of the Astronomical Roentgen Telescope X-ray Concentrator (ART-XC) (Mereminskiy et al. (2018)) (5-30 keV). It turns out that the donor star is not that bright

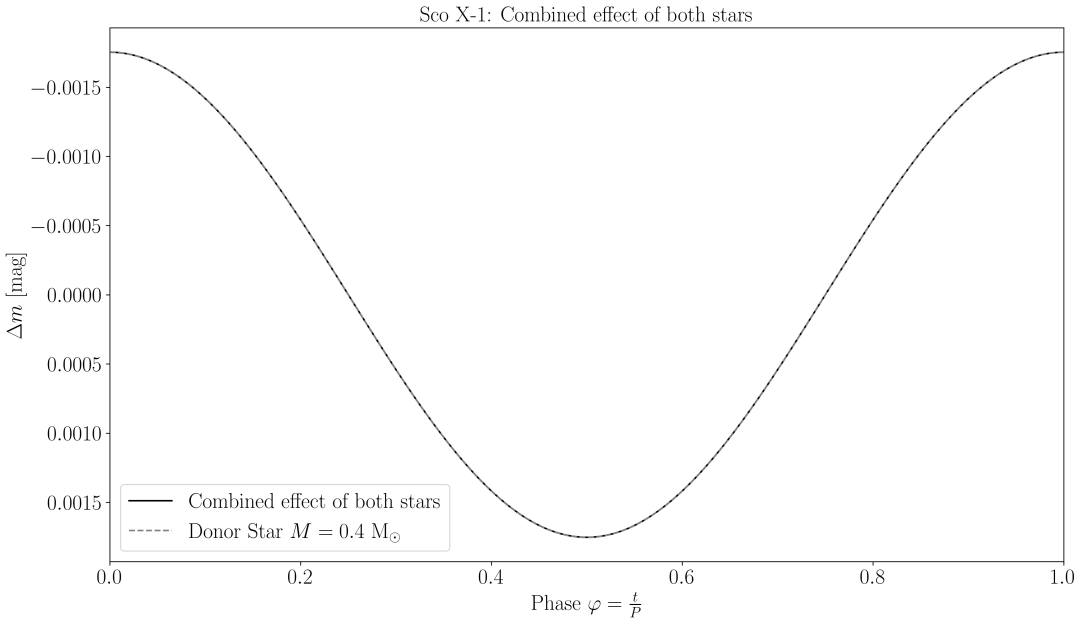

Figure 4.9: Combined effect

in this part of the spectrum. Therefore, the neutron star dominates and it is, unfortunately, heavier. So the effect of the radial velocity is lower, see Fig. 4.10.

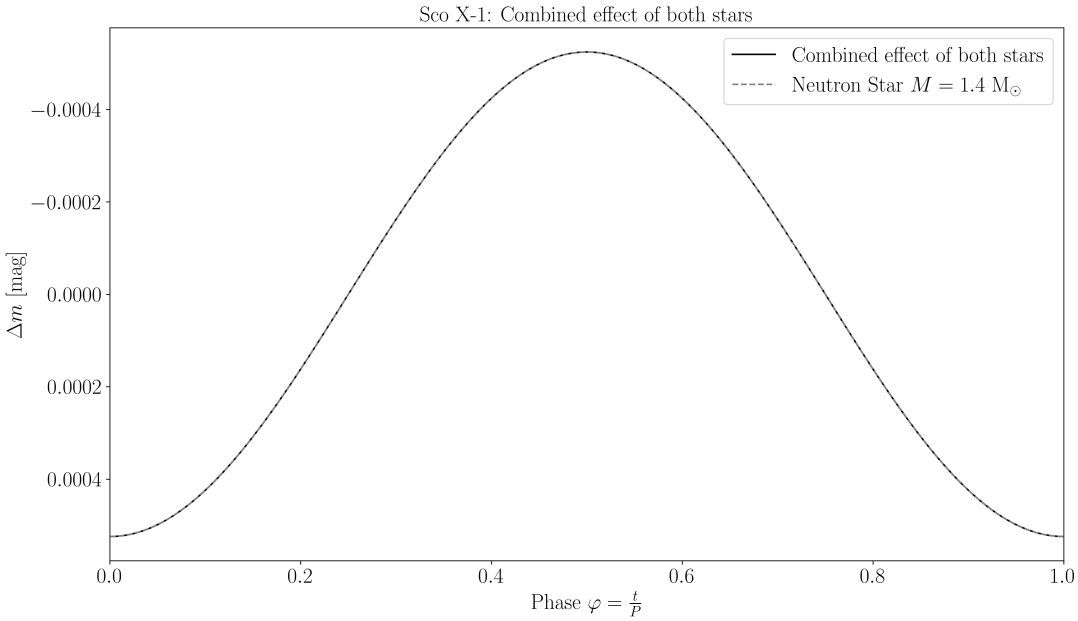

Figure 4.10: Combined effect in range of 5-30 keV.

4.3.2 BP Crucis

The BP Crucis system consists of an X-ray emission source, often called GX 3012, which is a neutron star, and a blue hypergiant. This system may seem like a strong candidate

Parameter	Blue hypergiant star	X-ray Pulsar
Mass	43 $M_\odot$	$\sim$ 1.8 $M_\odot$
Radius	70 $R_\odot$	$\sim$ 8.00 km
Temperature	18 100 K	$\sim 10^6$ K

Table 4.7: The parameters of BP Cru system obtained from Waisberg et al. (2017).

for observing the effect, since there is a big difference in masses of the components, see Tab. 4.7. However, the orbital period is 41.5 days due to the large distance of companions. Therefore, in comparison, we can expect a big effect in change, but in total, the rate of change will not be that big. The obtained eccentricity is $e = 0.462$.

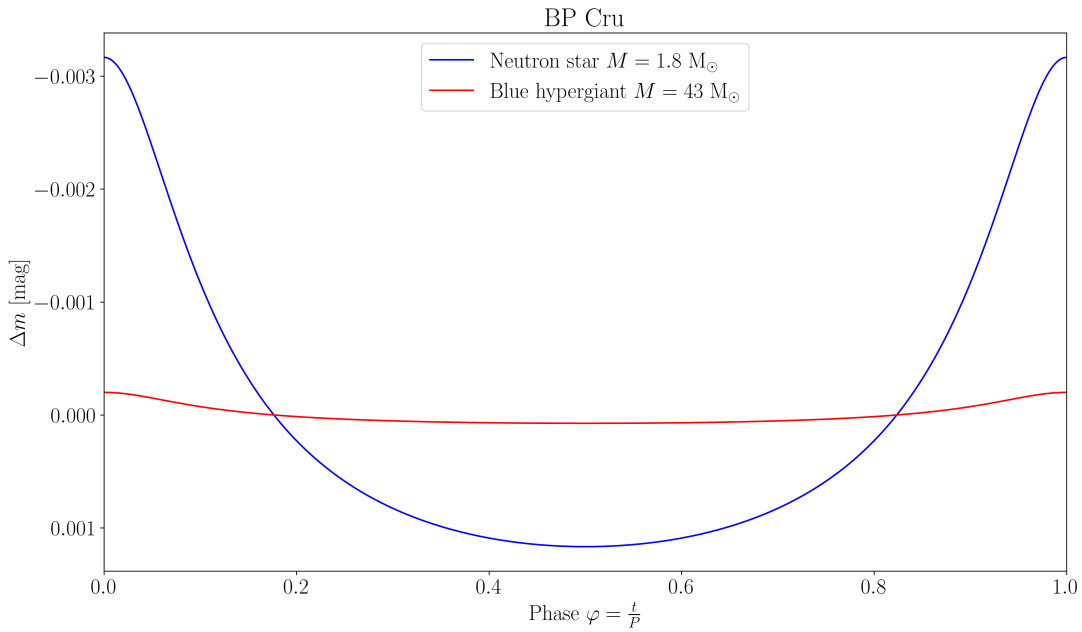

Figure 4.11: Phase curve for both components measured separately in the photometric filter $\lambda_0 = 92$ nm, $\Delta\lambda = 5$ nm.

Most of the light comes to us from the blue hypergiant, so it is not bad to study the rate of change mainly for the more luminous star, for which from statistics (4.5) we get a photometric filter in the UV range. However, the neutron star has to move faster due to the mass difference. This fact motivates us to study this system in the X-ray range. After simple calculations, it can simply be shown, see Fig. 4.13, that the X-ray radiation from the blue hypergiant can be neglected in comparison to that of the neutron star. This leads to a variation in the X-ray part of the spectra.

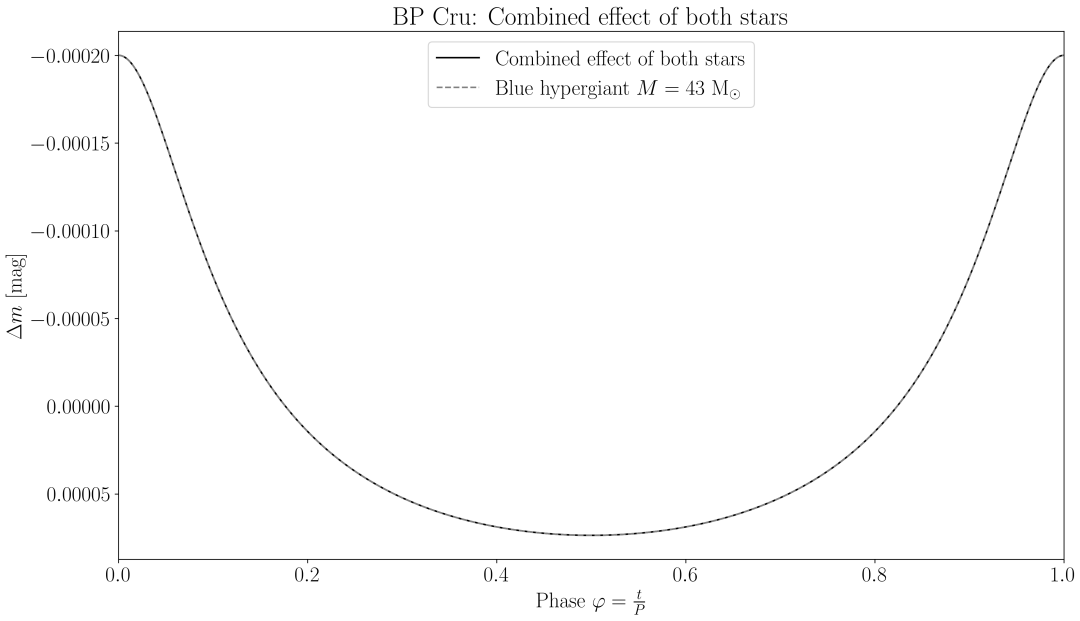

Figure 4.12: Maximum possible observable effect of the whole system in the photometric filter $\lambda_0 = 92$ nm, $\Delta\lambda = 5$ nm.

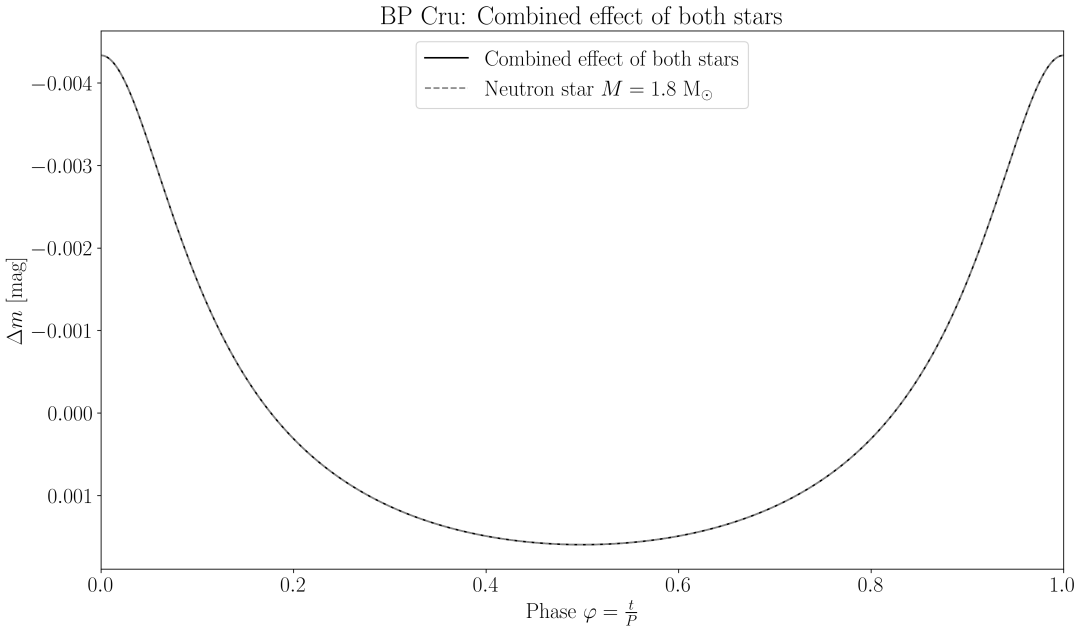

Figure 4.13: Combined effect in the range of 5-30 keV.

4.3.3 Centaurus X-3

Another suitable example is the Cen X-3 system, consisting of an X-ray pulsar, and an evolved star of the spectral type O6-7 II-III (called Krzemiński's Star[1]). The parameters of the components can be found in Tab. 4.8

Parameter	Krzemiński's Star	X-ray Pulsar
Mass	20.50 $M_\odot$	1.21 $M_\odot$
Radius	12.00 $R_\odot$	9.12 km
Temperature	39 000 K	$3.3 \cdot 10^7$ K

Table 4.8: The parameters of Cen X-3 system obtained from Giacconi et al. (1971), Blondin (1994) and Nashed (2023).

The photometric data indicate an orbital period of 2.09 days, which was confirmed by observation of the Doppler that has the periodicity consistent with that of the orbiting pulsar. Using the obtained parameters, we conclude that the highest effect is achieved for the UV range of wavelengths with the central wavelength of $\lambda_0 = 43$ nm.

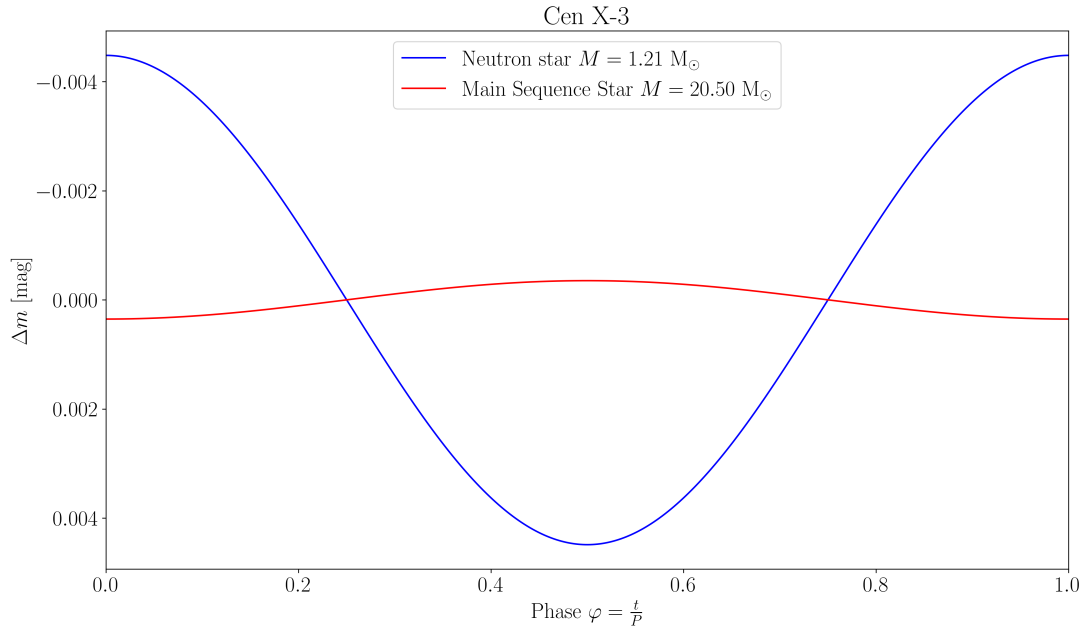

Figure 4.14: Phase curve for both components measured separately in the photometric filter $\lambda_0 = 43$ nm, $\Delta\lambda = 5$ nm.

However, as in the BP Cru case, we may try to study the rate of change in X-ray emission. Once again, we can see the possibility of observing a variation in the X-ray part of the spectra.

[1] Named after it's Polish discoverer.

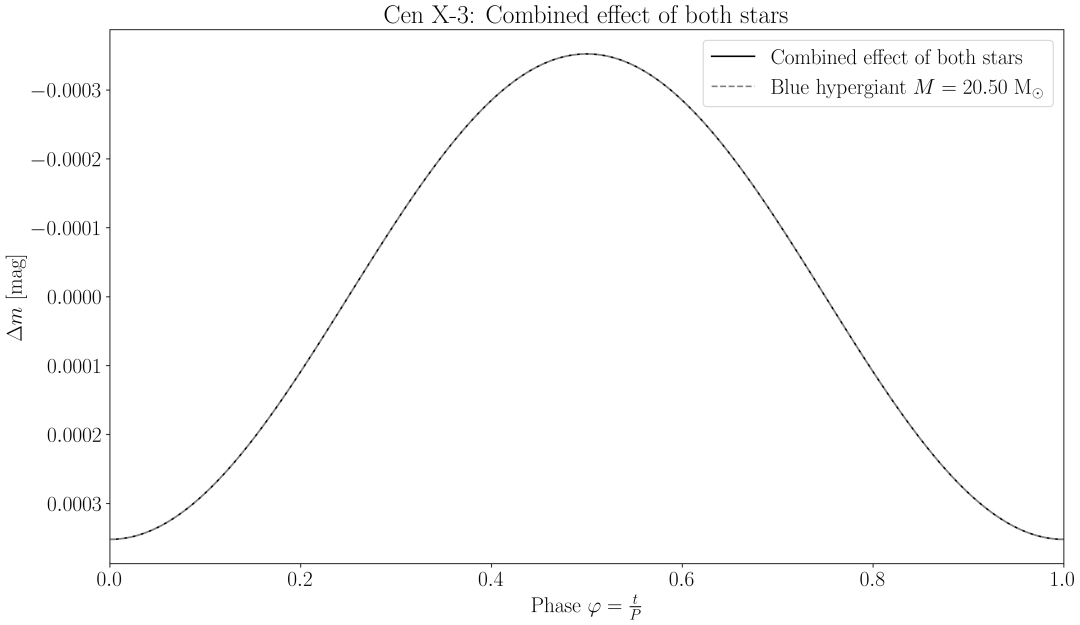

Figure 4.15: Maximum possible observable effect of the whole system in photometric filter $\lambda_0 = 43$ nm, $\Delta\lambda = 5$ nm.

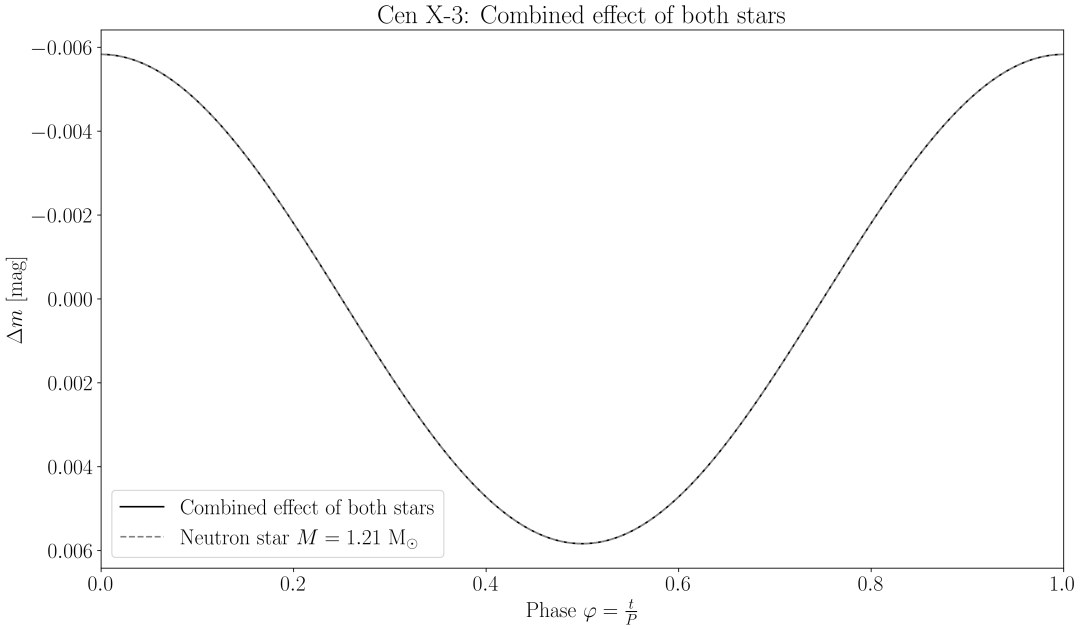

Figure 4.16: Combined effect in range of 5-30 keV.

4.4 Binary systems including a black hole

Binary systems including a black hole can be divided into two cases. The first case which will be studied is when both companions are detached and there is now a Roche-lobe overflow. That is actually the case we would like to study the most since we can determine the realistic chance of discovering "invisible" black holes. Another case we should include is the study of the systems, where the matter is being accreted onto the black hole. Accretion of matter onto black holes usually leads to X-ray emission, which makes the object visible. A good example of such an object is the well-known Cygnus X-1 system.

4.4.1 How close can we get?

Our goal is to discover a new stellar black hole (SBH) that does not emit light. In some cases, astrometry is a good way to detect the motion of the star. However, for distant stars, there is an obstacle that the change in position is small. Even if they are relatively close, the star can orbit very close to the SBH, so this can prohibit observations resolving motion. Interferometry could help us with these cases, however, we cannot monitor a large amount of stars continuously. What about spectroscopy? Yes, spectroscopy can be very useful here, but it is a demanding task in astrophysics to study many objects consistently using spectroscopy.

Photometry? Well, it could be a possible way to detect something new. Of course, as in spectroscopy, the geometry of the system plays the major role, mainly the inclination of the system. Before losing all hope, let us study how close can stars get to it's SBH before accretion begins. Using the work of Eggleton (1983), the radius of the secondary Roche lobe $R_{\mathrm{L},2}$ is given by the semi-analytical relation

$$\frac{R_{\mathrm{L},2}}{a} = \frac{0.49q^{2/3}}{0.6q^{2/3} + \ln\left(1+q^{1/3}\right)}, \tag{4.7}$$

where q is the mass ratio $q = \frac{M_2}{M_1}$. Implementing the third Kepler law and solving for the orbital period, we obtain

$$P_{\mathrm{min}} = 2\pi \left[\frac{R_{\mathrm{L},2}^3}{G(M_1+M_2)}\right]^{1/2} \left[\frac{0.6q^{2/3} + \ln\left(1+q^{1/3}\right)}{0.49q^{2/3}}\right]^{3/2}. \tag{4.8}$$

We can deduce that the larger the star, the larger the minimal orbital period, and then the maximal radial velocity is smaller. As stars get closer, their orbits become more circular. Therefore, it is reasonable to expect circular orbits. Then, the magnitude of the maximum orbital velocity ($i = 90^\circ$) of the star is

$$v_2 = \frac{1}{1+q}\left[\frac{G(M_1+M_2)}{R_{\mathrm{L},2}} \frac{0.49q^{2/3}}{0.6q^{2/3} + \ln\left(1+q^{1/3}\right)}\right]^{1/2}. \tag{4.9}$$

Now, it would be good to test how small periods we can reach and how large velocities we could expect.

Main Sequence limit

We will begin with main sequence stars, since they are more compact than post-main-sequence stars, which are in general less dense. Speaking about main-sequence stars orbiting near the SBH, we should not expect any red dwarf, since SBH are mostly evolved in systems consisting of hot stars with high masses. Theoretically, it is possible, and we would obtain physically correct results. However, this kind of system is very rare in the universe. There are several reasons why. First, in this kind of a system the red dwarf should orbit on very large orbits, which is in contradiction with what we want the system to be like. Moreover, on such a distant trajectory, the red dwarf could easily be kicked out by a supernova explosion, more correctly, by the loss of mass of the more massive companion. Therefore, we will take A0V stars as a lower limit. The stellar parameters were obtained from Mikulášek and Krtička (2013).

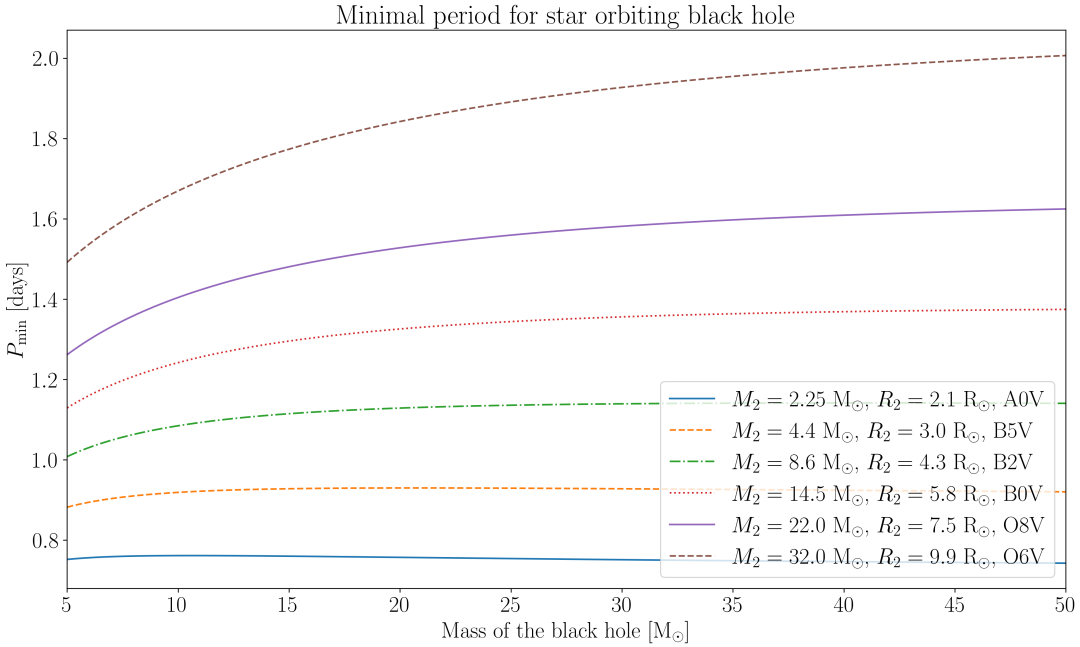

Figure 4.17: Orbital Periods for Main Sequence stars at their limits orbiting the SBH without a Roche-lobe overflow.

Even if we are talking about limiting cases, the orbital periods range from 18 hours to 2 days (Fig. 4.17). Fortunately, for an SBH with a mass around 15 M$_\odot$, the star can reach several hundreds of kilometres per second. This could lead to an effect of around 0.01 mag.

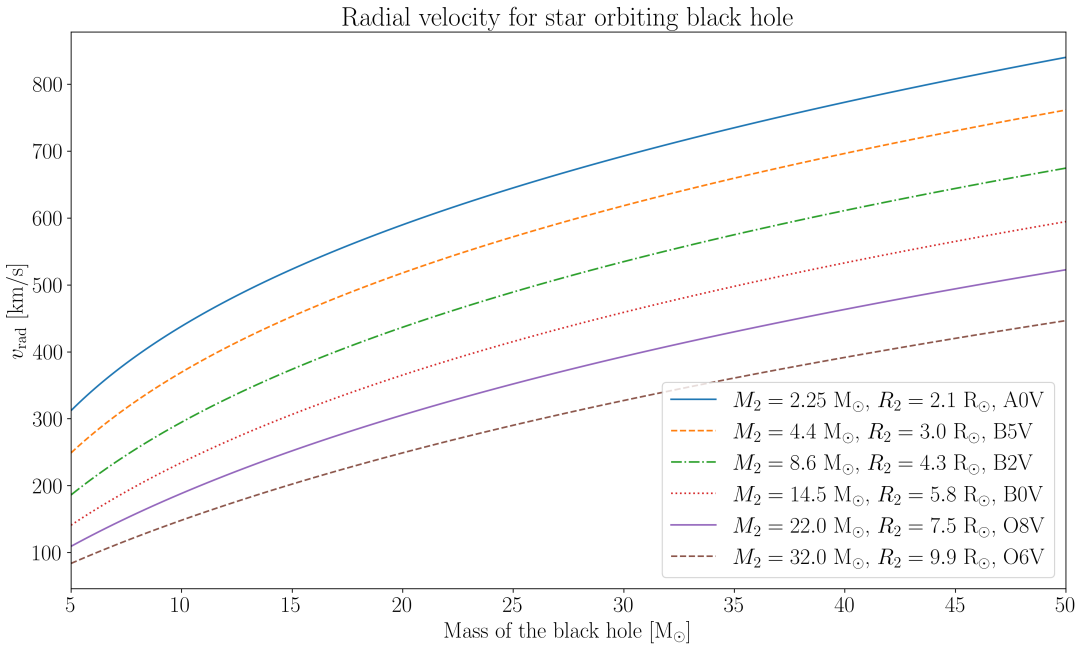

Figure 4.18: Radial velocities for Main Sequence stars at their limits orbiting the SBH without a Roche-lobe overflow.

Post-Main Sequence limit

For post-main-sequence stars, we can expect worse results, since stars are generally less dense and larger. Therefore, the limitation of their orbit will be bigger. Let us now compare with previous results. The stellar parameters were obtained from Mikulášek (2021).

From the results in Fig. 4.19 and 4.20 we can deduce that it is the more probable is to detect the SBH with an orbiting main-sequence star than with a post-main-sequence star. Also, the post-main-sequence stars usually have a strong stellar wind, which can lead to accretion.

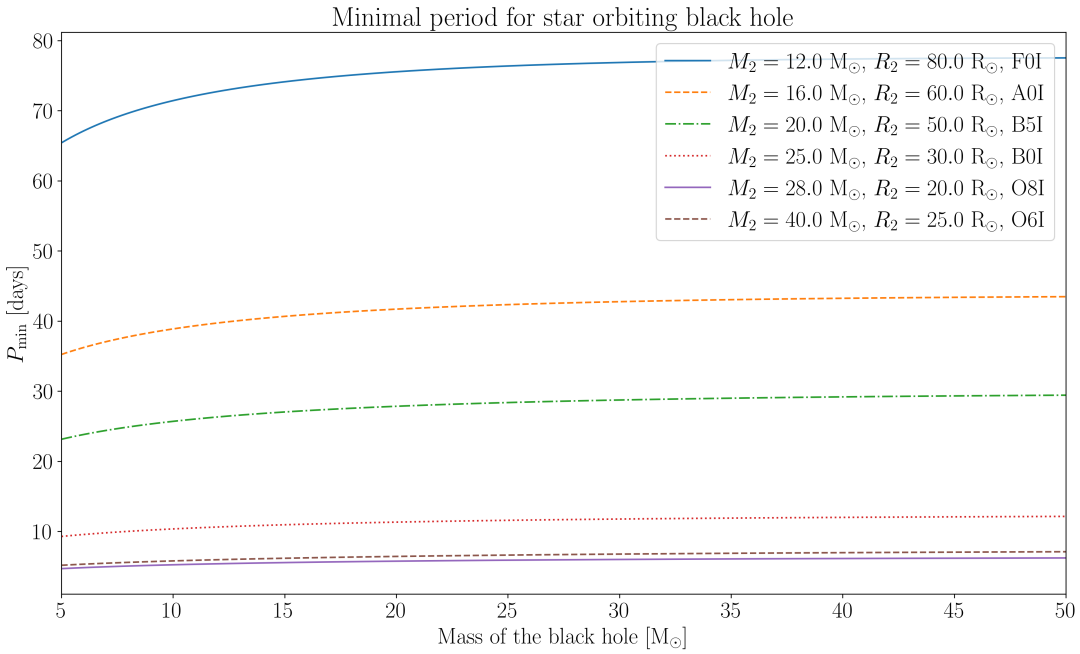

Figure 4.19: Orbital Periods for Post-Main Sequence stars at their limits orbiting the SBH without a Roche-lobe overflow.

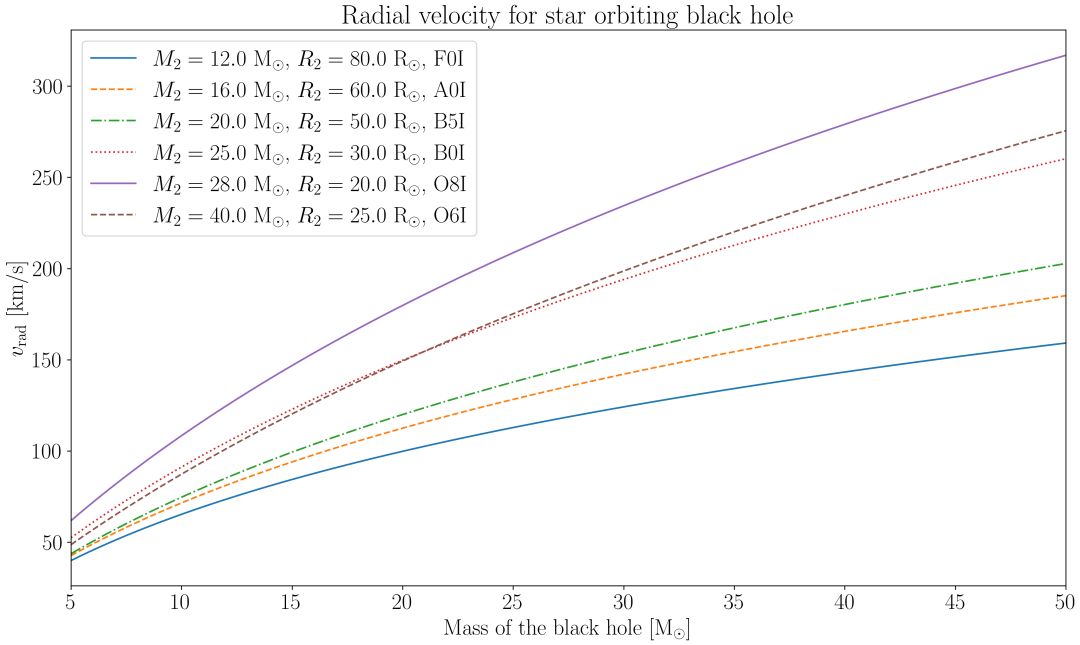

Figure 4.20: Radial velocities for Post-Main Sequence stars at their limits orbiting the SBH without a Roche-lobe overflow.

4.4.2 Binaries with accretion

The process of accretion of matter onto the second companion and the study of accretion disks are among the most important parts of modern astrophysics. Deriving all the necessary stuff can really be demanding for this thesis, which is not our goal. So, we will point out several results that we need for our models (see Frank, King, and Raine (2002) for a review). The accretion disk can be understood as ring at the radius R and with temperature profile $T(R)$. It can be shown that the temperature of the disk is described as a function of the radius R

$$T(R) = \left\{ \frac{3GM\dot{M}}{8\pi R^3 \sigma} \left[1 - \left(\frac{R_*}{R} \right)^{1/2} \right] \right\}^{1/4}, \tag{4.10}$$

where R_* is the radius of the acceptor (the object on which the matter accretes), $\dot{M}$ is the matter accreted per unit of time, and M is the mass of the acceptor. The flux of the accretion disk can be calculated as a function of the wavelength λ as

$$F_\lambda = \frac{4\pi h c^2 \cos i}{D^2 \lambda^5} \int_{R_*}^{R_{\text{out}}} \frac{R \, \mathrm{d}R}{\exp\left[\frac{hc}{\lambda k_{\text{B}} T(R)} \right] - 1}, \tag{4.11}$$

where i is the angle of inclination, R_{out} is the outer radius of the accretion disk. Speaking of black holes, the radius of the acceptor is not a good approach in this case. We need to know how close the last stable orbiting, bound particle is. Using the Schwarzschild metric

$$\mathrm{d}s^2 = g_{\mu\nu} \, \mathrm{d}x^\mu \, \mathrm{d}x^\nu = -c^2 \sqrt{1 - \frac{r_{\text{S}}}{r}} \, \mathrm{d}t^2 + \frac{\mathrm{d}r^2}{\sqrt{1 - \frac{r_{\text{S}}}{r}}} + r^2 \, \mathrm{d}\theta + r^2 \sin^2\theta \, \mathrm{d}\varphi, \tag{4.12}$$

and the geodetic equation

$$\frac{\mathrm{d}^2 x^\mu}{\mathrm{d}\tau^2} + \Gamma^\mu_{\alpha\beta} \frac{\mathrm{d}x^\alpha}{\mathrm{d}\tau} \frac{\mathrm{d}x^\beta}{\mathrm{d}\tau} = 0 \tag{4.13}$$

where $\Gamma^\mu_{\alpha\beta}$ are the Christoffel symbols that can be obtained using the metric $g_{\mu\nu}$

$$\Gamma^\mu_{\alpha\beta} = \frac{1}{2} g^{\mu\gamma} \left(\partial_\beta g_{\alpha\gamma} + \partial_\alpha g_{\gamma\beta} - \partial_\gamma g_{\alpha\beta} \right), \tag{4.14}$$

where we used the notation $\partial_a = \frac{\partial}{\partial x^a}$ and r, θ and φ are classical spherical coordinates, gives us the closest possible stable orbit for a particle $r = 3r_{\text{S}}$, where r_{S} is the Schwarzschild radius[2]. This limit can be used as $R_* = R_{\text{in}} = 3r_{\text{S}}$, where R_{in} is the inner boundary of the accretion disk.

[2] Schwarzschild radius r_{S} is the radius of the event horizon of the non-rotating black hole without charge and is given by $r_{\text{S}} = \frac{2GM}{c^2}$, where G is gravitational constant, M is mass of the black hole, and c is speed of light.

Cygnus X-1

The Cygnus X-1 system is located near η Cygni. This X-ray source consists of the blue supergiant star of the spectral type O9.7, and the first black hole discovered. Since the black hole is accreting mass from its component, the accretion disk is a strong source of the X-ray emission. Since the Cyg X-1 system is still under research, we used parameters from several works, Tab. 4.9, to obtain a reasonable model.

Parameters of the companions		
Parameter	Black hole	Blue super giant
Mass	18 $M_\odot$	31 $M_\odot$
Radius (R_{in} for BH)	160 km	21.8 $R_\odot$
Temperature	-	31 000 K
Other used parameters		
Outer radius R_{out}		26 600 km
Matter accreted $\dot{M}$		$3 \cdot 10^{-7}$ $M_\odot \cdot yr^{-1}$
Inclination i		27°
Eccentricity e		0.018

Table 4.9: The parameters of Cyg X-1 system obtained from Young et al. (2001), Papavasileiou, O. Kosmas, and T. S. Kosmas (2025) and Papavasileiou, O. Kosmas, and T. S. Kosmas (2025).

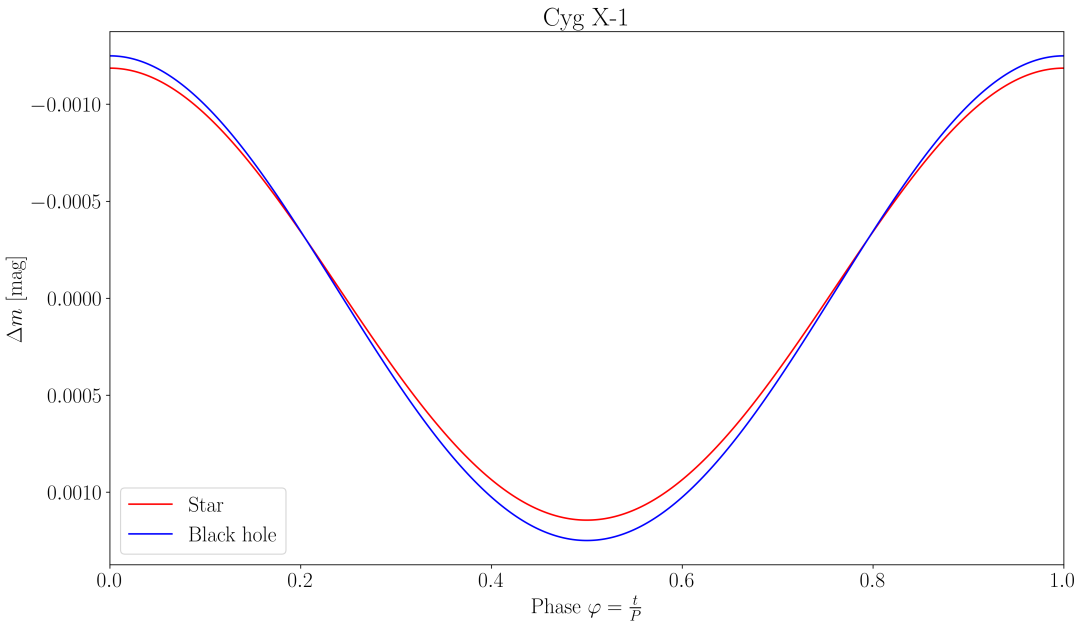

Figure 4.21: Phase curve for both components measured separately in the photometric filter $\lambda_0 = 52$ nm, $\Delta\lambda = 5$ nm.

From Figures 4.21 and 4.22 it is obvious that the effect is not significant and can be estimated as an effect from the previous subsection. Moreover, for these cases the approximation for the disk as the black-body radiation could give us a good estimate how big the effect can be.

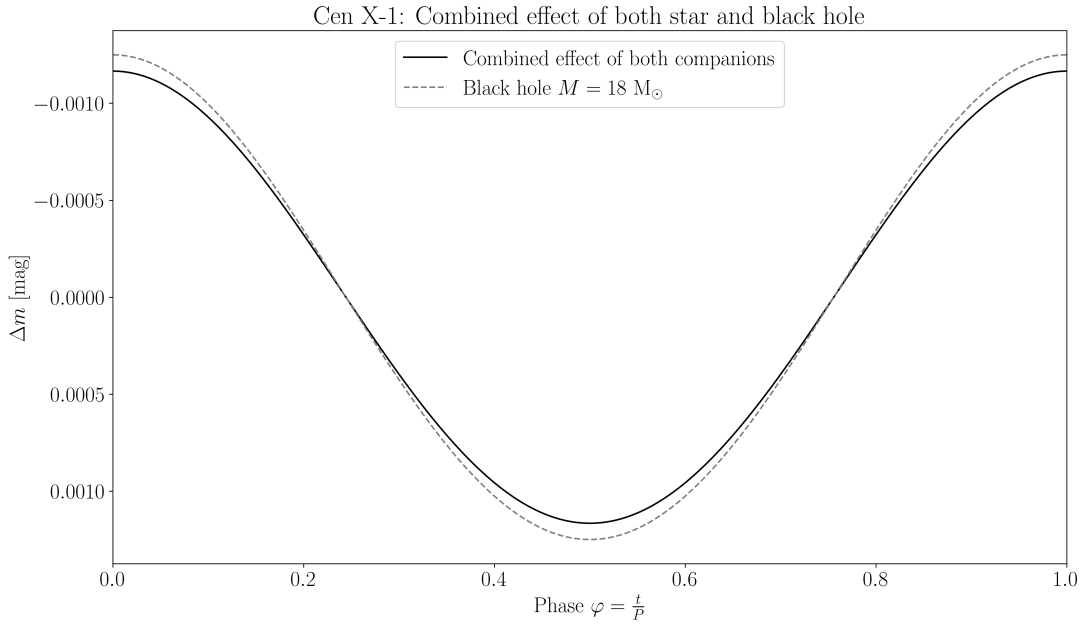

Figure 4.22: Maximum possible observable effect of the whole system in the photometric filter $\lambda_0 = 52$ nm, $\Delta\lambda = 5$ nm.

Note that the emission of the material in the vicinity of the black holes does not have to correspond to the accretion disk. The emission can rather correspond to the standing shock at the Lagrange 1 (L1) point in the binary or to some extent to the bow-shock due to the supersonic motion of the black hole with respect to the overflowing material - see e.g. Čechura and Hadrava (2015).

4.5 Stars orbiting Supermassive Black hole

Today Supermassive Black holes (SMBHs) that are mostly located in galactic nuclei trigger a lot of interest. Since galactic nuclei typically represent very dense stellar systems, in fact one of the densest in the galaxy, it is quite likely that a star can orbit the SMBH very tightly. As we have shown earlier, a close approach of the star to the SMBH might completely destroy it. The star can lose upper layers, and the only remaining part is the hot nucleus of the star. As we observe these hot cores orbiting with high velocities on eccentric trajectories, we might register rapid brightening due to the effect of radial velocity. Let us first study the limits of these systems and then we will focus on S stars and G objects (Zajaček, Pikhartová, and Peissker (2024)).

4.5.1 Extreme cases

The Galactic centre of the Milky Way hosts many stellar objects orbiting the SMBH. Some of these stars orbit the SMBH on very eccentric trajectories. Several tens of such orbits are depicted in Fig. 4.23. In Fig. 4.24 we also show their corresponding radial velocities that can reach $\sim 4\,000\ \mathrm{km}\cdot\mathrm{s}^{-1}$ and hence $\sim 1\%$ of the light speed.

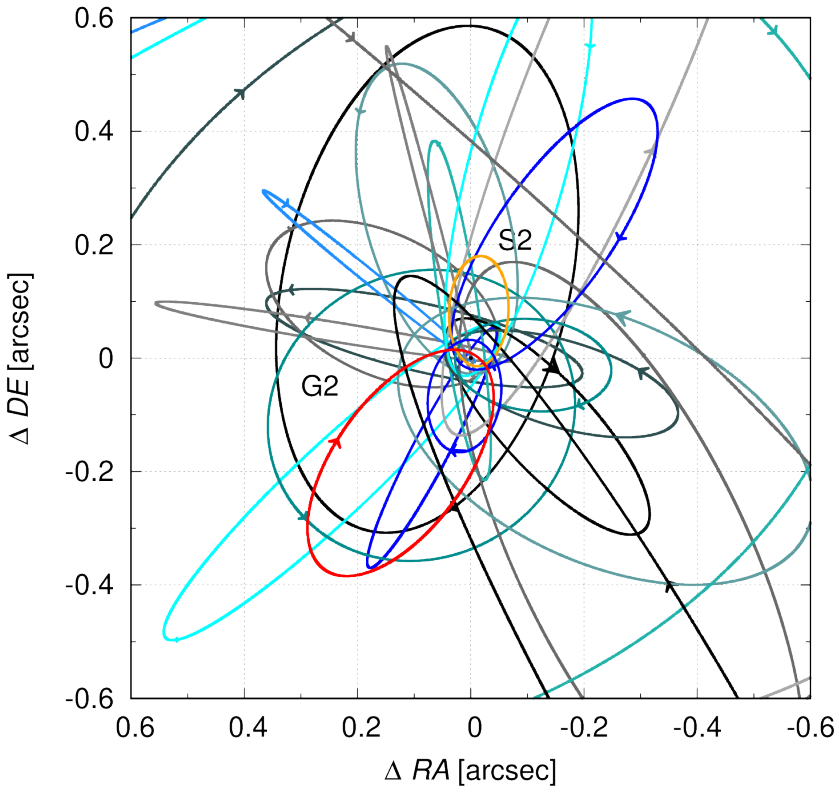

Figure 4.23: Trajectories of S cluster objects around the SMBH associated with the compact radio source Sgr A*. The orange orbit represents the S2 star orbit, while the red colour stands for the G2 orbit. The orbital elements for S stars were taken from Gillessen, Eisenhauer, et al. (2009), while the original G2 object orbital elements were taken from Gillessen, Genzel, et al. (2013).

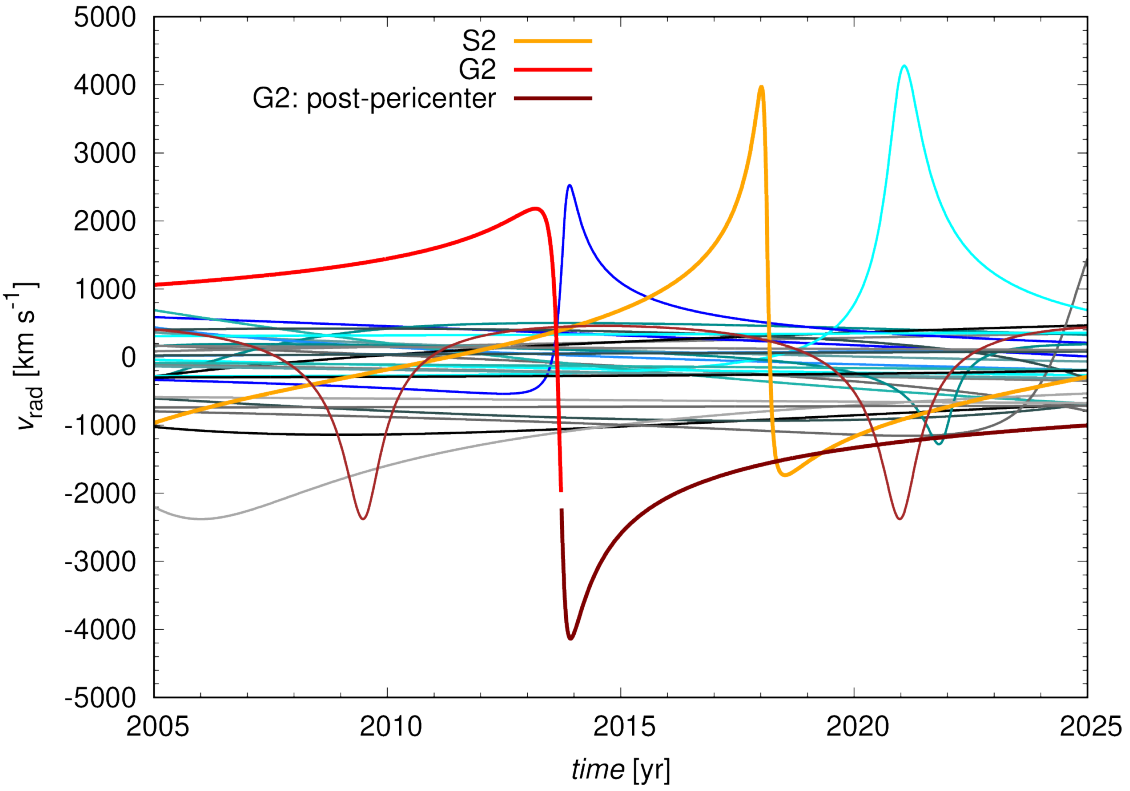

Figure 4.24: Radial velocities of S stars. The orange line stands for the S2 star while the red and maroon colours correspond to the pre-pericentre and the post-pericentre parts of the G2 orbit, respectively. The orbital elements for S stars were taken from Gillessen, Eisenhauer, et al. (2009), while the original G2 object orbital elements were taken from Gillessen, Genzel, et al. (2013).

For our extremal case, we can obtain the eccentricity from one of these realistic cases. Using the derived formula (2.80) and setting the periapsis distance

$$r_{\mathrm{p}} = a(1-e) = R\left(3\frac{M_{\mathrm{BH}}}{M}\right)^{1/3}. \tag{4.15}$$

From this equation, we can arrive at the orbital period

$$P = \left[\frac{9\pi M_{\mathrm{BH}}}{G\rho(M_{\mathrm{BH}}+M)}\right]^{1/2}(1-e)^{-3/2}. \tag{4.16}$$

Using the parameters of the S2 star, see Table 4.10, $M = 13.80\ \mathrm{M}_{\odot}$, $R = 6.02\ \mathrm{R}_{\odot}$ and eccentricity $e = 0.9389$ for S14 star (Bozza and Mancini (2005)), we obtain the period 29.82 days and the periapsis distance $r_{\mathrm{p}} = 4.24 \cdot 10^{11}$ m $= 33.67\ \mathrm{r_S}$. The effect of gravitational redshift was neglected, since it does not have a serious effect on the phase curve. For such an extremal case the effect is enormous. However, this is only a peak of the iceberg, and we need to study real cases. Such a trajectory studied here is very unstable, and objects orbiting so close would not last long. Therefore, it is almost impossible to detect an object on such an unstable orbit.

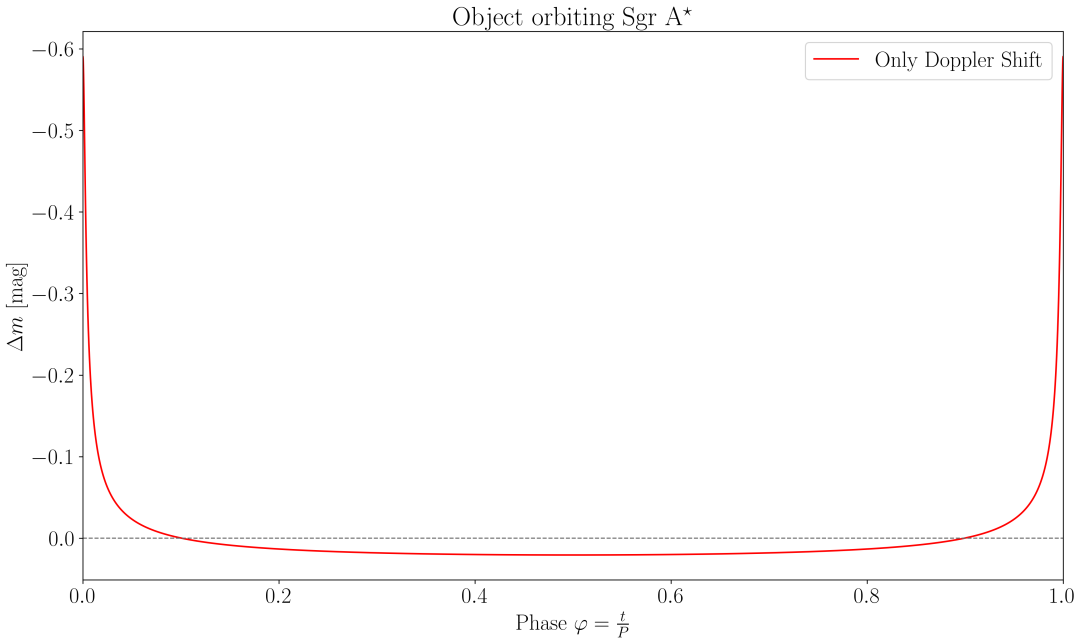

Figure 4.25: Phase curve in K filter $\lambda_0 = 2\,000$ nm and $\Delta\lambda = 400$ nm.

4.5.2 S2 star

The properties of the SMBH in the Galactic centre, which is associated with the compact radio source Sagittarius A*, were measured by monitoring so-called S stars. These are predominantly B-type stars orbiting close to Sgr A*. For our estimation, we have chosen the S2 star, since its orbital parameters are well known and are given in Tab. 4.10. Estimating

Parameter of S2 star	
Mass	13.80 $M_\odot$
Temperature	28 000 K
Orbital Parameters	
P	16.045 yr
e	0.885
i	134.567°
ϕ_0	66.263°
Ω	228.171°

Table 4.10: The parameters of the S2 star were obtained from Habibi et al. (2017) and the orbital parameters from GRAVITY Collaboration et al. (2020).

the best photometric filter using the derived relation leads to $\lambda_{\text{best}} = 68$ nm. Unfortunately, the region around the central SMBH is full of dust, so the extinction plays a major role here. Therefore, it is necessary to use a photometric filter at longer wavelengths (IR, microwaves), in our case the K-band filter $\lambda_0 = 2\,000$ nm and with the width $\Delta\lambda = 400$ nm. Modelling this effect for these wavelengths can help us compare if the effect still be observable.

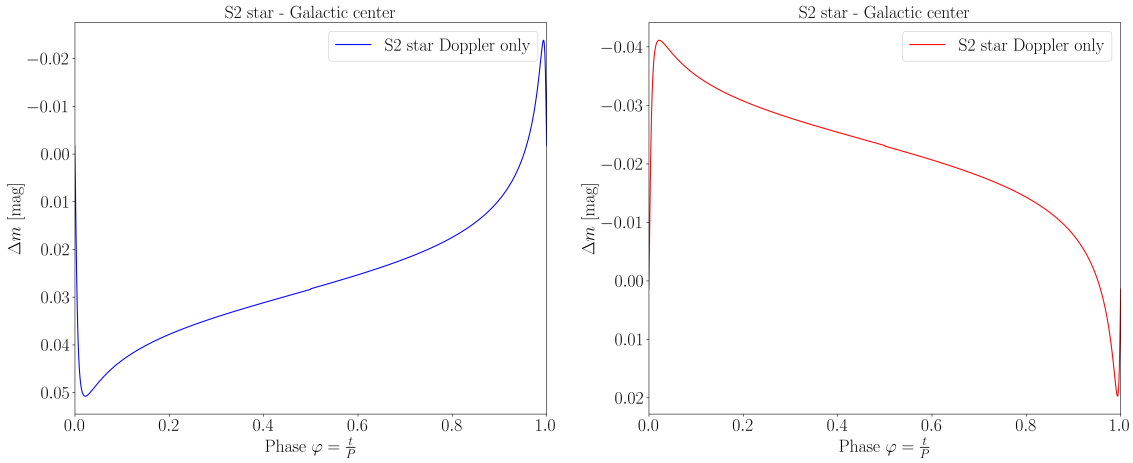

(a) Phase curve - S2 star in the ideal filter $\lambda_0 =$ 66 nm and $\Delta\lambda = 5$ nm.

(b) Phase curve - S2 star in K filter $\lambda_0 = 2\,000$ nm and $\Delta\lambda = 400$ nm.

Figure 4.26: Phase curves for the S2 star in the corresponding photometric filters.

We can conclude that the effect is still observable even in the K-band filter. One could admit that we did not include the gravitational redshift caused by the SMBH. Although the gravitational field of Sgr A* is strong, the S2 star orbits at a large distance. Therefore, the effect of gravitational redshift can be neglected. This comment is also based on the calculations where the difference was unnoticeable.

4.5.3 G objects

As mentioned earlier, the SMBH in the Galactic centre hosts various types of stars and other objects. In the previous subsection, we mentioned young hot subdwarf stars called S stars, which are relatively young ($\sim 5-10$ millions years), which can orbit very close to the SMBH and by monitoring their motion we can determine properties of their trajectories and Sgr A*.

In this region, not only were relatively regular objects, main-sequence stars, such as S stars, identified but also a class of dust-enshrouded objects, so-called G objects, were detected. They are characterized by broad emission, such as the hydrogen Brγ recombination line. They also orbit close to the Sgr A* and could help us understand the processes in galactic nuclei even further. In recent years, these objects have been monitored and studied. The first proposition was that they are just coreless gasseous-dusty clouds. However, one of the G objects passed the pericentre of Sgr A* on the length scale of a few 1 000 Schwarzschild radii. Although such a passage should be deadly for the dust cloud, it stayed relatively unchanged and intact. This fact showed that the cloud must be compact enough to survive the close passage. Nowadays theories converge towards the scenario that the G objects are dust-enshrouded stars that shine mostly in the IR domain and are characterized with the temperature 500-600 K and the gaseous-dusty envelope is limited by the Hill radius (Zajaček, Pikhartová, and Peissker (2024)) that reaches several astronomical units. Let us now study our effect on G objects, where we will focus on the G2 object, which passed through the pericentre of Sgr A* in 2014. The trajectory and G2 object parameters can be found in Tab. 4.11. The only problem lies in estimating the mass of the G2 object, since for the dusty envelope we obtain 3 M_{Earth}. However, if there is a star in it, it can reach a few $M_\odot$. Luckily, it is not a big deal for our calculations since the SMBH is much heavier.

Parameters of the G2 object	
Mass	$3\ M_{\text{Earth}} + M_{\text{star}}$
Temperature	~ 600 K
Orbital Parameters	
P	391 yr
e	0.970
i	118°
ϕ_0	97°
Ω	82°

Table 4.11: Both the trajectory and the G2 object parameters were obtained from Meyer et al. (2014). The temperature was obtained from Zajaček, Pikhartová, and Peissker (2024).

From Fig. 4.27, where we also used the gravitational redshift, even if it was not necessary, we can see that the rate of change is surprisingly large. In our calculations, the total mass of the G2 object was set to 3 M_{Earth}.

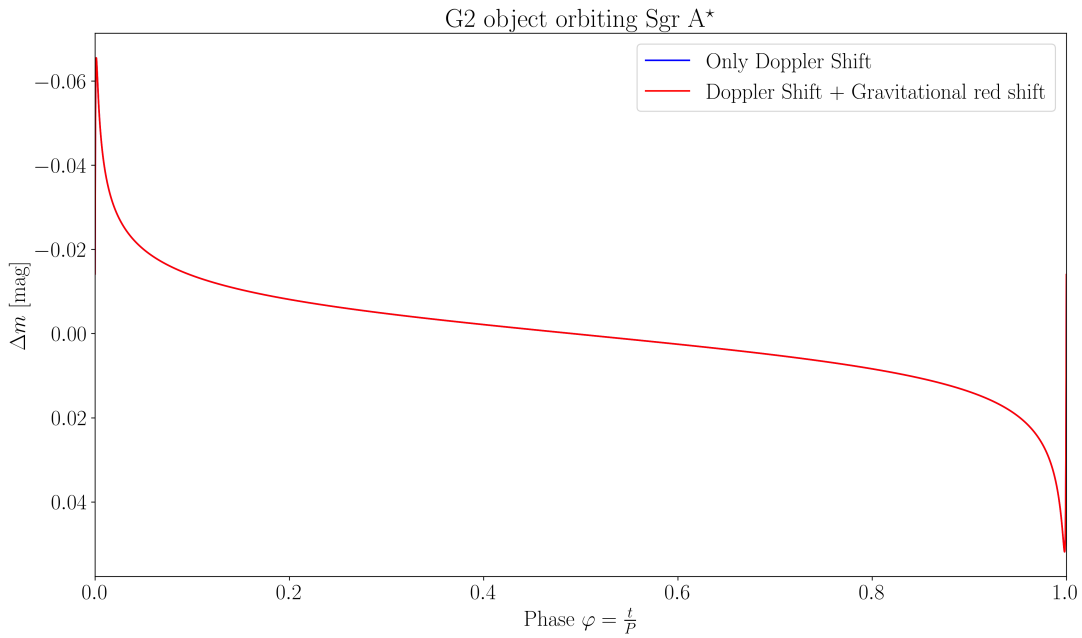

Figure 4.27: Phase curve - G2 object in the K-band filter with $\lambda_0 = 2\ 000$ nm and $\Delta\lambda = 400$ nm.

4.6 Cosmological problems

4.6.1 Expansion and K correction

In Fig. 3.1d, we can see that the peak for the positive radial velocities is going to the longer wavelength. Moreover, the intensity in infrared, microwave, and radio is increasing, which is in good agreement with observations.

The big mystery of astronomy is still the Hubble–Lemaître constant. As we mentioned earlier (Sect. 2.4), there are several ways to measure the distance and, thanks to it, calculate the Hubble–Lemaître constant, either from Cepheids or using standard candles SN Ia. The interesting fact is that for the nearest galaxies we can use our relations without any corrections. However, as we saw earlier, if we we use a narrow photometric filter, the intensity of light can be different due to the radial velocity effect. This means that the apparent visual magnitude measured can be a little different. As the apparent visual magnitude is in exponent, a small effect could make bigger difference. Although for closest galaxies the effect is not that high, for distant galaxies it could be serious. Let us see how big this problem is four our closest galactic neighbourhood. Since the Hubble Space Telescope (HST) observed Cepheid variables in the Virgo galaxy cluster, we can compare on this scale. Using the law of uncertainty propagation, we can determine the relative error of distance:

$$\frac{\Delta r}{r} = 0.2 \cdot \ln 10 \cdot \Delta m \approx 0.4605 \cdot \Delta m. \tag{4.17}$$

From equation (4.17) we derive that for higher radial velocities Δm will be higher and therefore the error of measuring the distance will be higher as well. Of course, there will

be different effects for different photometric filters and for various effective temperatures of the stars as shown in Fig. 4.28. As we mentioned earlier, the relative error of the

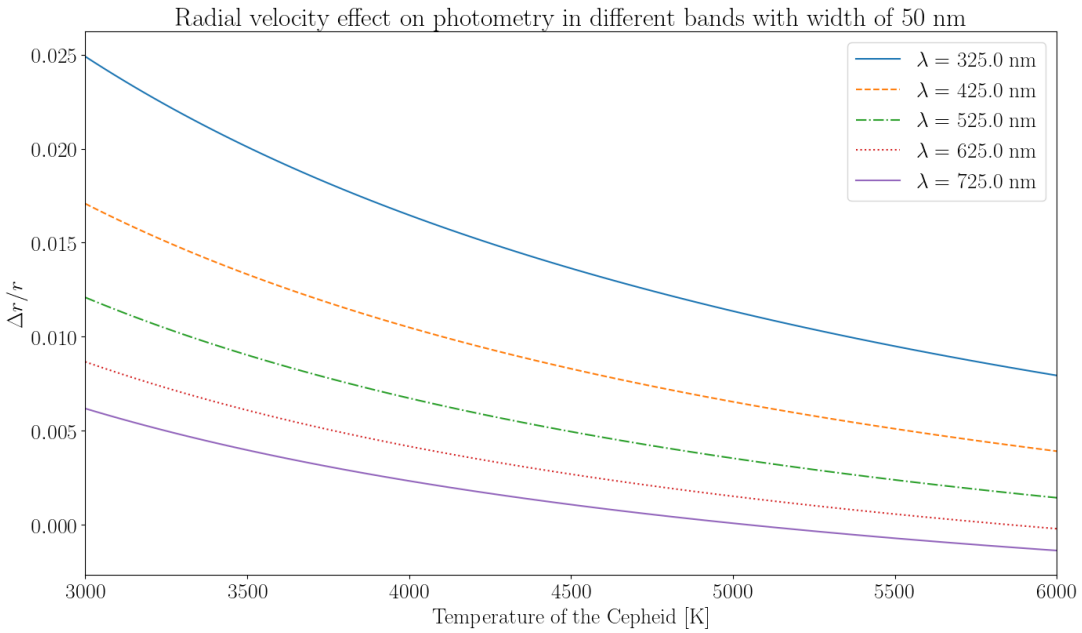

Figure 4.28: Relation between the relative distance error and the temperature of the Cepheid variables in the Virgo cluster.

distance is small. However, for the five-times further object (326 Mpc) the effect is fatal.

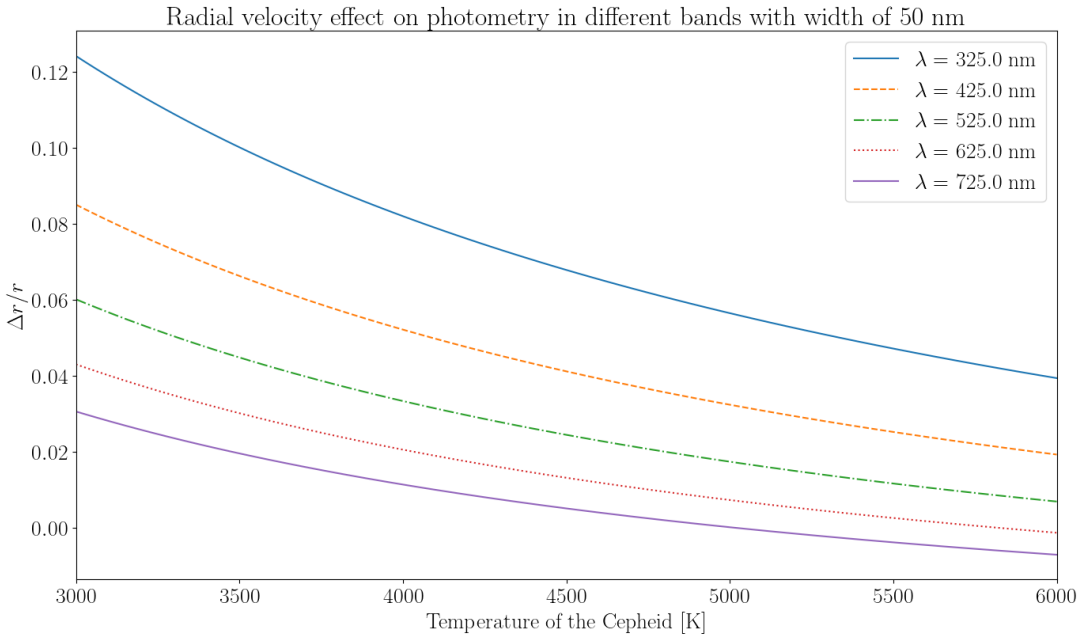

Figure 4.29: Relation between the relative distance error and the temperature of the Cepheid variables at the distance 326 Mpc.

This problem is not only connected to variable stars such as Cepheids, but it also includes SN Ia and other standard candles, with whose help we measure the distance.

These are essential reasons to introduce the so-called K correction. It is the coefficient that corrects the distance modulus. Using luminosity distance D_{L} in parsecs, we obtain a corrected relation

$$M = m - 5\log D_{\mathrm{L}} + 5 - K_{\mathrm{Corr}}. \tag{4.18}$$

The letter K is used because of the shift to red wavelengths, for which is used the K-band filter is used, and the correction was introduced by Hubble (1936).

4.6.2 Peculiar velocities and rotational profiles

Not only does the expansion of the Universe cause trouble. As we observe a distant galaxy, the stars rotate around the galactic centre at velocities close to hundreds of kilometres per second. In light of the previous cases, it is not necessary to explain what it could cause.

We should not just talk about the rotational velocities. The motion of stars in the galaxy can be very chaotic. For example, let us take a binary star in the last stage of its life. Let us suppose that in such a binary one of the companion explodes as a supernova. This instability could lead to splitting of the system. Hence, the supernova could reach the kick off velocity and as such move differently through the galaxy. This is not just about binaries, but the same problem could occur in stellar or galactic clusters. As the whole cluster moves at some radial velocity, some members could move within the cluster in different directions. That is often called the peculiar velocity. The velocities are usually dependent on the masses of the objects, but can reach hundreds to thousands of kilometres per second.

Discussion and Future Prospects

In this work, we study the effect of radial velocity on the observed flux of an object in a narrowband filter. In particular, we combine the spectral intensity distribution, primarily using the Planck's law, with the Doppler effect. In addition to the Doppler effect, we also consider the impact of relativistic motion and gravitational redshift. The higher the radial velocity, the stronger the effect; in extreme cases, it can reach up to 0.1 mag. The temperature then determines where the effect is most significant.

In general, we can say that the effect exists and affects stellar spectra (continuum emission) but not only. However, it is not so significant in most cases such as classical binaries. This is mostly given by the fact that the hotter stars are in general heavier. Their radiation is stronger, unfortunately their radial velocities are not so high. Moreover, as we study binaries, where stars are more similar, the presence of the second companion often decreases the total effect. The same result is obtained for binaries with a compact companion. But if the compact companion accretes matter and shines mostly in the X-ray part of the spectra, then the effect could be observable.

Speaking about galactic nuclei, where we can observe the emission of stars orbiting the SMBH as well as the other objects, in this environment we can expect the effect to be large due to high radial velocities. Therefore, galactic nuclei may be a good test-bed for studying this effect.

On cosmological scales, we have to be careful about the radial velocity of the object, since it can distort our view towards the observed object. In this case, it is necessary to obtain the spectra to minimize the possible error.

Concerning the discovery of non-accreting black holes, we can definitely say that it is possible but only with precise measurements and under special conditions when orbiting stars can get close enough. The variability timescale would be given by the orbital period of the companion.

In the future, next-generation observational facilities such as the Extremely Large Telescope (ELT) (Padovani and Cirasuolo (2023)), ULTRASAT (Shvartzvald et al. (2024)), QUVIK (Werner et al. (2024)) and Ultraviolet Explorer (UVEX) (Kulkarni et al. (2021)) will provide high-quality, precise data in the UV, optical, and infrared domains. The effects discussed in this work may therefore become relevant for high-precision measurements and should be taken into account in data analysis. Conversely, these instruments may also enable the direct detection of this effect, potentially allowing them to be used to refine and improve observational results.

Conclusion

Our objective was to study the effect of radial velocity on the observed flux of an object in a narrowband filter. The combination of the spectral distribution with effects such as the Doppler effect, relativistic Doppler effect and gravitational redshift shows that the object can appear either dimmer or brighter. We aimed to describe this effect mathematically and provide its physical interpretation.

Using the derived relation (3.24) we were able to determine the central wavelength λ_0 of the narrowband filter, with the filter width in most cases set to $\Delta\lambda = 5$ nm. From the orbital parameters, we determined the radial velocity as a function of phase and calculated the intensity numerically, comparing it with the intensity of the same object at rest. This allowed us to determine the corresponding change in magnitude. A similar approach was applied to binary stars.

For classical binaries, the effect is negligible in most cases. However, since it is phase-correlated with the radial velocity curve it can be subtracted from data to improve measurement precision. In cases where the spectroscopic data are insufficient to determine radial velocity profiles, and one component dominates the flux, it may be possible to infer the radial velocity curve from residuals in the phase curve. In X-ray binaries, variability from the compact components is detectable in the X-ray part of the spectrum, where it dominates the emission. In general, the effect is stronger at higher energies (e.g., X-ray or UV), which could be exploited by future missions, such as ULTRASAT and QUVIK.

For non-accreting black holes, we find that the detection may be possible through periodic photometry variations of companion stars that follow the radial velocity curve. These variations typically reach amplitudes of the order of 0.01 mag, although values at the millimagnitude level are more realistic.

In the Galactic centre, where high radial velocities are common, the effect becomes significant for various object (e.g, S-stars or G-objects). In extreme cases, the amplitude of variability can reach up to 0.5 mag, while for realistic cases such as the S2 star or the G2 object, we obtain variations of approximately 0.1 mag.

On cosmological scales, high velocities are also present; however, these effects are typically accounted for in standard corrections. Nevertheless, precise spectroscopic measurements remain essential for the accurate determination of radial velocities and to avoid systematic errors.

Overall, we have shown that the effect is generally negligible. However, in specific environments it can become significant or even useful for improving measurement precision. The variability timescale is given by the orbital period, while the amplitude is primarily determined by the radial velocity. For classical binaries, the resulting variations are comparable to those observed in transiting exoplanet systems or low-amplitude pulsators, such as δ Scuti or β Cephei stars. In the Galactic centre, the variability can reach levels comparable to stellar pulsations, rotational modulation due to starspots, or eclipsing binaries.

Appendix A

Geometric series

In this appendix, we briefly introduce geometric series, which will be used in Chapter C in the derivation of the integral appearing in the Stefan–Boltzmann law.

Let us imagine that the doctor injects us with some substance to prepare us for a medical procedure. Of course, this substance will not stay in our body for a long time. Let us say that every minute the half of the substance in the body is gone. This half can be named as a quotient q. Then the relation for the amount of substance at a certain time a_n as a function of the previous amount a_{n-1} is

$$\boxed{a_n = a_{n-1}q.} \tag{A.1}$$

Of course, we can continue

$$a_n = a_{n-1}q = a_{n-2}q^2,$$

until we get the relation for n-th component

$$\boxed{a_n = a_0 q^{n-1}.} \tag{A.2}$$

Let us analyze this sequence and try to draw a few points and begin with $q > 1$.

Geometric sequence

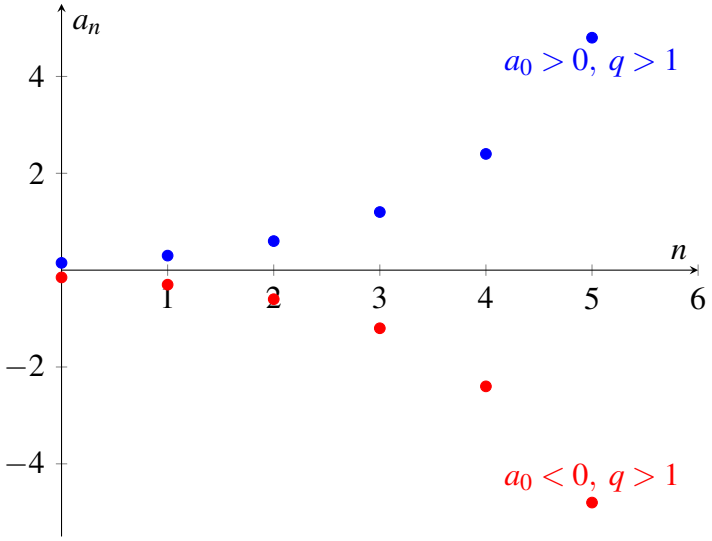

It is obvious that for $a_0 < 0$ the sequence is decreasing. However, for $a_0 > 0$ it is increasing and for $a_0 = 0$ it is a constant sequence. Now, we will look at what will happen, if the quotient is $q < -1$.

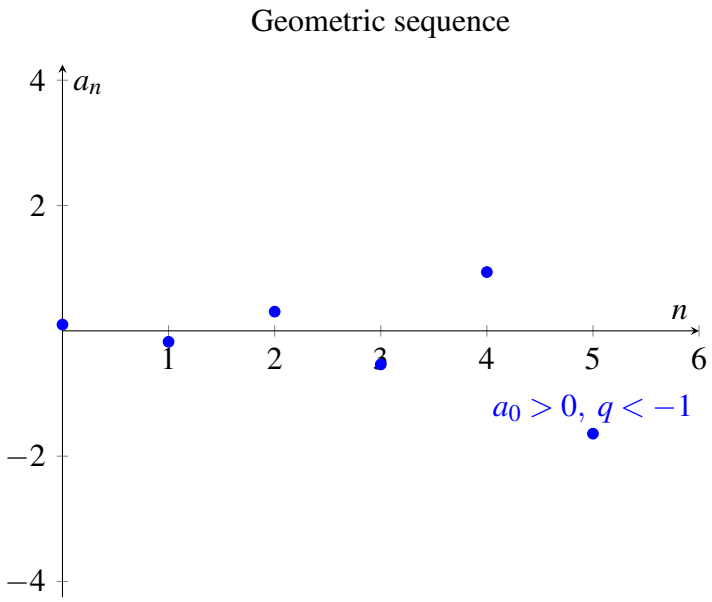

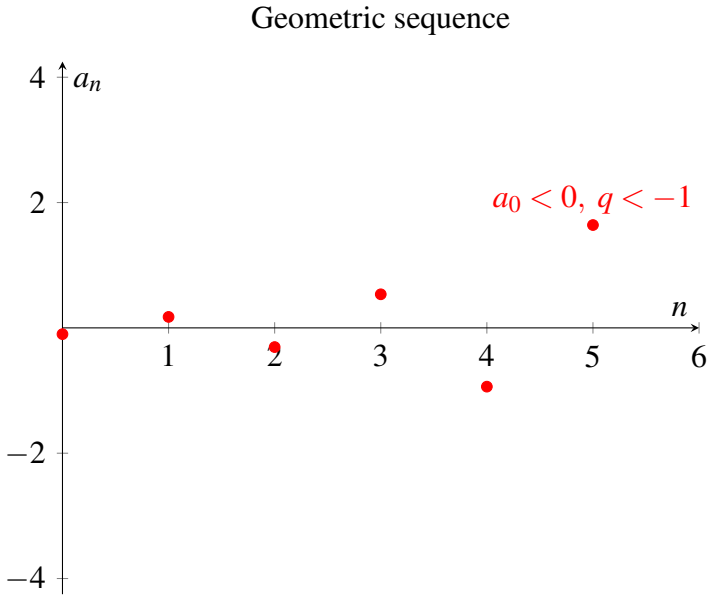

For both $a_0 < 0$ or $a_0 > 0$ we get the same result, it is only mirrored. The sequences are oscillating with higher and higher amplitudes.

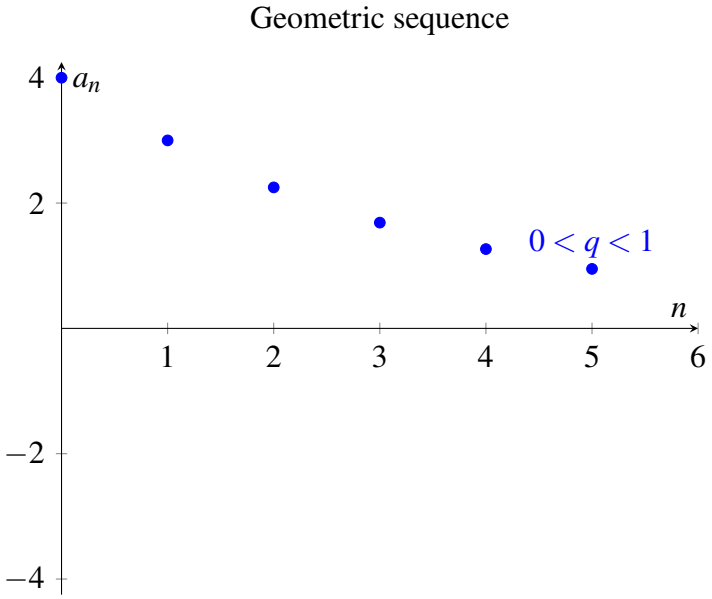

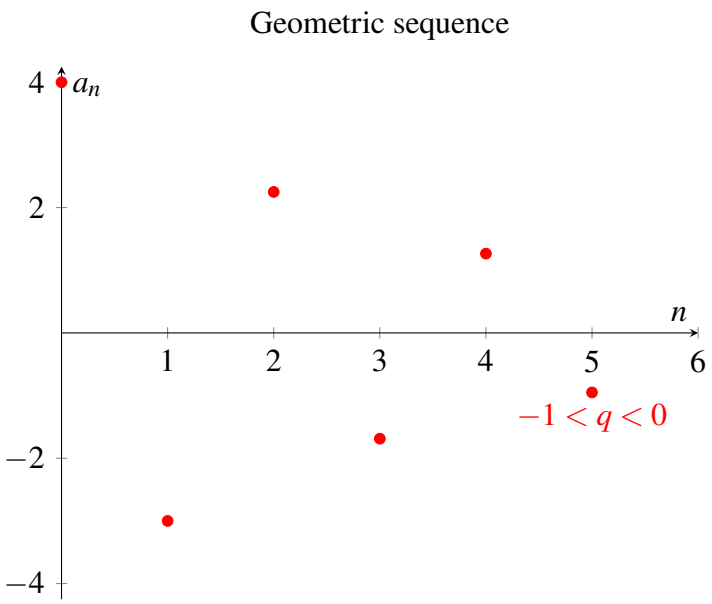

In case $0 < q < 1$, $a_0 > 0$, the sequence is decreasing, which could be the case with our medical substance. For $-1 < q < 0$ the sequence oscillates, however, for this case amplitudes go to zero. This can be the case, when a telescope tries to find an object and goes slowly to it. Now, when we introduce ourselves with this sequence, we can add all the components

$$s_n = a_0 + a_1 + \cdots + a_{n-1} + a_n. \tag{A.3}$$

Using the relation for the n-th component,

$$s_n = a_0 + a_0 q + \cdots + a_0 q^{n-1} + a_0 q^n, \tag{A.4}$$

$$qs_n = a_0 q + a_0 q^2 + \cdots + a_0 q^n + a_0 q^{n+1}, \tag{A.5}$$

$$\tag{A.6}$$

subtracting equations and making some corrections leads to

$$\boxed{s_n = a_0 \frac{1-q^{n+1}}{1-q}.} \tag{A.7}$$

For $|q| < 1$ the series converges, for $q \geq 1$ the series diverges, and for $q \leq -1$ the series oscillates. Using a limit as n goes to infinity, we obtain the following

$$\boxed{\sum_{n=0}^{\infty} a_0 q^n = \frac{a_0}{1-q}.} \tag{A.8}$$

Appendix B

Fourier series

In this appendix, we review Fourier series, which will also be used in Chapter C for the derivation of the integral appearing in the Stefan–Boltzmann law.

The Fourier series of the function $f(x)$ can be defined as follows,

$$\boxed{f(x) = \frac{a_0}{2} + \sum_{n=1}^{\infty} \left[a_n \cos(n\omega x) + b_n \sin(n\omega x) \right],} \tag{B.1}$$

where a_0, a_n a b_n are Fourier coefficients which can be calculated using the period T. The relation for ω is

$$\omega = \frac{2\pi}{T}. \tag{B.2}$$

Fourier coefficients can be calculated using relations

$$a_0 = \frac{2}{T} \int_{T_0}^{T_0+T} f(x)\ \mathrm{d}x, \tag{B.3}$$

$$a_n = \frac{2}{T} \int_{T_0}^{T_0+T} f(x) \cos(n\omega x)\ \mathrm{d}x, \tag{B.4}$$

$$b_n = \frac{2}{T} \int_{T_0}^{T_0+T} f(x) \sin(n\omega x)\ \mathrm{d}x. \tag{B.5}$$

Let us suppose that we have a periodic function with periodicity. For this situation, we can use the Fourier series. Moreover, the Fourier series is motivated by solving the heat equation

$$\frac{\partial u(t,x)}{\partial t} = \alpha \frac{\partial^2 u(t,x)}{\partial x^2}, \tag{B.6}$$

where α is a diffusion coefficient. Let us say that we want to find a solution with the separation of variables

$$u(t,x) = X(x)T(t). \tag{B.7}$$

After a few operations, we arrive at the point where the Fourier series appear. Of course, this is only one face of the beast. All the terms in the Fourier series can be used as an orthogonal system in the Hilbert space. This can be very useful in quantum mechanics when we try to find the wave function.

Appendix C

Derivation of the integral in Stefan–Boltzmann law

In this paragraph, we will finally look at the derivation[1] of the integral

$$\mathscr{I} = \int_0^\infty \frac{x^3}{\mathrm{e}^x - 1}\,\mathrm{d}x. \tag{C.1}$$

Multiplying the numerator and the denominator by the term e^{-x}, we obtain

$$\mathscr{I} = \int_0^\infty x^3 \frac{\mathrm{e}^{-x}}{1-\mathrm{e}^{-x}}\,\mathrm{d}x. \tag{C.2}$$

We can notice that the fraction $\frac{\mathrm{e}^{-x}}{1-\mathrm{e}^{-x}}$ looks similar to the relation in Eq. (A.8). We can write

$$\frac{\mathrm{e}^{-x}}{1-\mathrm{e}^{-x}} = \sum_{n=0}^{\infty} \mathrm{e}^{-(n+1)x} = \sum_{n=1}^{\infty} \mathrm{e}^{-nx}. \tag{C.3}$$

Although the first sum can be used, the second sum is better for further calculation. We obtain an integral

$$\mathscr{I} = \int_0^\infty x^3 \sum_{n=1}^{\infty} \mathrm{e}^{-nx}\,\mathrm{d}x. \tag{C.4}$$

Now the idea of switching between summation and integration could come to our mind. Firstly, we should rethink if it is possible and if we can do that. The sum of the sequence of functions $f_n(x) = \mathrm{e}^{-nx}$ converges uniformly in the interval $x \in [\delta, \infty)$, where for δ we have the condition $\delta \in (0, \infty)$. Since $x = 0$ is not in the interval, we cannot simply interchange the operations. Luckily, $x = 0$ is a group of zero size, so we can use a limit to avoid a mistake. The steps will be the following

$$\int_0^\infty x^3 \sum_{n=1}^{\infty} \mathrm{e}^{-nx}\,\mathrm{d}x = \sum_{n=1}^{\infty} \left(\lim_{\delta\to 0} \int_\delta^\infty x^3 \mathrm{e}^{-nx}\,\mathrm{d}x \right). \tag{C.5}$$

Using the per-partes method, we get

$$\mathscr{I} = \sum_{n=1}^{\infty} \left(\lim_{\delta\to 0} \left[-\frac{x^3}{n}\mathrm{e}^{-nx} - \frac{3x^2}{n^2}\mathrm{e}^{-nx} - \frac{6x}{n^3}\mathrm{e}^{-nx} - \frac{6}{n^4}\mathrm{e}^{-nx} \right]_\delta^\infty \right) = \sum_{n=1}^{\infty} \frac{6}{n^4}. \tag{C.6}$$

[1] The solution was inspired by the book Kulhánek (2020), chapter 3.10.4.

Now, the only thing left is to determine the sum of infinite series[2] $\sum_{n=1}^{\infty}\frac{1}{n^4}$. At this point, it would be very useful to use Fourier series. In denominator, we have the fourth power of n, which could lead to an idea of using the Fourier series of x^4 in the interval $x \in [-\pi,\pi] \Rightarrow T = 2\pi$ and $\omega = 1$. The function is even, therefore, the Fourier series will contain only cosines. Moreover, the interval is cleverly set to remove the possible remaining cosines.

$$a_0 = \frac{1}{\pi}\int_{-\pi}^{\pi} x^4\,\mathrm{d}x = \frac{2}{\pi}\int_0^{\pi} x^4\,\mathrm{d}x = \frac{2\pi^4}{5}, \tag{C.7}$$

$$a_n = \frac{1}{\pi}\int_{-\pi}^{\pi} x^4\cos(nx)\,\mathrm{d}x = \frac{2}{\pi}\int_0^{\pi} x^4\cos(nx)\,\mathrm{d}x = \tag{C.8}$$

$$= \frac{2}{\pi}\left[\frac{x^4}{n}\sin(nx) + \frac{4x^3}{n^2}\cos(nx) - \frac{12x^2}{n^3}\sin(nx) - \frac{24x}{n^4}\cos(nx) + \frac{24}{n^5}\sin(nx)\right]_0^{\pi} = \tag{C.9}$$

$$= (-1)^n\left(\frac{8\pi^2}{n^2} - \frac{48}{n^4}\right), \tag{C.10}$$

$$b_n = \frac{1}{\pi}\int_{-\pi}^{\pi} x^4\sin(nx)\,\mathrm{d}x = 0. \tag{C.11}$$

It is obvious that the coefficients b_n really disappeared thanks to the even function x^4. Now we obtain the following

$$x^4 = \frac{\pi^4}{5} + \sum_{n=1}^{\infty}\left[(-1)^n\left(\frac{8\pi^2}{n^2} - \frac{48}{n^4}\right)\cos(nx)\right]. \tag{C.12}$$

From the result (C.12) we get the relation for our sum if we set $x = \pi$.

$$\sum_{n=1}^{\infty}\frac{1}{n^4} = -\frac{\pi^4}{60} + \frac{\pi^2}{6}\sum_{n=1}^{\infty}\frac{1}{n^2}. \tag{C.13}$$

The only thing remaining to calculate is $\sum_{n=1}^{\infty}\frac{1}{n^2}$, which is the famous Basel problem. There are several ways to calculate this sum, however, we will use once again the Fourier series with the function x^2 in the same interval. We get

$$a_0 = \frac{1}{\pi}\int_{-\pi}^{\pi} x^2\,\mathrm{d}x = \frac{2}{\pi}\int_0^{\pi} x^2\,\mathrm{d}x = \frac{2\pi^2}{3}, \tag{C.14}$$

$$a_n = \frac{1}{\pi}\int_{-\pi}^{\pi} x^2\cos(nx)\,\mathrm{d}x = \frac{2}{\pi}\int_0^{\pi} x^2\cos(nx)\,\mathrm{d}x = \tag{C.15}$$

$$= \frac{2}{\pi}\left[\frac{x^2}{n}\sin(nx) + \frac{2x}{n^2}\cos(nx) - \frac{2}{n^3}\sin(nx)\right]_0^{\pi} = \tag{C.16}$$

$$= (-1)^n\frac{4}{n^2}, \tag{C.17}$$

$$b_n = \frac{1}{\pi}\int_{-\pi}^{\pi} x^2\sin(nx)\,\mathrm{d}x = 0. \tag{C.18}$$

[2] This series can remind us the Riemann zeta function: $\zeta(s) = \sum_{n=1}^{\infty}\frac{1}{n^s}$, for $s = 4$.

The Fourier series will be the following

$$x^2 = \frac{\pi^2}{3} + 4\sum_{n=1}^{\infty}\left[\frac{(-1)^n}{n^2}\cos(nx)\right]. \tag{C.19}$$

Setting $x = \pi$, we obtain

$$\sum_{n=1}^{\infty}\frac{1}{n^2} = \frac{\pi^2}{6} = \zeta(2). \tag{C.20}$$

Plugging in Eq. (C.13) we finally get our sum

$$\sum_{n=1}^{\infty}\frac{1}{n^4} = \frac{\pi^4}{90}. \tag{C.21}$$

Applying this result to Eq. (C.6) we get

$$\boxed{\int_0^{\infty}\frac{x^3}{e^x - 1}\,dx = \frac{\pi^4}{15},} \tag{C.22}$$

which is the result we sought.

Appendix D

Derivation of the acceleration in the spherical coordinates

In this paragraph, we will attempt to derive the acceleration in the spherical coordinates. Let us start from the definition of acceleration

$$\mathbf{a} = \frac{\mathrm{d}^2\mathbf{r}}{\mathrm{d}t^2}, \tag{D.1}$$

where $\mathbf{r}$ stands for the position vector and with the help of the basis vectors $\hat{\mathbf{x}}, \hat{\mathbf{y}}$ and $\hat{\mathbf{z}}$ we express it in the Cartesian coordinates

$$\mathbf{r} = x \cdot \hat{\mathbf{x}} + y \cdot \hat{\mathbf{y}} + z \cdot \hat{\mathbf{z}}. \tag{D.2}$$

Introducing the spherical coordinates as follows

$$x = r\cos\phi\sin\theta \tag{D.3}$$
$$y = r\sin\phi\sin\theta \tag{D.4}$$
$$z = r\cos\theta \tag{D.5}$$

we can calculate unit basis vectors in the spherical coordinates

$$\hat{\mathbf{r}} = \frac{1}{|\hat{\mathbf{r}}|}\begin{pmatrix} \frac{\partial x}{\partial r} & \frac{\partial y}{\partial r} & \frac{\partial z}{\partial r} \end{pmatrix}\begin{pmatrix} \hat{\mathbf{x}} \\ \hat{\mathbf{y}} \\ \hat{\mathbf{z}} \end{pmatrix} \tag{D.6}$$

Similarly, it can be derived for the basis vectors $\hat{\theta}$ and $\hat{\phi}$. We find

$$\hat{\mathbf{r}} = \cos\phi\sin\theta \cdot \hat{\mathbf{x}} + \sin\phi\sin\theta \cdot \hat{\mathbf{y}} + \cos\theta \cdot \hat{\mathbf{z}} \tag{D.7}$$
$$\hat{\theta} = \cos\phi\cos\theta \cdot \hat{\mathbf{x}} + \sin\phi\cos\theta \cdot \hat{\mathbf{y}} - \sin\theta \cdot \hat{\mathbf{z}} \tag{D.8}$$
$$\hat{\phi} = -\sin\phi \cdot \hat{\mathbf{x}} + \cos\phi \cdot \hat{\mathbf{y}} \tag{D.9}$$

From the position vector $\mathbf{r}$ we need to derive relations for the Cartesian basis vectors in terms of the spherical coordinates. This can be done by finding the inverse matrix

transformation or solving the system of equations, which leads to

$$\hat{\mathbf{x}} = \cos\phi \sin\theta \cdot \hat{\mathbf{r}} + \cos\phi \cos\theta \cdot \hat{\theta} - \sin\phi \cdot \hat{\phi} \tag{D.10}$$

$$\hat{\mathbf{y}} = \sin\phi \sin\theta \cdot \hat{\mathbf{r}} + \sin\phi \cos\theta \cdot \hat{\theta} + \cos\phi \cdot \hat{\phi} \tag{D.11}$$

$$\hat{\mathbf{z}} = \cos\theta \cdot \hat{\mathbf{r}} - \sin\theta \cdot \hat{\theta} \tag{D.12}$$

It can be shown that for our position vector, we have

$$\mathbf{r} = r \cdot \hat{\mathbf{r}} \tag{D.13}$$

If we find the derivatives of the basis vectors, we can derive the relation for the acceleration in the spherical coordinates

$$\frac{\mathrm{d}\hat{\mathbf{r}}}{\mathrm{d}t} = \frac{\mathrm{d}\theta}{\mathrm{d}t} \cdot \hat{\theta} + \frac{\mathrm{d}\phi}{\mathrm{d}t} \sin\theta \cdot \hat{\phi} \tag{D.14}$$

$$\frac{\mathrm{d}\hat{\theta}}{\mathrm{d}t} = -\frac{\mathrm{d}\theta}{\mathrm{d}t} \cdot \hat{\mathbf{r}} + \frac{\mathrm{d}\phi}{\mathrm{d}t} \cos\theta \cdot \hat{\phi} \tag{D.15}$$

$$\frac{\mathrm{d}\hat{\phi}}{\mathrm{d}t} = -\frac{\mathrm{d}\phi}{\mathrm{d}t} \left(\sin\theta \cdot \hat{\mathbf{r}} + \cos\theta \cdot \hat{\theta}\right) \tag{D.16}$$

For the velocity, we get

$$\mathbf{v} = \frac{\mathrm{d}r}{\mathrm{d}t} \cdot \hat{\mathbf{r}} + r\frac{\mathrm{d}\theta}{\mathrm{d}t} \cdot \hat{\theta} + r\frac{\mathrm{d}\phi}{\mathrm{d}t} \sin\theta \cdot \hat{\phi} \tag{D.17}$$

and for the acceleration, we get

$$\begin{aligned}
\mathbf{a} = &\left[\frac{\mathrm{d}^2 r}{\mathrm{d}t^2} - r\left(\frac{\mathrm{d}\theta}{\mathrm{d}t}\right)^2 - r\sin^2\theta\left(\frac{\mathrm{d}\phi}{\mathrm{d}t}\right)^2\right]\hat{\mathbf{r}} \\
&+ \left[r\frac{\mathrm{d}^2\theta}{\mathrm{d}t^2} + 2\frac{\mathrm{d}r}{\mathrm{d}t}\frac{\mathrm{d}\theta}{\mathrm{d}t} - r\sin\theta\cos\theta\left(\frac{\mathrm{d}\phi}{\mathrm{d}t}\right)^2\right]\hat{\theta} \\
&+ \left[r\sin\theta\frac{\mathrm{d}^2\phi}{\mathrm{d}t^2} + 2\sin\theta\frac{\mathrm{d}r}{\mathrm{d}t}\frac{\mathrm{d}\phi}{\mathrm{d}t} + 2r\cos\theta\frac{\mathrm{d}\theta}{\mathrm{d}t}\frac{\mathrm{d}\phi}{\mathrm{d}t}\right]\hat{\phi}
\end{aligned} \tag{D.18}$$

which is the formula we sought.

Appendix E

Derivation of infinite sum

Let us derive the formula

$$\sum_{n=1}^{\infty} \frac{\mathrm{e}^{-n\alpha}}{n} = -\ln\left(1-\mathrm{e}^{-\alpha}\right). \tag{E.1}$$

To do so, we first consider the infinite series

$$\sum_{n=1}^{\infty} \frac{x^n}{n}. \tag{E.2}$$

We previously derived the geometric series

$$\sum_{n=0}^{\infty} x^n = \frac{1}{1-x}, \tag{E.3}$$

which converges uniformly on the interval $|x| < 1$, a condition that is satisfied here. Therefore, we may integrate both sides:

$$\int_0^x \frac{1}{1-t}\,\mathrm{d}t = -\ln(1-x), \tag{E.4}$$

where the absolute value in the logarithm is unnecessary because $|x| < 1$. Thanks to uniform convergence, we may interchange integration and summation on the left-hand side:

$$\int_0^x \sum_{n=0}^{\infty} t^n\,\mathrm{d}t = \sum_{n=0}^{\infty} \int_0^x t^n\,\mathrm{d}t = \sum_{n=0}^{\infty} \frac{x^{n+1}}{n+1} = \sum_{n=1}^{\infty} \frac{x^n}{n}. \tag{E.5}$$

Finally, substituting $x = \mathrm{e}^{-\alpha}$, we obtain

$$\boxed{\sum_{n=1}^{\infty} \frac{\mathrm{e}^{-n\alpha}}{n} = -\ln\left(1-\mathrm{e}^{-\alpha}\right).} \tag{E.6}$$

Bibliography

Blondin, John M. (Nov. 1994). "The Shadow Wind in High-Mass X-Ray Binaries". In: *ApJ* 435, p. 756. DOI: 10.1086/174853.

Borkovits, T. et al. (Oct. 2005). "Indirect evidence for short period magnetic cycles in W UMa stars. Period analysis of five overcontact systems." In: *A&A* 441.3, pp. 1087–1097. DOI: 10.1051/0004-6361:20052805. arXiv: astro-ph/0507228 [astro-ph].

Bozza, V. and L. Mancini (July 2005). "Gravitational Lensing of Stars in the Central Arcsecond of Our Galaxy". In: *ApJ* 627.2, pp. 790–802. DOI: 10.1086/430664. arXiv: astro-ph/0503664 [astro-ph].

Čechura, J. and P. Hadrava (Mar. 2015). "Stellar wind in state transitions of high-mass X-ray binaries". In: *A&A* 575, A5, A5. DOI: 10.1051/0004-6361/201424636. arXiv: 1412.3924 [astro-ph.SR].

Cherepashchuk, A. M., T. S. Khruzina, and A. I. Bogomazov (Nov. 2021). "Parameters of the X-ray binary system Scorpius X-1". In: *MNRAS* 508.1, pp. 1389–1403. DOI: 10.1093/mnras/stab2515. arXiv: 2109.00967 [astro-ph.SR].

Eggleton, P. P. (May 1983). "Aproximations to the radii of Roche lobes." In: *ApJ* 268, pp. 368–369. DOI: 10.1086/160960.

Frank, Juhan, Andrew King, and Derek Raine (2002). *Accretion Power in Astrophysics*. 3rd ed. Cambridge: Cambridge University Press.

Geier, S. et al. (Mar. 2015). "The fastest unbound star in our Galaxy ejected by a thermonuclear supernova". In: *Science* 347.6226, pp. 1126–1128. DOI: 10.1126/science.1259063. arXiv: 1503.01650 [astro-ph.SR].

Giacconi, R. et al. (July 1971). "Discovery of Periodic X-Ray Pulsations in Centaurus X-3 from UHURU". In: *ApJL* 167, p. L67. DOI: 10.1086/180762.

Gillessen, S., F. Eisenhauer, et al. (Feb. 2009). "Monitoring Stellar Orbits Around the Massive Black Hole in the Galactic Center". In: *ApJ* 692.2, pp. 1075–1109. DOI: 10.1088/0004-637X/692/2/1075. arXiv: 0810.4674 [astro-ph].

Gillessen, S., R. Genzel, et al. (Feb. 2013). "New Observations of the Gas Cloud G2 in the Galactic Center". In: *ApJ* 763.2, 78, p. 78. DOI: 10.1088/0004-637X/763/2/78. arXiv: 1209.2272 [astro-ph.GA].

GRAVITY Collaboration et al. (Apr. 2020). "Detection of the Schwarzschild precession in the orbit of the star S2 near the Galactic centre massive black hole". In: *A&A* 636, L5, p. L5. DOI: 10.1051/0004-6361/202037813. arXiv: 2004.07187 [astro-ph.GA].

Habibi, M. et al. (Oct. 2017). "Twelve Years of Spectroscopic Monitoring in the Galactic Center: The Closest Look at S-stars near the Black Hole". In: *ApJ* 847.2, 120, p. 120. DOI: 10.3847/1538-4357/aa876f. arXiv: 1708.06353 [astro-ph.SR].

Hubble, Edwin (Dec. 1936). "Effects of Red Shifts on the Distribution of Nebulae". In: *ApJ* 84, p. 517. DOI: 10.1086/143782.

Kiss, L. L., Gy. M. Szabó, and T. R. Bedding (Nov. 2006). "Variability in red supergiant stars: pulsations, long secondary periods and convection noise". In: *MNRAS* 372.4, pp. 1721–1734. DOI: 10.1111/j.1365-2966.2006.10973.x. arXiv: astro-ph/0608438 [astro-ph].

Kulhánek, Petr (2020). *Vybrané kapitoly z teoretické fyziky. I*. Praha: AGA.

Kulkarni, S. R. et al. (Nov. 2021). "Science with the Ultraviolet Explorer (UVEX)". In: *arXiv e-prints*, arXiv:2111.15608, arXiv:2111.15608. DOI: 10.48550/arXiv.2111.15608. arXiv: 2111.15608 [astro-ph.GA].

Lorenzo, J. et al. (Dec. 2014). "MY Camelopardalis, a very massive merger progenitor". In: *A&A* 572, A110, A110. DOI: 10.1051/0004-6361/201424345. arXiv: 1410.5575 [astro-ph.SR].

Mereminskiy, I. A. et al. (Feb. 2018). "A Deep Extragalactic Survey with the ART-XC Telescope of the Spectrum-RG Observatory: Simulations and Expected Results". In: *Astronomy Letters* 44.2, pp. 67–80. DOI: 10.1134/S1063773718020044.

Meyer, L. et al. (May 2014). "The Keplerian orbit of G2". In: *The Galactic Center: Feeding and Feedback in a Normal Galactic Nucleus*. Ed. by L. O. Sjouwerman, C. C. Lang, and J. Ott. Vol. 303. IAU Symposium, pp. 264–268. DOI: 10.1017/S1743921314000714. arXiv: 1312.1715 [astro-ph.GA].

Mikulášek, Zdeněk (2021). *Fyzika horkých hvězd*. university lecture notes. URL: https://astro.physics.muni.cz/download/documents/skripta/F7601_1.pdf.

Mikulášek, Zdeněk and Jiří Krtička (2013). *Úvod do fyziky hvězd*. Brno: Masarykova univerzita.

Nashed, G. G. L. (June 2023). "The Effect of f(R, T) Modified Gravity on the Mass and Radius of Pulsar HerX1". In: *The Astrophysical Journal* 950.2, p. 129. ISSN: 1538-4357. DOI: 10.3847/1538-4357/acd182. URL: http://dx.doi.org/10.3847/1538-4357/acd182.

Padovani, Paolo and Michele Cirasuolo (Jan. 2023). "The Extremely Large Telescope". In: *Contemporary Physics* 64.1, pp. 47–64. DOI: 10.1080/00107514.2023.2266921. arXiv: 2312.04299 [astro-ph.IM].

Papavasileiou, Th. V., O. Kosmas, and T. S. Kosmas (Jan. 2025). "A simplified approach for reproducing fully relativistic spectra in X-ray binary systems: Application to Cygnus X-1". In: *A&A* 693, A75, A75. DOI: 10.1051/0004-6361/202451798. arXiv: 2408.02415 [astro-ph.HE].

Schröder, K.-P. and M. Cuntz (Apr. 2007). "A critical test of empirical mass loss formulas applied to individual giants and supergiants". In: *A&A* 465.2, pp. 593–601. DOI: 10.1051/0004-6361:20066633. arXiv: astro-ph/0702172 [astro-ph].

Shvartzvald, Y. et al. (Mar. 2024). "ULTRASAT: A Wide-field Time-domain UV Space Telescope". In: *ApJ* 964.1, 74, p. 74. DOI: 10.3847/1538-4357/ad2704. arXiv: 2304.14482 [astro-ph.IM].

von Zeipel, H. (June 1924). "The radiative equilibrium of a rotating system of gaseous masses". In: *MNRAS* 84, pp. 665–683. DOI: 10.1093/mnras/84.9.665.

Waisberg, I. et al. (July 2017). "Submilliarcsecond Optical Interferometry of the High-mass X-Ray Binary BP Cru with VLTI/GRAVITY". In: *ApJ* 844.1, 72, p. 72. DOI: 10.3847/1538-4357/aa79f1. arXiv: 1705.02351 [astro-ph.SR].

Werner, N. et al. (Feb. 2024). "Science with a Small Two-Band UV-Photometry Mission I: Mission Description and Follow-up Observations of Stellar Transients". In: *Space Sci. Rev.* 220.1, 11, p. 11. DOI: 10.1007/s11214-024-01048-3. arXiv: 2306.15080 [astro-ph.HE].

Young, A. J. et al. (Aug. 2001). "A complete relativistic ionized accretion disc in Cygnus X-1". In: *MNRAS* 325.3, pp. 1045–1052. DOI: 10.1046/j.1365-8711.2001.04498.x. arXiv: astro-ph/0103214 [astro-ph].

Zajaček, Michal, Monika Pikhartová, and Florian Peissker (Sept. 2024). "Galactic center G objects as dust-enshrouded stars near the supermassive black hole". In: *arXiv e-prints*, arXiv:2410.00304, arXiv:2410.00304. DOI: 10.48550/arXiv.2410.00304. arXiv: 2410.00304 [astro-ph.GA].